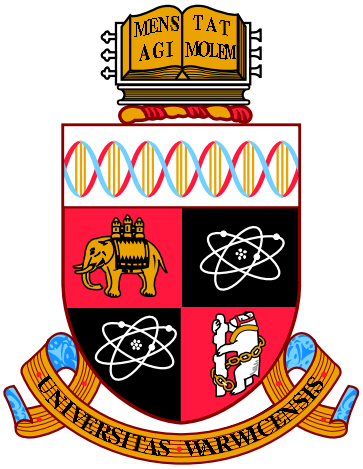

Bacterial inner membrane remodelling by force generation of FtsZ fibres

by

Erick Martins Ratamero

Thesis

Submitted to the University of Warwick

for the degree of

Doctor of Philosophy

Department of Physics

July 2017

THE UNIVERSITY OF WARWICK

Contents

List of Figures

Acknowledgments

If 31-year old Erick told 15-year old Erick he would be about to finish a PhD thesis at an excellent British university working on a project between theoretical physics and molecular biology, teenage Erick would have found that very funny and completely impossible.

The journey to this point has been very, very long and not particularly easy. There are many junctures in my life where a single thing being slightly different would probably have resulted in a wildly different outcome. It sounds strange to acknowledge the particular set of coincidences and events outside my control that contributed to this work ever existing, but they were a huge part of my success (as they are a huge part of anyone's success). So there you go.

My supervisors, Matthew Turner and Corinne Smith, were the best supervisors I could ever have hoped for. As someone with no background in statistical mechanics or cell biology, they have taught me as much as they could in these almost four years and were always available and encouraging at every step of the way. I am immensely grateful to them. I would also like to extend my thanks to Prof. Harold Erickson at Duke University, who, without ever having met me and knowing I had very little lab experience, agreed to host me in his lab for six months and was the most graceful host possible. Also, many thanks to Alison Rodger, who acted as quasi-supervisor, organizer, impromptu advisory committee, and who made my PhD fellowship possible. Finally, many thanks to Naomi Grew, whom I knew I could always count on if I needed to

sort any non-scientific issues.

I am saving a whole paragraph for office PS001 because that place shaped who I am. We shared many laughs, many pints, many ideas. I am not going to cite names because there are too many and I am very afraid of forgetting anyone, but you know who you are. Thank you. It has been a pleasure.

Equally, the Marie Curie cohort also deserves a whole paragraph. We did not meet very often, but it always felt like meeting your best friends who you have not seen in a while. You are brilliant, each and every one of you, and I am sure you will go on to do wonderful things, in science or otherwise. Thank you so much for sharing a bit of your life with me.

Finally, thanks to my very best friend in the world (and my brother!), Luciano, my sister Tatiana, and to my parents, Liacy and Eduwaldo. Anything said here would not be enough. It is way more than "help and support throughout these years". They went through a lot so that I could be here right now, and that is a debt I can never repay.

Declarations

This thesis is submitted to the University of Warwick in support of my application for the degree of Doctor of Philosophy. It has been composed by myself and has not been submitted in any previous application for any degree.
The work presented (including data generated and data analysis) was carried out by the author, except where indicated in the text.

Abstract

In this work, we aim to understand the behaviour of filaments and bundles of filaments in the presence of diffusible cross-linkers; we posit that these are analogues of the structures present in the Z-ring, with special focus on *E. coli*. Then, we study these structures by constructing a mathematical model based on statistical mechanics, and analysing its behaviour under different ranges of parameters.

We show that the ring-like geometry of the division plane is conducive to constriction, and that this effect can be potentialised by the dynamics of depolymerisation. Furthermore, we show that percolating bundles of filaments are also capable of constriction, and that percolation is necessary but not sufficient for a contractile force to arise. Finally, we investigate how such a model can originate percolating bundles of filaments and how to maximise the contractile potential of such bundles. Concomitantly, we investigate the mutant ftsZ84, an *E. coli* mutant with uncommon properties that might help us understand the relationship between FtsZ assembly and bacterial cell division, by using a new experimental approach. Though the results prove inconclusive, we were able to confirm that the activity of this mutant agrees with the published literature.

Chapter 1

Introduction

Since germ theory of disease became widely accepted, the search for new antimicrobial drugs has been in the minds of scientists [Wright, 2007]. After the work of Pasteur and Koch in the 19th century [Evans, 1978], the rapid discovery of new drugs in the 20th century marks one of the biggest advances in medical science in human history.

Arguably, the apex of this process came in the 40s, 50s and 60s, when many classes of natural antibiotic compounds were discovered. Since then, there was a shift towards modifying the drugs already in use chemically [Wright, 2007]. Even if new compounds have been introduced in clinical environments, no new class of antibacterial compounds has been discovered since daptomycin in 1987 [Silver, 2011].

This lack of new drugs is a major concern due to the spreading of antibacterial resistance amongst bacteria that are relevant in clinical contexts. As these become more and more widespread, there are no new compounds to be used as replacements to the now ineffective ones for treating patients.

Indeed, many antibiotic-resistant bacteria are already of note for being serious threats: *Mycobacterium tuberculosis* and *Neisseria gonorrhoeae* exist as multidrug-resistant strains, a methicillin-resistant *Staphylococcus aureus* strain known as MRSA is common and vancomycin-resistant *Enterococci*, Carbapenen-resistant *Enterobacteriaceae* and penicilin-resistant *Streptococcus pneumoniae* are also of note [Anonymous, 2013; Wright, 2007; Chopra, 2012].

The current targets for antimicrobial compounds are varied. These targets can be classified into three groups: RNA synthesis (rifamycins, mainly in-

hibiting RNA polymerase), DNA synthesis (fluoroquinolones, inhibiting DNA topoisomerase) and cell wall synthesis (beta-lactams inhibiting PBPs and glycopeptides inhibiting transpeptidases). To this day, no compounds to reach market have specifically targeted the prokaryotic cell division machinery, though[Kohanski et al., 2010].

This machinery, also known as the divisome [Den Blaauwen et al., 2008], is a large complex comprising more than 20 proteins, as it can be seen on Fig. 1.1. It assembles at the division site at the middle of a cell inside the membrane after FtsZ assembles into filaments, forming a ring-like region known as the Z-ring [Typas et al., 2012; den Blaauwen, 2013; Egan and Vollmer, 2013]. These filaments are attached to the membrane through anchor proteins ZipA and FtsA [Pichoff and Lutkenhaus, 2002], and the Z-associated proteins provide extra structure to this complex [Galli and Gerdes, 2012; Durand-Heredia et al., 2011, 2012].

This initial assembly, then, recruits other proteins to participate in peptidoglycan synthesis outside the membrane. By co-localizing the cell wall synthesis machinery with the Z-ring scaffold, the cell guarantees that the whole cell wall is suitably remodelled when the Z-ring contracts and, finally, creates a septal region in mid-cell, finishing the division of one cell into two daughter cells [Typas et al., 2012; den Blaauwen, 2013; Egan and Vollmer, 2013].

The cornerstone of the Z-ring, FtsZ is largely conserved in bacteria, essential to its division and present very little redundancy in function. At the same time, it has no direct homologue in human cells [Silver, 2011]. As such, it is, in theory, an excellent antibiotic target. Furthermore, it is only one of several proteins in the divisome to share these characteristics [den Blaauwen et al., 2014].

It is, therefore, essential to understand the mechanisms involved with prokaryotic cell division if we want to develop the antimicrobial drugs of the future. In this work, we aim to understand the behaviour of filaments and bundles of filaments in the presence of diffusible cross-linkers; we posit that these are analogues of the structures present in the Z-ring, with special focus on *Escherichia coli*. Then, we study these structures by constructing a mathematical model and analysing its behaviour under different ranges of parameters.

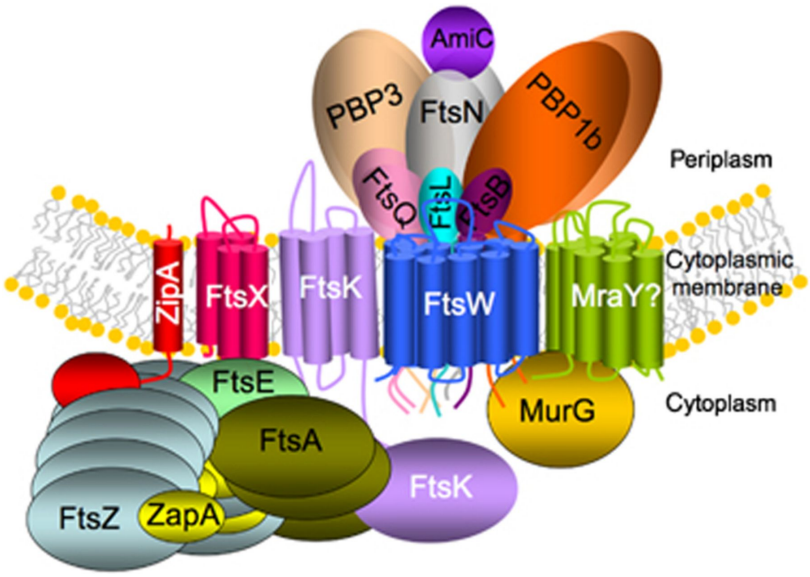

Figure 1.1: A schematic representation of the divisome complex. These proteins control cytokinesis in bacterial cells. Transmembrane domains are represented by cylinders [Den Blaauwen et al., 2008].

Concomitantly, we investigate the mutant ftsZ84, an *E. coli* mutant with uncommon properties that might help us understand the relationship between FtsZ assembly and bacterial cell division, by using a new experimental approach. Though the results prove inconclusive, we were able to confirm that the activity of this mutant agrees with the published literature.

1.1 Bacterial cell division

Scientists have been trying to understand prokaryotic cell division at least since the 1960s. Then, *E. coli* mutants were able to replicate and segregate chromosomal DNA but could not achieve division. This is the origins of the nomenclature "fts": it stands for filamentous temperature-sensitive [Van de Putte et al., 1964; Hirota et al., 1968]. Under certain temperature ranges, these cells would not be able to divide and would grow to form long filaments that eventually died.

With advances in gene fusion, two-hybrid assays and fluorescence microscopy, a lot of research has been produced since those days. Many proteins

were shown to be required for correct cell division, and the workings of the large complex known as the divisome was slowly put together piece by piece [Goehring et al., 2005].

However, studying membrane proteins is not simple, and the fact that many of the mutations cause cell death is a significant obstacle - it is not possible to investigate the effects of a mutation in loss of functions if the cell does not survive. In this context, temperature sensitivity was key to performing studies. Cells could, then, be grown at temperatures where these mutants would not cause negative effects, and then be changed to temperatures where loss of function occurs [Pichoff and Lutkenhaus, 2002; Goehring et al., 2005; Allen et al., 1974; Addinall and Lutkenhaus, 1996; Addinall et al., 1997].

The contraction of the Z-ring is the very last step in the cell division process, occurring after chromosomal replication and segregation. Different bacteria produce cell wall in midcell at different points of this cycle; *E. coli* does it while invagination of the membrane occurs due to the contractile Z-ring, while Gram-positive bacteria sythesize cell wall before invagination occurs [Den Blaauwen et al., 2008; Typas et al., 2012; Egan and Vollmer, 2013].

A key discovery about the organization of the divisome appears for the first time in 1991 [Bi and Lutkenhaus, 1991]. In that, it is reported that FtsZ localizes to the midcell and remains at the leading edge during cytokinesis, and that it is the most abundant and the first part of the cell division apparatus. After that report, the behaviour of FtsZ and the piecemeal assembly of the bacterial division machinery have been analysed by many different studies [Stricker et al., 2002; Anderson et al., 2004; Chen and Erickson, 2005]. Measurements proving that FtsZ generates contractile forces *in vitro* [Osawa et al., 2008] have solidified its position as both scaffolding and driver of cytokinesis.

The fact that the Z-ring is very dynamic is essential to understand prokaryotic division. The FtsZ monomers exchange with the cytoplasm constantly and very quickly; when studied using fluorescence recovery after photobleaching (FRAP), the Z-ring recovers from photobleaching with a half-life of 10 to 30 seconds [Stricker et al., 2002; Anderson et al., 2004; Chen and Erickson, 2005].

In *E. coli*, there are at least 20 proteins involved in the bacterial division process. Of those, many are actually essential for survival: FtsZ, ZipA, FtsA,

FtsK, FtsQ, FtsL, FtsB, FtsW, FtsI/PBP3 and FtsN. Other proteins still localise at midcell during division and participate on it, but are not essential. FtsZ is the first protein to correctly localise to the division site and, in fact, has been shown to be necessary for the other proteins to correctly localise [Goehring et al., 2005].

By fluorescently labelling each individual component of the divisome, it was possible, then, to discern in which order the relevant proteins were recruited and their localization. As previously mentioned, FtsZ is the first protein to arrive at the division site; it is, then, followed by FtsA and ZipA, both acting as anchors for the FtsZ filaments to the membrane, and localising independently from each other [Pichoff and Lutkenhaus, 2002]. Next, FtsEX localises to midcell [Schmidt et al., 2004; Corbin et al., 2007], with FtsK [Wang and Lutkenhaus, 1998; Chen and Beckwith, 2001], FtsQ [Chen et al., 1999], FtsL/FtsB [Ghigo et al., 1999], FtsW [Mercer and Weiss, 2002], FtsI/PBP3 [Weiss et al., 1999] and FtsN [Chen and Beckwith, 2001] following that, in order.

This sequential recruitment of proteins looks quite simple, but the specific mechanisms of assembly are not necessarily so. It is not clear whether each recruited protein interacts only with the one recruited immediately before or with that protein and one or more of the other ones previously recruited; in fact, there is some evidence supporting the idea that a complex network of interactions might be the case here. Some proteins interact independently of the other ones, some might form complexes before localising and changing the order of recruitment seems to affect some proteins rather than others [Goehring et al., 2005; Fraipont et al., 2011; Buddelmeijer and Beckwith, 2004].

In spite of many of those proteins being essential for division to work, there seems to be at least some degree of overlapping in function between them. Deletion of one of the encoding genes can sometimes be compensated by overexpressing a different protein. That is the case, for example, with FtsK: when deleted, restoration occurs by overexpressing FtsAZ, FtsQ, ZipA, FtsB and FtsN [Geissler and Margolin, 2005]. In this case (as in other examples where division can be recovered), the bacteria are viable again, although with a remaining degree of defect.

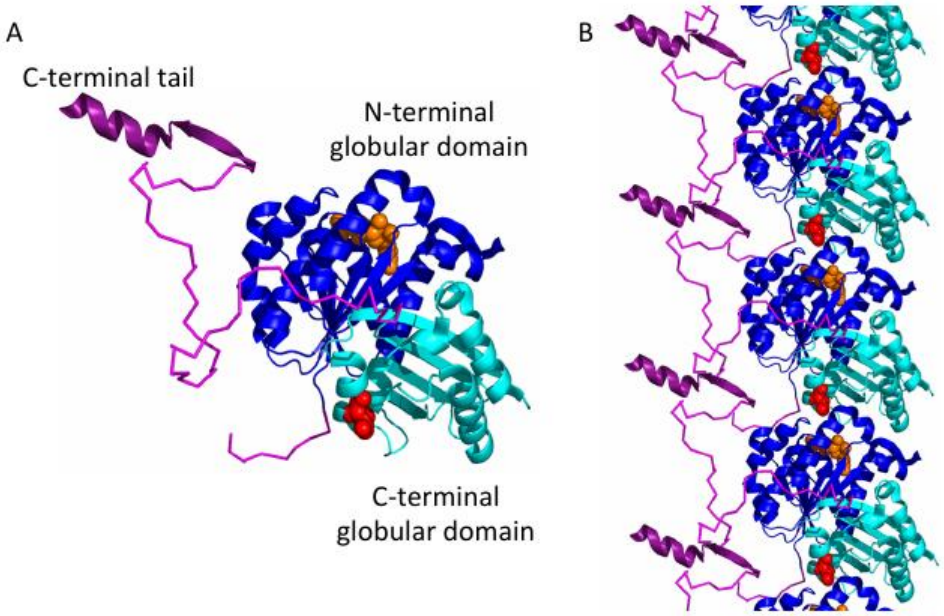

Figure 1.2: FtsZ structure from the bacteria *Pseudomonas aeruginosa*. A) Monomeric FtsZ crystal structure with a bound GDP molecule presented in orange. B) FtsZ polymer structure, predicted from stacking monomers [Erickson et al., 2010; Cordell et al., 2003].

1.2 FtsZ

FtsZ is a protein with approximate mass of 40 kDa. In spite of having only 10-18% of amino acid similarity, it presents nearly the same folding structure as eukaryotic tubulin [Löwe and Amos, 1998; Nogales et al., 1998]. FtsZ is a guanosine-5'-triphosphatase (GTPase), with an active site for GTP hydrolysis [RayChaudhuri and Park, 1992; de Boer et al., 1992] being formed when it forms head-to-tail polymers [Scheffers et al., 2001, 2002]; the interaction between neighbouring monomers and subsequent polymerisation occur in the presence of GTP, as evidenced by Fig. 1.2, and the depletion of GTP when hydrolysis occurs causes dissociation of polymers *in vitro* [Mukherjee and Lutkenhaus, 1998].

FtsZ polymers exist in many different conformations and lengths. In the presence of guanosine-5'-diphosphate (GDP), it could form tubes with the polymers curving into a helical shape [Mukherjee and Lutkenhaus, 1998; Erick-

son et al., 1996; ; Bramhill and Thompson, 1994]; when GTP and diethylaminoethyl-dextran [Erickson et al., 1996] or Ca^{2+} [Yu and Margolin, 1997], FtsZ seems to form straight filaments, that could then be grouped into flat sheets. Adding magnesium or potassium ions to the buffer seems to improve polymerisation [RayChaudhuri and Park, 1992; de Boer et al., 1992; Chen et al., 2005]. Simulating the crowded environment of a cell caused the protein to assemble into thick ribbons with lateral interactions when bound to GTP, with no significant assembly in the presence of GDP [González et al., 2003]. While it is not clear in which of these many forms FtsZ is present *in vivo*, it is thought that filaments bound to GTP seem to be the basic building block.

1.2.1 FtsZ assembly

The assembly of polymers can be either isodesmic or cooperative. In isodesmic assembly, each monomer addition when elongating the polymer has the same rate (or affinity) as any other addition. Due to that, isodesmic assembly leads to average polymer length that increases with protein concentration and to polymer formation occurring at any concentration [Huecas et al., 2008]. On the other hand, cooperative assembly means that a critical concentration exists: under this concentration, no assembly occurs and only the monomeric species exist. Above the critical concentration, polymers and monomers coexist, and monomers are incorporated into polymers until their concentration falls below the critical one [Romberg et al., 2001].

Cooperative assembly has been reported multiple times for FtsZ. The exact critical concentration largely depends on the specific buffer being used for the polymerisation reaction; it has been reported from $0.31\mu M$ (pH 6.5, $2.5mM$ magnesium) to $2.9\mu M$ (same conditions without magnesium) [Caplan and Erickson, 2003]. These values, though, are much lower than predicted *in vivo* concentration of FtsZ in *E. coli* cells; that can range from 3.5 to $15\mu M$ [Rueda et al., 2003; Pla et al., 1991; Lu et al., 1998]. More supporting evidence for the cooperative assembly of FtsZ comes from studies with a GTP-regenerating system, where analysis of sedimentation velocities show a bimodal distribution with a slowly-sedimenting species containing monomers and dimers and a fast-sedimenting species with long polymers [González and

Vélez, 2005].

It is not immediately obvious how a single-stranded filament can present cooperative assembly. Previously, cooperative assembly could be explained by having monomers interacting with multiple subunits after a dimer is formed [Miraldi et al., 2008]; that works for multi-stranded and helical filaments, but not for single-stranded ones. Modelling work showed that the assembly data could be fitted to either a system including monomer activation, dimer nucleation and elongation or a system where monomers need to be activated before nucleation occurs; dimer formation, then, requires two activations, while elongation requires only one [Chen et al., 2005; Miraldi et al., 2008].

1.2.2 Z-ring structure and *in vitro* work

As previously mentioned, the first study to show FtsZ localisation during bacterial division comes from 1991, where cells were immuno-gold labelled and imaged with electron microscopy. That study showed, also, that FtsZ remains at the leading edge of the constricting furrow. Due to limitations in resolution and the cytoplasmic density, it was not possible, then, to investigate Z-ring dynamics *in vivo* [Bi and Lutkenhaus, 1991].

Green Fluorescent Protein (GFP) came along and, then, it was possible to use fluorescence light microscopy (FLM) to image FtsZ molecules. Though the FtsZ-GFP fusion is not functional, it was possible to express that fusion at a low level while keeping most of the wild-type protein intact. FtsZ, then, showed as a bright band at the centre of the cell, indicating a closed ring structure [Addinall and Lutkenhaus, 1996]. The resolution to see individual filaments, though, was still not there; the best that could be done was to measure the Z-ring width, at roughly 100nm [Fu et al., 2010].

We can see how the Z-ring contracts and, then, disassembles on figure 1.3. Interestingly, disassembly seems to start before scission is completed, and new rings seem to start forming at the future daughter cell division sites [Sun and Margolin, 1998].

While these studies give us some insight into the dynamics of the Z-ring, its structure cannot be probed by simple fluorescence microscopy due to the diffraction limit. However, three-dimensional structured illumination

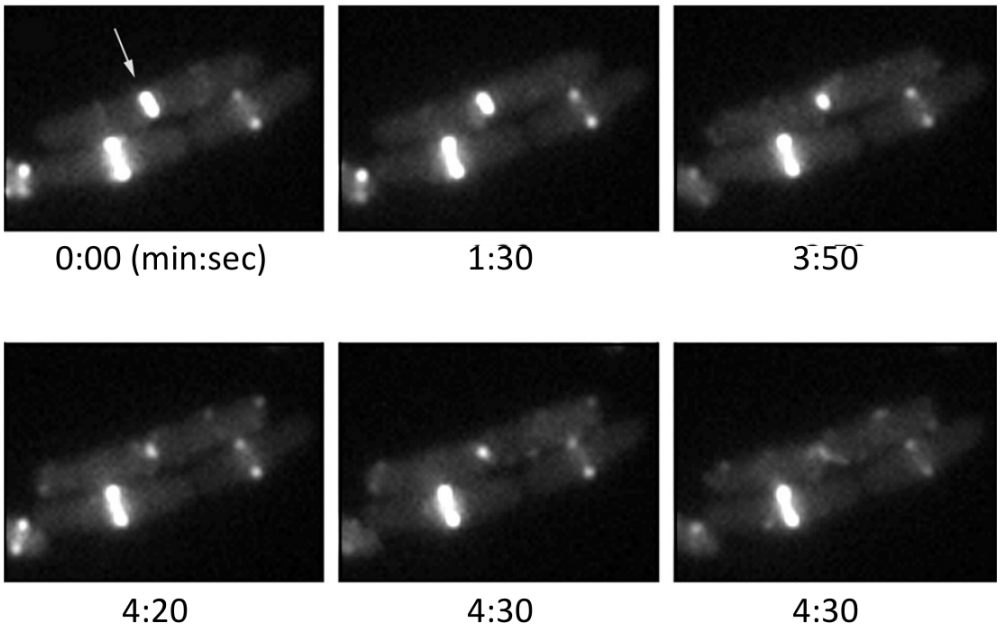

Figure 1.3: In this experiment, Erickson *et al.* show constriction and disassembly of the Z-ring from the centre of the cell during bacterial division [Erickson et al., 2010].

microscopy (3D-SIM) was able to give us some evidence regarding the particulars of Z-ring formation and composition - FtsZ patches with short filaments orientated randomly were observed. In addition to that, there were significant gaps within the Z-ring region where FtsZ concentration was either low or non-existent; similar patterns were seen upon labelling of FtsA and ZipA [Rowlett and Margolin, 2014].

Indeed, *E. coli* is not alone in presenting this structure. Both *B. subtilis* and *S. aureus* also showed Z-ring regions where no FtsZ was apparent [Strauss et al., 2012]. The general structure of high-density regions linked by low-density stretches was dynamic before and during cytokinesis. In fact, complete, continuous rings were only seen in *C. crescentus* when DNA damage occurred; these rings did not contract, suggesting that the gap regions are important for constriction [Holden et al., 2014].

Some further advancement in resolving the structure of the Z-ring comes from a work in 2007 that uses electron cryotomography (ECT) on *C. crescentus*, showing an arrangement of FtsZ filaments of approximately 100nm in length in the midcell region [Li et al., 2007]. These filaments were single or double stranded, and most of them oriented perpendicularly to the long axis of the cell. While the low number of filaments in this work seems to be at odds with the amount of FtsZ in other studies, this was the best resolution available for the Z-ring structure.

Some more clarity on this issue was achieved by utilizing electron cryotomography in both *E. coli* and *C. crescentus*: by observing division sites and reconstructing the three-dimensional structures obtained by tomography, it was possible to discern the Z-ring as composed of a small, single-layered band of filaments that create a continuous ring-like structure through lateral interactions. While the individual filaments to not span the whole circumference of the cell, dividing Z-rings do so through overlapping many filaments [Szwedziak et al., 2015].

While many groups tried to resolve the structures involved in the Z-ring *in vivo*, some others tried to establish the nature of the ring through *in vitro* work. Notably, Osawa *et al.* was successful at creating an FtsZ fusion that included a membrane-targeting sequence, making anchor proteins unnecessary [Osawa et al., 2008]. Then, that protein was added to tubular, multi-lamellar

vesicles. When GTP was added, dynamical ring-like structures were formed on the inside of the vesicles. These structures semmed to pull the membrane inwards. When GTP was depleted, these structures relaxed and dissociated. It is important to note, though, that the contractile process did not achieve complete scission, indicating that FtsZ, by itself, is not enough to complete division. Also, the mechanism through which FtsZ caused contraction was not clear.

Further work created a similar fusion protein and localised it on the outside of vesicles. In this case, FtsZ in the presence of GTP was able to cause concave membrane depressions, while by moving the membrane targeting sequence around the FtsZ structure, from C-terminus to N-terminus, produced convex indentations instead [Osawa et al., 2009]. These results indicate that the FtsZ filaments possess some intrinsic curvature, and that they can pull the membrane to their curvature.

Finally, the same group was also able to create "inside-out rings" by introducing the flipped version of the FtsZ fusion protein to the outside of tubular liposomes. Instead of pinching the membrane from the inside, these rings were able to "press" it inwards from the outside in. Contraction seemed at least partially dependent on GTP hydrolysis; using the non-hydrolysable GTP analogue guanosine-5'-[(α, β)-methyleno]triphosphate (GMPCPP) yielded some constriction, but not as much as with GTP present. By using GMPCPP, subunit exchange was also prevented, and photo-bleaching recovery was arrested [Osawa and Erickson, 2011]. Electron micrographs of these structures showed ribbons of FtsZ filaments that were closely packed, but still presented gaps, indicating that lateral FtsZ interactions might take place [Milam et al., 2012].

1.2.3 FtsZ regulation and localization

The spatial regulation of FtsZ (and its colocalizing membrane anchor proteins FtsA and ZipA) and the control of polymerisation over time is done through interaction with other intracellular molecules. The concentrations of FtsZ, FtsA and ZipA in *E.coli* are thought to not change significantly over time during the cell cycle [Rueda et al., 2003]. Positive and negative regulators of FtsZ have been pinpointed, though it is likely that more are yet to be identified

[Bailey et al., 2014; Tsang and Bernhardt, 2015].

In *E. coli*, there are three main systems for regulation of FtsZ activity: SulA, the Min system and nucleoid occlusion. SulA is a protein that is expressed when the cell detects DNA damage, being a part of the stress response system [Huisman et al., 1984; Janion, 2008]. It stops the Z-ring from being formed, such that the cell will not divide before the genetic damage is repaired [Dajkovic et al., 2008; Chen and Erickson, 2011; Mukherjee et al., 1998]. SulA acts to prevent FtsZ polymerisation, and normal cell function is quickly restored when its gene is no longer expressed [Janion, 2008; Mizusawa and Gottesman, 1983].

Contrary to SulA, the other two systems are not conditional: they are at work at all times during the cell cycle. Combined, they aim at restricting FtsZ activity to midcell, ensuring the correct positioning of the Z-ring and the division plane and avoiding unequal splitting of the genetic material upon division [Bi and Lutkenhaus, 1990; De Boer et al., 1990].

The Min system is designed to prevent the Z-ring from forming close to the cell poles. When this system is inactivated, bacterial division forms "minicells", small bodies without nuclear material [de Boer et al., 1989]. The other side of the division septum is a longer than wild-type cell with multiple nucleoids, indicating that the divisome can only assemble at one place per cycle [Bi and Lutkenhaus, 1990; De Boer et al., 1990].

To achieve that goal, the Min system requires three proteins: MinC, MinD and MinE [Lutkenhaus, 2007]. MinD is a protein that associates to the membrane and oscillates across the cell, from one pole to the other. The switching time in these oscillations are of the order of 10-30 seconds, with the exact cycle time depending on the ratio between MinD and MinE. Furthermore, the oscillations only occur in the presence of MinE [Raskin and de Boer, 1999].

MinE itself accumulates around midcell and seems to promote dissociation of MinD from the membrane, then moving towards one of the poles. MinD is, then, forced to go to the opposite pole, and MinD reforms around midcell and follows the same process in the other direction [Hale et al., 2001].

Finally, MinC follows the same pattern as MinD, but it is not necessary for the oscillatory behaviour to form [Hu and Lutkenhaus, 1999]. It is, however,

the effective inhibitor in this system; it is MinC, and not the other two, that stops FtsZ from polymerising. Since MinC oscillates from pole to pole just like MinD, the time averaged concentration of it is a gradient with minimum around midcell, making it the most likely place for FtsZ to polymerise and for the Z-ring to be formed [Hu et al., 1999].

The other permanent mechanism for establishing the correct positioning of the Z-ring is nucleoid occlusion. Its main objective is to stop the Z-ring from forming over the genetic material (or nucleoid) of the cell, ensuring that genetic material replication and segregation is completed before cytokinesis and that the correct division of the nucleoid between daughter cells is made [Wu and Errington, 2012].

The first protein involved in nucleoid occlusion to be identified was *B. subtilis* Noc [Wu and Errington, 2004], while in *E. coli* the involved protein is SlmA [Bernhardt and De Boer, 2005]. They both bind to DNA and inhibit FtsZ polymerisation locally. Importantly, both these proteins do not bind to the replication termination region (Ter) in the DNA; that ensures that, as chromosomal replication ends, the concentration of these proteins at midcell falls while the chromosomes are segregated [Wu et al., 2009; Tonthat et al., 2011].

In *E. coli*, MatP is another protein involved with the correct localization of the Z-ring. It binds to a specific DNA sequence in the Ter region of the chromosome [Mercier et al., 2008] and then interacts with ZapB in the presence of ZapA, acting as a signalling agent for the correct positioning of the divisome [Espéli et al., 2012].

1.3 Contractility during cytokinesis

The central, defining feature of cytokinesis in bacteria is that, contrary to eukaryotic cell [Maupin and Pollard, 1986], it does not seem to rely on any motor protein; no such protein has been identified in prokaryotes. Furthermore, it has been shown that FtsZ itself is capable of generating at least some contractile force [Osawa et al., 2008]. The only existing theoretical criterion for models of contractility of the Z-ring is due to Lan *et al.* who estimated the minimum force necessary to drive bacterial division to be 8 pN. That value is

relatively small when compared to the forces generated by eukaryotic motor proteins, and it takes into account the cell wall growth that goes together with constriction [Lan et al., 2007].

There are still several models for the origin of the contractile force in the Z-ring. One of the leading theories proposes that multiple filaments might anneal to form a large one that is able to span the whole circumference of the cell, that then contracts through increasing lateral interactions by filament sliding [Erickson et al., 2010]. There are essentially three arguments against this mechanism: the fast dynamics of FtsZ assembly and disassembly [Stricker et al., 2002; Anderson et al., 2004; Chen and Erickson, 2005], the apparent presence of lower-density FtsZ regions in the Z-ring [Rowlett and Margolin, 2014; Strauss et al., 2012; Holden et al., 2014] and the many lateral bonds that would need to be broken for sliding to proceed, making this process too slow to account for the contractility observed *in vivo* [Erickson, 2009].

A competing theory postulates that FtsZ filaments can bind to the membrane as GTP-bound, straight filament and, upon GTP hydrolysis, convert to a GDP-bound, curved conformation, exerting an inward force locally. Through "iterative pinching" around the whole cell, a sustainable contractile force could be generated, with constant depolymerisation and re-binding of the FtsZ polymers central to this mechanism [Li et al., 2007]. Some *in vitro* work seems to show that, in the presence of GTP (and DEAE-dextran), FtsZ formed straight filaments, tubes and mini-rings, while the non-hydrolysable GMPCPP (and DEAE-dextran) caused only straight filaments to appear, and GDP (and DEAE-dextran) formed curved tubes and mini-rings. This points towards GTP-bound interfaces being straight, and GDP-bound ones being curved [Erickson et al., 1996; Lu et al., 2000]. It is important, though, to mention that curved FtsZ structures seem to appear only when surfaces are present, making the possibility of surface-related artefacts difficult to neglect.

However, the differences in structure necessary for this hypothesis to be sustained have not been seen when comparing the GDP and GTP-bound monomer structures. FtsZ structure from *M. tuberculosis* showed that the T3 loop changes from a tensioned to a relaxed state when hydrolysis occurs [Li et al., 2013], and molecular dynamics simulations of the *M. jannaschii* FtsZ protein showed that the GDP-bound monomer lost some of its protein-

protein interactions when compared to the GTP-bound one, making it less stable [Hsin et al., 2012]. When added to the multiple structures seen from FtsZ *in vitro* [RayChaudhuri and Park, 1992; de Boer et al., 1992; Mukherjee and Lutkenhaus, 1998; Erickson et al., 1996; Yu and Margolin, 1997; Bramhill and Thompson, 1994; Chen et al., 2005; González et al., 2003], there is no conclusive evidence that this is the actual mechanism at work in bacteria.

1.4 FtsZ as Antibacterial target

As previously mentioned, good antibiotic targets would include those that are largely conserved in bacteria, essential to its division and have very little redundancy in function. At the same time, they should have no direct homologue in human cells [Silver, 2011]. Indeed, FtsZ obeys all of those requirements; any molecule capable of inhibiting FtsZ will probably make bacterial cells inviable [Egan and Vollmer, 2013].

The homology relationship between FtsZ and eukaryotic tubulin is of concern; however, the difference in amino-acid sequence is likely to be significant enough to make the design of molecules with FtsZ specificity possible [den Blaauwen et al., 2014].

There are multiple ways a molecule could inhibit FtsZ function and, therefore, disrupt cell division. It could block the interaction of FtsZ with other proteins by targeting its C-terminal; it could mimic SulA and interact with FtsZ at the T7 loop to block polymerisation; it could stabilise the filaments and prevent depolymerisation, stifling the fast dynamics of the Z-ring; it could compete with GTP at the nucleotide-binding site, though that would risk affecting function of other processes that require GTP inside the cell [den Blaauwen et al., 2014].

Many small molecules capable of inhibiting FtsZ have been discovered, both synthetic and natural, using multiple techniques like high-throughput *in vitro* assays, computational and structural design and whole-cell filamentation tests. However, no antibiotic drug targeting the apparatus involved in cell division has reached the market yet. This is due to the fact that simply discovering an inhibiting molecule is not enough: pharmacokinetics and drug availability at the target cells are considerations that need to be taken

into account when developing market-ready drugs [den Blaauwen et al., 2014; Anderson et al., 2012].

One example of a synthetic molecule with potential to become an FtsZ-targeting antibacterial drug is PC190723 (3-[(6-chloro[1,3]thiazolo[5,4-b]pyridin-2-yl)methoxy]-2,6-difluorobenzamide). This compound is an analogue of 3-methoxybenzamide (3-MBA), a molecule suggested to target FtsZ [Ohashi et al., 1999]. PC190723 was shown to inhibit both *B. subtilis* and *S. aureus* (in this case, even single and multi-drug resistant strains). It was also not toxic to human hepatocytes [Haydon et al., 2008; Tan et al., 2012]. In addition to that, 100% of mice survived when given a single intravenous dose of PC190723 in a mouse model of *S. aureus* infection, as opposed to 0% of mice without treatment [Haydon et al., 2008].

It is suspected that the mechanism of action of this molecule is stabilising FtsZ filaments to promote polymerisation. The critical concentration, then, disappears, and so does the cooperative aspect of FtsZ polymerisation [Elsen et al., 2012]. In addition to that, it has been shown that FtsZ localises wrongly in the presence of PC190723, with multiple rings and arcs appearing in places outside the midcell [Haydon et al., 2008; Tan et al., 2012]. However, these effects have not been replicated in *in vitro* studies with *E. coli* FtsZ, and *E. coli* does not seem to be susceptible to the molecule [Haydon et al., 2008; Andreu et al., 2010].

On the naturally-produced side, a good example of FtsZ-targeting molecule is viriditoxin. It was identified from screening over 100,000 natural extracts of fermented broths and plants. While a synthesized version [Park et al., 2011] of viriditoxin was not active against *E. coli* and *B. subtilis* [Anderson et al., 2012], the purified version from *Aspergillus viridinutans* fermentation broth was successful at inhibiting growth of *Staphylococcus*, *Enterococcus* and *S. pneumoniae* and all of its single and multi-drug resistant strains. It appears to do so by inhibiting polymerisation and GTPase activity [Wang et al., 2003].

These compounds have as a common trait the ability to disrupt the assembly of the Z-ring. This can be achieved by inhibiting polymerisation or depolymerisation. However, inhibiting FtsZ activity by stopping protein-protein interactions has not been a successful endeavour. Small molecules will always struggle to disrupt these interactions due to the large areas of

the proteins that can be buried when that interaction occurs [Tsao et al., 2006]. Some progress has been made in finding compounds that can disturb the FtsZ:ZipA interaction, and a crystal structure analysis of one of these compounds showed that, indeed, it can bind to ZipA at the FtsZ binding site [Kenny et al., 2003].

1.5 Membrane anchors

The two proteins that co-localize with FtsZ to midcell early and anchor it to the membrane are ZipA and FtsA. ZipA is an inner membrane protein with a single transmembrane domain, colocalizing with FtsZ and remaining in midcell until the end of cytokinesis [Hale and de Boer, 1997]. *In vitro*, it can also promote bundling of FtsZ filaments [RayChaudhuri, 1999] without affecting GTPase [Liu et al., 1999]. Furthermore, ZipA also is necessary for the correct localisation of other proteins in the divisome [Pichoff and Lutkenhaus, 2002]. The structure of ZipA C-terminal domain was resolved my both NMR spectroscopy and X-ray crystallography [Moy et al., 2000; Mosyak et al., 2000]. Interestingly, a 20-Åcavity exists, where the C-terminal from FtsZ binds [Mosyak et al., 2000].

Working in parallel to ZipA, FtsA is a protein with an amphipathic helix at its C-terminal, anchoring FtsZ to the inner membrane through a membrane targeting sequence [Pichoff and Lutkenhaus, 2005]. Just like ZipA, FtsA is also necessary for the localization of divisome proteins [Pichoff and Lutkenhaus, 2002; Karimova et al., 2005] and localizes to the midcell region roughly at the same time as FtsZ [Addinall and Lutkenhaus, 1996].

Just like FtsZ is a prokaryotic analogue of tubulin, FtsA is a prokaryotic analogue of actin [Bork et al., 1992]. Thus, it is part of a family of ATPases. There is some evidence of FtsA protofilaments being formed during division, and it has been shown to happen in the presence of ATP in *in vitro* studies using *S. pneumoniae* FtsA, but with no apparent ATP hydrolysis activity [Lara et al., 2005]. On the other hand, by using *B. subtilis* FtsA, ATPase activity was detected in dimers [Feucht et al., 2001]. Co-crystallisation of *T. maritima* with a non-hydrolysable analogue of ATP (adenosine-5'-[γ-thio]triphosphate, or ATP-γ-S) showed continuous filaments in the crystal [van den Ent et al.,

2001].

Adding FtsA and FtsZ to supported lipid bilayers and following their locations using total internal reflection fluorescence (TIRF) microscopy, it was possible to note the formation of bundles of filaments moving in one direction upon addition of GTP and ATP or ATP-γ-S. Another dynamic structure observed were vortices that always rotated clockwise, with diameters that were fixed and around $1.09 \pm 0.24\mu m$. This specific kind of dynamics were only present with FtsA; substituting it for ZipA did not yield the same results [Loose and Mitchison, 2014].

Further work by Bisson *et al.* uncovered further interesting dynamics related to the FtsZ-FtsA vortices seen in supported lipid bilayers; the movements of both these proteins relative to the dynamics of cell wall synthesis during division were imaged *in vivo*. FtsZ was shown to treadmill in circumferential paths around the Z-ring region, while FtsA co-localizes with it. Both these proteins seem to pull along the cell-wall-synthesizing enzymes. The rate of treadmilling controls cytokinesis and the rate of cell wall synthesis, meaning that treadmilling guides the insertion of cell wall in small concentric rings.[Bisson Filho et al., 2016] This is further proof of the varied and complex effects that proteins like FtsA can have on the organization and dynamics of the Z-ring.

1.6 Bundling Agents

A number of proteins have been shown to stabilize FtsZ filaments and promote filament bundling, at least in *in vitro* studies. As previously mentioned, one of those proteins is ZipA: it has been shown to facilitate the formation of bundles of FtsZ filaments [RayChaudhuri, 1999] while not affecting GTP hydrolysis activity to any degree [Liu et al., 1999].

Another protein that can present similar function when observed *in vitro* is ZapA. This is one of the proteins that are accessory to cell division, first found in *B. subtilis*. It is, though, present in a large range of bacteria [Gueiros-Filho and Losick, 2002]. It is relatively small, at about 10 kDa, and about 100Å long. A detailed crystal structure of *Pseudomonas aeruginosa* indicates it is an anti-parallel tetramer, presenting four globular domains at

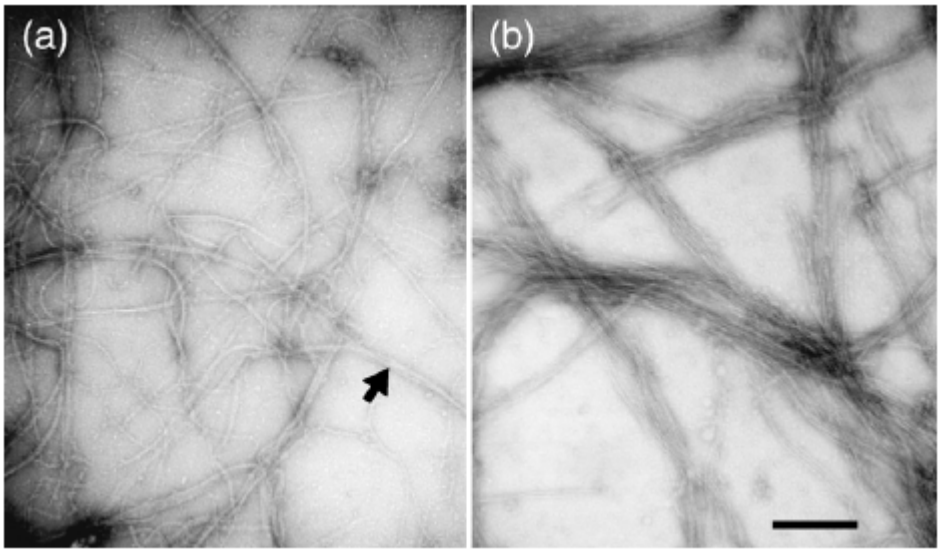

Figure 1.4: Negative stain electron microscopy of FtsZ filaments shows that YgfE induces the formation of bundles. Figure shows (a) individual filaments in the absence of YgfE and (b) bundles in the presence of YgfE. Picture from [Small et al., 2007].

opposite ends of a central stalk [Low et al., 2004].

ZapA is one of the proteins that localise to the division site early in the cell cycle, both in *B. subtilis* and *E. coli*. The *in vivo* activity of ZapA is suggested to be stabilizing the Z-ring; this was a claim first put forward through the genetic experiments that identified ZapA in the first place. It is not clear, though, which part of the protein interacts with FtsZ [Gueiros-Filho and Losick, 2002]. Meanwhile, *in vitro* work showed ZapA binding directly to FtsZ and induces the individual protofilaments to assemble into large bundles. That might be connected to the dimeric or tetrameric nature of ZapA [Gueiros-Filho and Losick, 2002; Small et al., 2007].

In addition to that, *E. coli* possess an ortholog to ZapA in the shape of YgfE, a proteins that has 11% identity and 34% similarity to ZapA. *In vitro* work has showed that YgfE can bind to FtsZ polymers, and that it can enhance polymerisation and induce bundling of protofilaments, as it can be seen in Fig. 1.6. However, as opposed to ZipA, the bundling effect here comes added to a reduction in GTP hydrolysis activity [Small et al., 2007].

While it is not completely clear to which degree these bundling agents act to cross-link FtsZ filaments and how relevant bundles are *in vivo*, it has been shown that the YgfE protein localizes to the Z-ring [Gueiros-Filho and Losick, 2002] and that both ZipA and ZapA do stabilize Z-rings *in vivo* [Gueiros-Filho and Losick, 2002; Liu et al., 1999; Hale and De Boer, 1999].

1.7 Previous FtsZ modelling work

The modelling work regarding FtsZ, its dynamics, polymerisation and the Z-ring formation and contraction is extensive, even if their rationale for the origin of the contractile force in the Z-ring tends to align to the ones presented in Section 1.3. The complexity of these models is quite varied, and so are the results and aims of each model.

For example, one of the models designed to investigate the possible cooperativity of FtsZ polymerisation was developed by Chen *et al.*, where a relatively simple set of ordinary differential equations were developed to model activation, dimerisation and elongation of FtsZ filaments over time. Then, numerical solutions to these equations were obtained, simulating the *in vitro* polymerisation of FtsZ in the presence of GTP. The hypothesis was that early polymerisation was qualitatively different from further elongation. Individual equations for addition of FtsZ monomers up to filament length of 6 were defined, and from the 6-monomer long filament onwards they were just considered as "long" filaments, without explicit length. In this model, no annealing of filaments and GTP hydrolysis are present [Chen et al., 2005; Chen and Erickson, 2005].

Upon solving the equations, it was then possible to fit the polymerisation data from FtsZ to obtain the rate constants involved in the polymerisation process. The data, in this case, was obtained from the mutant FtsZ-L68W, where the fluorescence at 350 nm changes upon assembly, due to a small conformational change affecting how much a tryptophan residue is exposed. From that data, the model indicates a polymerisation process where FtsZ forms a weak dimer as its nucleation step. It is not clear, though, whether extrapolating the data from this mutant to the wild-type is valid, since sedimentation assays indicated a different critical concentration [Chen et al., 2005].

An new assay was, then, developed: fluorescence resonance energy transfer (FRET) was used to probe FtsZ assembly, by introducing a single cysteine to attach either the donor or acceptor fluorophore. This new mutant (FtsZ-F268C) was significantly different from L68W and the rate constants were also different. However, they still indicated that a weak dimer nucleus was the likely explanation [Chen and Erickson, 2005].

Another group took a very different approach to trying to solve the same problem. Huecas *et al.* developed a static model for FtsZ polymerisation, by considering the equilibrium distribution [Huecas et al., 2008]. In this model, the monomer needs to be activated before dimerisation and elongation. Given the relative simplicity of this model, analytical solutions were possible: these were identical to Oosawa's equation for condensation polymerisation [Oosawa and Kasai, 1962].

This result indicates that cooperative polymerisation for the purely linear FtsZ filaments was possible. An extension of this work was developed by Miraldi *et al.*, where polymerisation of activated and non-activated monomers was explicitly modelled [Miraldi et al., 2008]. In addition to an equilibrium constant of activation, four additional constants were defined, for the four possible monomer-monomer interactions that arise from the existence of two species of monomers. It was, then, possible to calculate the polymer concentration and study the cooperative polymerisation, given protein and monomer species concentrations.

The results obtained agreed with Huecas *et al.* [Huecas et al., 2008]: both models predict cooperative polymerisation when the activated monomer is less stable than the inactive one, and when the interaction between two activated monomers is favourable enough to balance the activation step. When the dimerisation of active monomers had a large equilibrium constant and the other four (for the two monomer species) were small, maximum cooperativity was achieved, indicated by a sharp critical concentration [Miraldi et al., 2008]. This goes against the previous work of Chen *et al.*, that postulated a weak dimer [Chen et al., 2005; Chen and Erickson, 2005].

Indeed, as it can be seen from these examples, it is possible to construct multiple models that, given the same inputs, generate outputs that agree with experimental data. Therefore, simply being able to present a good fit to such

data does not guarantee that a model is a valid explanation for the workings of the experimental system [Doucet and Sloep, 1992].

A separate problem that groups tried to solve through modelling was the Z-ring assembly *in vivo*. A kinetic model for binding FtsZ filaments that follow a certain length distribution from the cytoplasm to the membrane was developed by Allard and Cytrynbaum. A barrel-shaped Z-ring and filaments being held together by lateral interactions were assumed. Furthermore, all filaments binding to the membrane are assumed to be GTP-bound, and hydrolysis is assumed only to occur when the filament is bound. The hypothesis for force generation was that of "iterative pinching", where filaments bend when GTP hydrolysis occur [Lu et al., 2000]. The final assumption was that only GDP-bound monomers at the end of polymers can depolymerise from the filaments back to the cytoplasm [Allard and Cytrynbaum, 2009].

A very large proportion of GDP-bound monomers in the Z-ring (53% on average) was observed. That might be an artifact of only incorporating depolymerisation at the ends of a filament and seems at odds with the rapid dynamics of the Z-ring *in vivo*. However, the average residence time of a filament in the Z-ring in this model was 12 seconds, which is in agreement with times measured by fluorescence recovery after photobleaching (FRAP) [Allard and Cytrynbaum, 2009]. The large proportion of GDP-bound monomers also meant the force generated was significant. For cell radii from 25 nm to 400 nm, this was larger than 8 pN, the threshold hypothesised to be enough for deformation of the cell wall to occur [Lan et al., 2007].

A different model was developed by Lan *et al.* [Lan et al., 2009]. This model was more focused on the microscopic, monomer-level interactions: the Z-ring region of the membrane was divided into a two-dimensional lattice, where each side could be empty or occupied by different entities: FtsZ, FtsA, ZipA, FtsA bound to FtsZ and ZipA bound to FtsZ. Then, a Monte Carlo-Metropolis algorithm was applied, accepting changes that decreased the free energy of the system. The calculation of energies was based on binding interactions between monomers of FtsZ, both longitudinally and laterally, and the interactions between FtsZ monomers and the other two proteins. Then, a switch of sorts was introduced, where lateral interactions became more favourable; however, no such switch has been identified in the biology of bacterial cells

yet, and it is not clear whether this mechanism has relevance biologically [Erickson, 2009]. To model expansion and contraction, if a monomer tries to move to an occupied square a new row is added and the circumference of the ring region increases by the size of a monomer. If, when a monomer is removed, an empty row is generated, that row is deleted and the circumference is decreased by the size of a monomer. Since the removal of an empty row is likely to introduce new monomer-monomer interactions, contraction is generally favoured [Lan et al., 2009].

Another idea for abstracting the same system was put forward by Surovtsev *et al.* [Surovtsev et al., 2008]. Polymerisation, Z-ring formation and contraction were also characterised in terms of ODEs, but with end-to-end annealing being allowed and all GDP-bound interfaces having the same likelihood to break down, instead of limiting dissociation to the ends of filaments. These equations were solved for filament lengths of up to 150 monomers. However, the Z-ring was considering as simply consisting of long filaments annealing to form closed polymers, which goes against the current view of the Z-ring as a collective of short, overlapping fibres [Li et al., 2007]. Also, the length of 150 monomers is not enough to span the whole circumference of the cell, so the group assumes the qualitative behaviour of the system scales to cell-size *in vivo*, which might not be the case.

Finally, Dow *et al.* [Dow et al., 2013] developed a mathematical model for the assembly and contraction of the Z-ring in terms of accumulating short linear FtsZ filaments that can associate and dissociate from the membrane. This extends on the previous work by Surovtsev *et al.* [Surovtsev et al., 2008] by including the kinetics of accumulation of FtsZ on the anchor proteins and the physical forces necessary to bend the cell membrane against its surface tension, while tuning some of the model parameters to account for the most recent experimental data. The model is, then, used to predict whether a cell can initiate division and its division outcome, being able to compare that to experimental results for FtsZ mutants and cells without some of the FtsZ-binding proteins.

Chapter 2

Theoretical Methods

2.1 Introduction

While there is a plethora of previous models regarding bacterial division exploring thoroughly the polymerisation, assembly and dynamics of FtsZ filaments, there are fewer models around when it comes to force generation, and these are based on either the role of bending filaments or sliding filaments with lateral interactions.

In this work, we explore the role of cross-linkers in this process; in fact, the results will be general to any bundles of filaments. Other than specific parameter values, there should not be anything in our model that is particular to FtsZ. In particular, some of the inspiration for this work come from experiments cross-linking microtubules, which is one other system where this model could be applied.

In this chapter, we will present how we move from a concept for a model to an actual implementation. We will discuss how the problem at hand is formulated mathematically and physically, how we make sure that it is thermodynamically consistent. In order to calculate the free energy, we must define the entropy and our procedure for sampling microstates.

2.2 Formulation of the problem

The basic building block of our model for bacterial division are filaments. These are collections of protein monomers bound end to end without any gaps. In a digital representation, we will think of a filament as a set of occupied sites next to each other, with unoccupied sites at each end. These are one-dimensional entities in nature, defined by their length only; however, as previously mentioned, lateral overlaps are going to be central to our approach, meaning that we think of these entities as existing in a two-dimensional space (as a membrane environment, for example), with two ends defined by the interfaces of occupied sites with unoccupied ones and sides defined by the sites adjacent to the filament.

The other biological entity directly represented in our system are cross-linkers. These are, essentially, two-headed "stickers" that will bind to the two sides of filaments. Usually, these will be two different filaments, though a filament long enough to wrap around the whole system could in principle be cross-linked to itself. We will come back to the representation of the space where filaments exist in Section 2.2.1.

For convenience, we will define a single point-like position for each of these entities. In the case of filaments, this will be the site occupied by one specific monomer in the chain of connected monomers (we choose the left-most monomer); on the other hand, cross-linkers will have their position defined as the site where the binding between the two sides of filaments occur, using the beginning of the lateral overlap region as a reference point. That means that cross-linkers sitting at the very first site where lateral overlap occurs will have a position value of 0 within that overlap region.

The existence of filaments and cross-linkers will define constraints on the position of other entities in the system. We will discuss the exact constraints and how they are formulated later on Section 2.2.3. The variable is the actual size of the system in terms of total available sites. This is a proxy for the size of the Z-ring region.

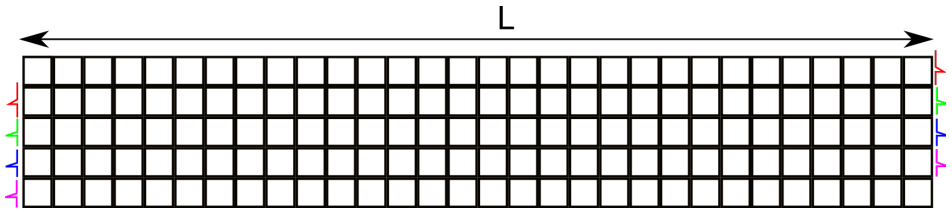

Figure 2.1: The helical structure of the system. We define L as the turn length of the helix and N as the number of turn lengths in the system; in this figure, we have $L = 30$ and $N_{lines} = 5$. We can approximate the radius of curvature of the system R as $R = L/2\pi$; since R should be significantly bigger than the monomer size, that should be an approximation for the average radius of curvature of the filaments in this system. Coloured sections indicate that the right-side "boundary" at the end of the line are, in fact, the same as the left "boundary" in the consecutive line.

2.2.1 The Region of interest

Our choice for defining the system is a quasi-two dimensional lattice. In that way, purely one-dimensional entities can interact with each other, and there will still exist a second dimension for lateral overlap regions and cross-linkers.

We achieve this by defining a long helical region of size LN_{lines}. This helix will have turn length L, meaning that sites that are separated by L sites are next to each other in the second dimension. The system, then, will have exactly N_{lines} turns. Hard walls are incorporated at the beginning and end of the helix so that filaments remain confined into this region, a proxy for the Z-ring region.

We can see a representation of what a long filament in this geometry would look like at Figure 2.1. We can see that a filament with length $L_f > L$ will have a lateral overlap region with itself.

We show a representation of the defined region of interest in Figure 2.2. We can identify an intrinsic radius of curvature of the cell $R = L/2\pi$. If we assume all filaments in the system as aligned to the long direction of the system, this will also define the approximate radius of curvature for the filaments as well. Given that the long direction of the system will typically be much larger in size compared to a filament, we will also assume that no twist or lateral bending is required for the filaments to align correctly to this quasi-two

dimensional lattice. Importantly, we should emphasize that this model will not capture the very final pinching during the division process, where a single cell divides into two.

2.2.2 Internal Representations

We can, now, talk in more detail about the implementation-specific representations of different structures in our system. As mentioned, the filaments are purely one-dimensional structures; therefore, they can be represented by a single integer value, which is its size (i.e., the number of contiguous occupied sites in the lattice, with unoccupied sites before and after it). No particular position will be associated with each individual filament, since our model concentrates on the ensemble properties of systems. The filaments in the system, then, are represented by a one-dimensional list of integer values that indicate the sizes of each filament and in which order they appear in the system. For convenience of implementation, we record the number of filaments currently existent as an integer before the very first size. Therefore, the list

$$\text{filaments} = [5\ 4\ 10\ 1\ 8\ 21] \tag{2.1}$$

indicates that there are 5 filaments in this system, with their lengths appearing in the order indicated by the list (first the 4-monomer long filament, then to 10-monomer long one, and so on). Mapping this example to Figure 2.1, the 4-monomer long filament would be the closest to the top left, with the consecutive ones following it until the 21-monomer long filament is the closest to the bottom right.

Conversely, cross-linkers can be represented purely by the two filaments they cross-link. The representation of which filament is which is done through the ordering from the previously presented list of filaments. Therefore, the cross-linker list

$$\text{crosslinkers} = [(1, 3), (2, 4)] \tag{2.2}$$

would have a cross-linker between the 4-monomer long filament and the 1-monomer long one, and a cross-linker between the filaments of size 10 and 8.

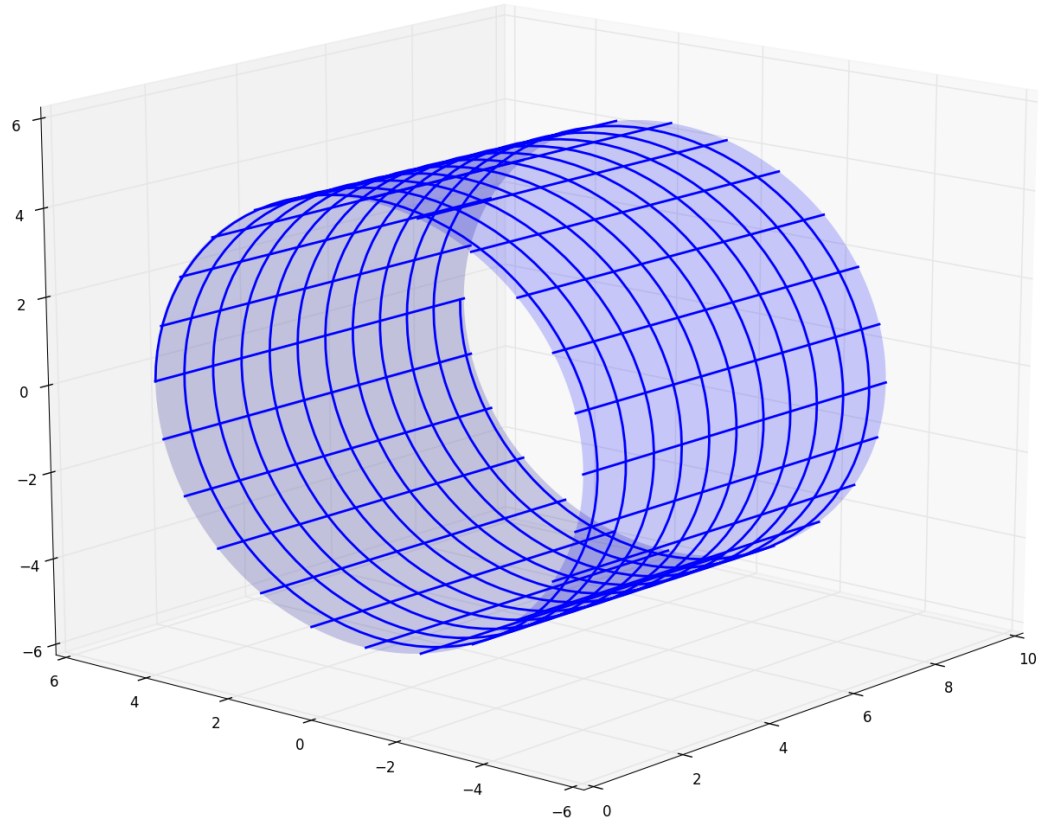

Figure 2.2: A three-dimensional representation of the system. This is equivalent to the "ribbon" representation of Fig. 2.1, wrapped in a third dimension so that the coloured boundaries at the ends are matched.

Having both representations defined, we can start to think of our system more like a normal two-dimensional lattice. The details of the essential one-dimensional nature of a long helix can be hidden inside the implementation, with the existence of a cross-linker between two filaments limiting their positions to a range of integers roughly within L from each other, so that they can maintain a lateral overlap between them.

2.2.3 Constraints Calculation

We are left, then, we the task of calculating the constraints on filament and cross-linker position given the presence of other structures in the system and the system boundaries. There are a number of interactions to consider here: steric (filament-filament) interactions, cross-linker dependent interactions and depletion interactions limiting cross-linkers to overlap regions.

For filament-filament interactions, it is quite simple to calculate constraints in their positions: the difference between positions in two consecutive filaments should be at least the size of the first one plus one (for a gap between them; two filaments without a gap would be a longer, single filament, defining a different system). We can add to that the fact that the first filament should obey a steric interaction with the initial hard barrier, and the last filament with the final hard barrier. Then, for K filaments, there are $K + 1$ total constraints which can be written; $K - 1$ for the differences between positions, and 2 for the two hard barriers. The $K - 1$ difference constraints will be, in general, of the form

$$x_{k+1} - x_k \geq l_k + 1 \tag{2.3}$$

if we choose the leftmost monomer of a filament for the point where the position x_k of the k-th filament is measured, and if l_k is the length of that filament. We can add the constraints

$$x_1 \geq 0 \tag{2.4}$$

and

$$x_K \leq (L * N) - l_K \tag{2.5}$$

where, again, L is the turn length of the helix and N is the number of turn lengths in the system, and K is the number of filaments in the system.

Cross-linkers introduce constraints on the positions of filaments. Multiple cross-linkers can appear between the same pair of filaments, and indeed that is a common occurrence in our simulations. Each set of one or more cross-linkers that connect two filaments introduce a constraint between the positions of the two filaments that are so linked.

Essentially, these constraints will be such that the minimum overlapping region between the filaments is equal to the number of repeated cross-linkers assigned to them. There is, therefore, a minimum and maximum value for the difference in their positions. These will of the form

$$x_j - x_i \geq L - l_j + r_{ij} \tag{2.6}$$

and

$$x_j - x_i \leq L + l_i - r_{ij} \tag{2.7}$$

where the two filaments in question are the i-th and j-th ones (with $i < j$), with their respective positions and lengths as previously noted, and r_{ij} is the number of repeated cross-linkers between these two filaments.

The trickiest constraints to write down are the ones regarding the positions of the cross-linkers in a given overlapping region. The size of an overlapping region depends on both positions x_i and x_j and both lengths l_i and l_j. For a given overlap region, we will call the individual cross-linker positions $s_1, \ldots, s_r$. These positions are specific to the overlap region, meaning that a cross-linker at the leftmost position in an overlap has a position $s_i = 0$. The relationship between these positions and global positions inside the system will depend on x_i, x_j, l_i and l_j in ways that are not trivial, and this relationship is not important to our model. The easiest constraints to write are

$$s_1 \geq 0 \tag{2.8}$$

$$s_{k+1} - s_k > 0 \tag{2.9}$$

and

$$s_r \leq \min l_i, l_j \tag{2.10}$$

Those only enforce that the first cross-linker cannot be outside the overlap

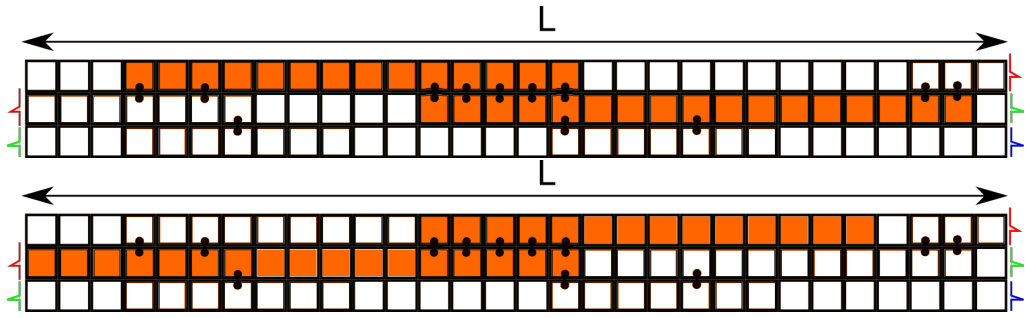

Figure 2.3: When the overlap region size is equal to the number of cross-linkers, we achieve equality on Equations (2.6) and (2.7). Here, we have $l_i = 14$, $l_j = 17$ and $r_{ij} = 5$, with $L = 30$. The difference $x_j - x_i$, then, have its minimum and maximum values of 18 and 39. Cross-linkers are represented as two circles ("heads") vertically connected. Only the two relevant filaments are represented for clarity, with the extra cross-linkers outside the overlap of interest being shown to indicate the presence of further filaments not being represented.

region to the left, that each subsequent linker in that overlap needs to increase in position and that the length of the overlap region can never be larger than the shorter of the two filaments involved.

The difficulty is, then, in writing the very last constraint, which is of the form

$$s_r < A \rightarrow s_r \leq A - 1 \tag{2.11}$$

where A is the size of the overlap region in terms of monomers. As previously mentioned, there is a trivial upper barrier on this value: the overlap region can never be larger than the smallest of the two filaments.

If we look at the constraints presented on Eqs. (2.6) and (2.7), we can start thinking about this problem. We want equality in these constraints when $A = r_{ij}$, that is, when the maximum position for a cross-linker is the number of cross-linkers minus 1 (due to counting from 0, not 1). We can visualise this situation in Fig. 2.3.

From those equality situations, we can write

$$x_j - x_i = L - l_j + (A + 1) \rightarrow A = x_j - x_i + l_j - L \tag{2.12}$$

and

$$x_j - x_i = L + l_i - (A' + 1) \rightarrow A' = x_i - x_j + l_i + L \tag{2.13}$$

The first limit was calculated for $x_j - L < x_i$, and the second for $x_j - L > x_i$. If we were to write constraints of the form presented in Eq. (2.11), we would have two constraints for the two different values of A.

Fortunately, enforcing both constraints at the same time is good enough. We can show that by inserting each of the limit conditions into the value of A calculated for the other limit. We rewrite the limits as

$$x_i - x_j > -L \tag{2.14}$$

and

$$x_j - x_i > L \tag{2.15}$$

Now, inserting Eq. (2.14) into (2.13) and rewriting it in the form of Eq. (2.11), we get

$$s_r \leq x_i - x_j + l_i - (x_i - x_j) - 1 \rightarrow s_r \leq l_i - 1 \tag{2.16}$$

and, conversely, inserting Eq. (2.15) into (2.12) and rewriting accordingly we get

$$s_r \leq x_j - x_i + l_j - x_j + x_i - 1 \rightarrow s_r \leq l_j - 1 \tag{2.17}$$

and we see that both of these constraints are already enforced by Eq. (2.10). In the situation of Fig. 2.3, the minimum $x_j - x_i = 18$ would give us $A = 18 + 17 - 30 = 5$ and $A' = -18 + 14 + 30 = 26$, and the maximum $x_j - x_i = 39$ would give us $A = 39 + 17 - 30 = 26$ and $A' = -39 + 14 + 30 = 5$.

Therefore, the constraint that does not enforce a strict limit on the size of the overlap region is, in fact, redundant. Since we can never be sure which of the two possibilities, A or A', is the enforcing limit and which is the redundant one, we shall apply both at all times.

2.3 Metropolis algorithm and statistical mechanics

In this section, we will describe the algorithms that will be used to simulate the dynamical behaviour of this system, and connect these ideas to our formulations.

Initially, we will outline how to establish simulations that can return results without needing to sample every possible configuration of the system. Therefore, we will see how Markov Chain Monte Carlo simulations are established and analyse their main properties. Then, we will introduce the Metropolis Algorithm and explain how this method ensures that we sample configurations at the right probability densities. Finally, we will connect these concepts to our model and show how they can come together.

2.3.1 Markov-chain Monte Carlo simulation

The aim of a Monte Carlo algorithm is to approximate averages by statistical sampling. The average of independent samples will obey the central limit theorem and tend to a normal distribution (as long as the variance of the underlying random distribution is finite), and the variance in the estimate will scale like $1/S$, where S is the number of samples.

Especially in problems where the dimensionality is high, involving many variables, using other methods that scale exponentially with the number of dimensions quickly becomes infeasible. Monte Carlo is very straightforward to implement and the scaling of the error only depends on the number of samples, and not on dimensionality.

We still have the problem of obtaining a "fair" sample. This problem can be posed, alternatively, as sampling from a probability distribution $p(x)$. Sometimes, these probability distributions will not analytical, closed forms. In these cases, it might not be possible to obtain independent samples.

Markov chains are processes that generate correlated sequences of states. A transition operator $T(x \to x')$ gives the probability of changing from state x to state x', from which every step in the sequence of states will be generated. What makes these chains of states Markovian is the property that the

probabilities associated with transitions depend only on the current state x.

This means that a Markov chain is memoryless, in the sense that anything happening before the current state does not have any bearing on what will happen next. In our case, we want the operator $T(x \to x')$ to leave the probability distribution $p(x)$ from which we want to sample stationary; that is,

$$p(x') = \sum_x T(x \to x')p(x) \tag{2.18}$$

for any x'. Although $p(x)$ is stationary, the state x can me time-dependent. Given this property, we would have the same marginal distribution at all subsequent steps of the chain. Furthermore, we might want the operator T to be such that the marginal distribution over a state will tend to $p(x)$ independently of the initial state. In this case, the operator needs to be able to reach any state $x|p(x) > 0$ in a finite number of steps (irreducibility) and that states that are only accessible at specific regularly spaced steps do not exist (aperiodicity) [Tierney, 1994].

It is possible to write a simpler version of this condition in the form of a detailed balance equation. In this case, we have

$$T(x \to x')p(x) = T(x' \to x)p(x') \tag{2.19}$$

for any x, x'. Essentially, it says that, given a state in equilibrium and the transition operator T, it should have the same probability of a forwards step $x \to x'$ and a backwards step $x' \to x$. By summing over x on both sides, we can recover the general condition. Detailed balance is a useful way of constructing transition operators that work for constructing Markov Chain Monte Carlo algorithms.

2.3.2 The Metropolis algorithm

The Metropolis algorithm is defined by its choice for the transition operator $T(x \to x')$. In this case, their choice is

$$\begin{aligned} T(x \to x') &= 1 \quad &, p(x) < p(x') \\ T(x \to x') &= p(x')/p(x) \quad &, p(x) \geq p(x') \end{aligned} \tag{2.20}$$

It is simple to prove that this transition operator satisfies detailed balance. If $p(x) < p(x')$, we have

$$T(x \to x')p(x) = p(x) \tag{2.21}$$

and

$$T(x' \to x)p(x') = (p(x)/p(x'))p(x') = p(x) \tag{2.22}$$

Alternatively, if $p(x) \geq p(x')$,

$$T(x \to x')p(x) = (p(x')/p(x))p(x) = p(x') \tag{2.23}$$

and

$$T(x' \to x)p(x') = p(x') \tag{2.24}$$

We can now relate this algorithm to Statistical Mechanics. In this case, we can define $p(x)$ as

$$p(x) = \frac{e^{-\beta E_x}}{\sum_y e^{-\beta E_y}} \tag{2.25}$$

where $\beta = 1/k_B T$ and E_x is the energy of a system [Binder et al., 1993].

The denominator in this term is, by definition, the partition function Z of a system; therefore,

$$p(x) = \frac{e^{-\beta E_x}}{Z} \tag{2.26}$$

and, thus,

$$\frac{p(x')}{p(x)} = e^{-\beta(E_{x'} - E_x)} \tag{2.27}$$

if the partition function Z does not change. In the general case where Z does change, we would have

$$\frac{p(x')}{p(x)} = \frac{\frac{e^{-\beta E_{x'}}}{Z(x')}}{\frac{e^{-\beta E_x}}{Z(x)}} = e^{-\beta(E_{x'} - E_x)} \frac{Z(x)}{Z(x')} \tag{2.28}$$

If we define the entropy of the system S as $ln(Z) = \frac{S - \beta\langle E \rangle}{k_B}$, we can now have

$$\frac{p(x')}{p(x)} = e^{-\beta(E_{x'} - E_x)} e^{-\beta T(-S_{x'} + S_x)} \tag{2.29}$$

and, thus,

$$\frac{p(x')}{p(x)} = e^{-\beta(\Delta E - T\Delta S)} \tag{2.30}$$

Finally, there is a simple relationship between the acceptance procedures of the Metropolis algorithm and relevant quantities in Statistical Mechanics, namely the free energy in the system and the partition function. By calculating those before and after a change of state, we can compute the ratio $p(x')/p(x)$ and, then, apply the Metropolis acceptance procedure accordingly.

2.3.3 Applying Metropolis to our model

It is clear, from the previous section, that we need to come up with procedures for calculating the variables ΔE and ΔS inside our model to deal with the acceptance procedure of Metropolis. A second detail was glossed over until now, but it is central to our simulation: the choice of which state x' should be attempted at each point.

We have chosen to take a temporal approach, introducing a global "clock" to the system and choosing how to change the state of it according to temporal rates. Different events (e.g. adding a filament, removing a monomer) can, then, occur at different rates over time, allowing us to attempt certain changes on consistent time scales that connects to the underlying biological system.

Therefore, we can think of the way our simulation runs in the following way:

- 1. Start a clock
- 2. Calculate the next occurrence of all possible events
- 3. Move to the next event in time
- 4. Attempt said event through a Metropolis approach; accept or reject it, go to step 2

and so on.

Calculating the variable ΔE for our systems is relatively straightforward. It will normally be composed of two parts: one for changes in chemical

potential due to binding or unbinding of agents in the system, and one due to the bending of filaments or membranes when a change of cell curvature is induced by forces that arise during simulation.

Unfortunately, calculating the entropy change ΔS is a much more difficult endeavour. For a given state configuration of the system, all microstates will have the same internal energy, so the problem of calculating the partition function Z (and, therefore, ΔS) can be reduced to that of calculating the number of microstates. That can be done analytically for a small subset of all possible systems, but in general it will be a very difficult problem. This problem is equivalent to calculating the number of integer solutions to all the linear constraints defined in Section 2.2.3. These constraints will define a high-dimensional convex polytope so we need an algorithm to count the integer points inside such an object, this being the number of accessible microstates.

2.4 Barvinok's algorithm

2.4.1 Background

The generic problem of counting the number of integer points that satisfy certain linear constraints has been around for a long time; importantly, compiler optimization techniques rely on such information to improve parallelism [Turjan et al., 2002], minimize memory size [Zhao and Malik, 2000; Turjan et al., 2002], estimate execution time [Lisper, 2003] and energy consumption [Kim et al., 2003], and other such tasks.

A technique to solve such problems has been proposed by Clauss and Loechner [Clauss and Loechner, 1996] and is implemented in the *Polylib* library [Loechner, 1999]. However, even for a fixed number of dimensions, this technique can be exponential for the worst case, and it might even fail to produce a solution altogether. Alternative approaches have been tried: automata-based counting techniques [Boigelot and Latour, 2004; Parker and Chatterjee, 2004], which are also exponential, and the algorithm presented by Pugh to solve the generic problem [Pugh, 1994]. However, Pugh's technique is also exponential, and no implementation has been completed.

The algorithm with which we are concerned in this work, through which

it is possible to compute the number of integer points in a fixed polytope in polynomial time, was first described by Barvinok in 1993 [Barvinok, 1994]. It would, then, be further extended by Barvinok and Pommersheim in 1999 [Barvinok and Pommersheim, 1999] to incorporate parametric polytopes (i.e., polytopes with a linear dependence on a parameter). Importantly, the first actual implementation of Barvinok's 1993 work came only in 2004, by De Loera *et al.* [De Loera et al., 2004].

In the next sections, we will present some useful definitions for the understanding of this algorithm, and then we will present how the counting procedure happens, and finally we will discuss the *barvinok* library, which is the specific implementation of that algorithm that is being used in this work.

2.4.2 Definitions

In this section, we will present some definitions that will prove useful when explaining the works of the counting algorithm. These will be mostly basic polyhedral definitions and theoretical results regarding polytope enumeration. Polytope enumeration is an essential result for counting accessible microstates and calculating the entropy of our systems.

A rational polyhedron $P \subset \mathbb{Q}^d$ is defined as the set of d-dimensional vectors $\mathbf{x}$ delimited by linear equalities

$$P = \{\mathbf{x} \in \mathbb{Q}^d | A\mathbf{x} \geq \mathbf{b}\} \tag{2.31}$$

where A is a matrix such that $A \in \mathbb{Z}^{m \times d}$ and $\mathbf{c}$ is a vector such that $\mathbf{c} \in \mathbb{Z}^m$. In our systems, these polyhedra will be defined by the constraints that emerge from filaments and cross-linkers.

The affine hull of a set $S \subset \mathbb{Q}^d$ is the set defined by $\{\lambda_1 x_1 + \ldots + \lambda_k x_k | \{x_1, \ldots, x_k\} \subset S, \lambda_i \in \mathbb{Q}, \sum_i \lambda_i = 1\}$. That is, the affine hull of a set is a set containing that "interpolates" between all points of the original set. Related to that, the dimension of a rational polyhedron $P \subset \mathbb{Q}^d$ is defined as that of its affine hull.

Furthermore, we will define a rational polytope as a bounded rational polyhedron; in the case of our system, any defined polyhedron representing the possible microstates can be contained inside a hypercube and is, therefore,

bounded. Thus, we will use polytope and polyhedron largely interchangeably when talking about applications of Barvinok's algorithm to our system.

Finally, we will define a face F of a rational polyhedron P as the intersection of P with $\{\mathbf{x} \in \mathbb{Q}^d | A'\mathbf{x} \geq \mathbf{c}'\}$, where $A'\mathbf{x} \geq \mathbf{c}'$ is a subsystem of $A\mathbf{x} \geq \mathbf{c}$. If the dimension of P is n, we call the $(n-1)$-dimensional faces as facets, and the 0-dimensional faces as vertices. Importantly, vertices are always extremal points of P, meaning that they cannot be written as convex combinations of other points in P.

We have dealt in rational numbers up to now; we can extend many of those definitions to real numbers and make some additional definitions. We will define the convex hull of a set $S \subset \mathbb{R}^d$ as the real-valued converse of the previously defined affine hull. That is,

$$\text{conv}S = \{\lambda_1 x_1 + \ldots + \lambda_k x_k | \{x_1, \ldots, x_k\} \subset S, \lambda_i \geq 0, \sum_i \lambda_i = 1\} \tag{2.32}$$

Another useful notion related to the convex hull is that of a conic hull of a set $S \subset \mathbb{R}^d$:

$$\text{co } S = \{\sum_i \lambda_i y_i : \lambda_i \geq 0, y_i \in S \ \forall \ i\} \tag{2.33}$$

Finally, we will define a rational cone $K \subset \mathbb{R}^d$ as the conic hull of a finite number of integer vectors, such as

$$K = \ \text{co}\{u_1, \ldots, u_k\} : u_i \in \mathbb{Z}^d, \ i = 1, \ldots, k \tag{2.34}$$

In this case, we call $u_1, \ldots, u_k$ the generators of the cone K. Also, we call this cone simple if the generators of that cone are linearly independent vectors. Importantly, $\mathbb{Z}^d$ is a lattice in $\mathbb{R}^d$, i.e., a discrete additive subgroup in Euclidean space.

Now, being $K \subset \mathbb{R}^d$ a simple rational cone, we take $c \in \mathbb{R}^d$ to be a vector such that the inner product $\langle c, \cdot \rangle$ decreases along the extreme rays of K (an extreme ray of an n-dimensional cone is simply the intersection of $n-1$ active constraints). Then, the series

$$\sum_{x \in K \cap \mathbb{Z}^d} \exp\{\langle c, x \rangle\} \tag{2.35}$$

converges. Furthermore, that series defines a meromorphic function in $c \in \mathbb{C}^d$. We will define this function as $\sigma(K, c)$. In fact, for all c, we can write this function as

$$\sigma(K, c) = p_k\left(\exp\{c_1\}, \ldots, \exp\{c_d\}\right) . \prod_{l=1}^{k} \frac{1}{1 - \exp\{\langle c, u_l \rangle\}} \tag{2.36}$$

here, p_k is a Laurent polynomial in d variables. From that formulation, we can see that the singular points of this meromorphic function are the ones where the denominator of each factor of the product are zero, that is,

$$H_j = \{c \in \mathbb{R}^d : \langle c, u_j \rangle = 0\}, j = 1, \ldots, k \tag{2.37}$$

which is a union of hyperplanes. Equations (2.35) and (2.36) are presented here without proof; these can be consulted in the references.

Now, being $P \subset \mathbb{R}^d$ a convex polytope, we will define the supporting cone of P at the vertex v as

$$K_v = \{u \in \mathbb{R}^d : v + \delta.u \in P\} \tag{2.38}$$

for all $\delta > 0$ sufficiently small. This is not an intuitive definition: a simpler definition is that K_v is generated by the vectors defined by the edges of P that intersect the vertex v. The decomposition of polyhedra into supporting cones will later be essential for an efficient counting algorithm.

We define a polytope as integral if the set of all of its vertices (hereby referred to as Vert$P$) lie on the lattice $\mathbb{Z}^d$.

In a work of 1988, Brion proposes the following: if P is an integral polytope, then

$$\sum_{x \in P \cap \mathbb{Z}^d} \exp\{< c, x >\} = \sum_{v \in \mathrm{Vert}P} \exp\{\langle c, v \rangle\}.\sigma(K_v, c) \tag{2.39}$$

This equality, however, does not hold at the singular points of the function $\sigma(K_v, c)$. [Brion, 1988] Importantly, this allows us to reduce the counting of integer points inside a polyhedron to calculating a function over the set of all vertices of that same polyhedron.

2.4.3 Enumerating non-parametric polytopes

We can, now, outline the algorithm for counting the integer points inside our polytopes. This procedure works for non-parametric polytopes, i.e., polytopes where A and c do not depend on any parameters. It uses proposition (2.39) to reduce the problem of enumerating the integer points to calculating a function over the set of vertices of a polytope.

The simplest way to count the integer points inside a polytope might appear to be to use $c = 0$ at equation (2.39). This does not quite work: for all functions $\sigma(K_v, c)$, the point $c = 0$ is singular, which invalidates the proposition. We are able to implement a similar approach, though. First, a parameter t is introduced. Now, c can be any generic point in $\mathbb{R}^d$, that is, a regular point for all functions $\sigma(K_v, c)$. Now, we will want to calculate the constant term of the Taylor expansion for

$$\sum_{x \in \mathbb{Z}^d \cap P} \exp\{t.\langle c, x\rangle\} \tag{2.40}$$

around $t = 0$. Proposition (2.39) allows us to do so by computing the constant terms $R(K_v, v, c)$ of the Laurent expansion of the functions

$$\exp\{t.\langle c, v\rangle\}.\sigma(K_v, t.c) \tag{2.41}$$

for Vert$P$. As long as we can obtain these terms $R(K_v, v, c)$ easily, we will be able to achieve our target of having an efficient algorithm for counting integer points inside a polyhedron, allowing us to easily compute the entropy in our systems.

In fact, it is possible to define a class of cones for which $R(K_v, v, c)$ is a straightforward computation. We will define a subset of simple rational cones as primitive; a primitive cone K is one where

$$K = \text{co}\{u_1, \ldots, u_k\} \tag{2.42}$$

where $u_1, \ldots, u_k$ is a basis of a lattice $\Lambda = \mathbb{Z}^d \cap \text{Lin}K$, where Lin$K$ is the linear hull of K. The vectors $u_1, \ldots, u_k$ are, then, called the primitive generators of K.

The term $R(K_v, v, c)$, it turns out, has an explicit formula for primitive cones K_v. The polynomial p_K is simply equal to 1 for primitive cones, making the function $\sigma(K, c)$ very simple to compute.

With that problem solved, we now need an efficient way of decomposing any simple rational cone K into a combination of primitive cones. When the dimension of our polytope d is fixed, this procedure can be done in polynomial time and the number of primitive cones is bounded. This decomposition is the central part of the algorithm; this is what makes a polynomial-time algorithm for counting integer points in a polytope possible.

We can, then, rewrite equation (2.36) in the cases where $K \subset \mathbb{R}^d$ is a primitive cone:

$$\sigma(K, c) = \prod_{l=1}^{k} \frac{1}{1 - \exp\{\langle c, u_l \rangle\}} \tag{2.43}$$

where $u_1, \ldots, u_k$ are the primitive generators of K. Again, we will present this without proof; it follows from Eq. (2.36), and the derivation can be found in [Barvinok, 1994].

From this result, it can be shown that,for any $k \in \mathbb{N}$, there exists a polynomial $Q_k(x_1, \ldots, x_k, y)$ of degree not more than k, with rational coefficients such that

$$R(K, v, c) = Q_k(x_1, \ldots, x_k, y).\prod_{l=1}^{k} x_l^{-1} \tag{2.44}$$

where $R(K, v, c)$ is the constant term of the Laurent expansion of the generic version of function (2.40) for any primitive cone K around $t = 0$ for any $v \in \mathbb{Z}^d$, any primitive k-dimensional cone $K \subset \mathbb{R}^d$ with its usual primitive generators and for any $c \in \mathbb{R}^d$ that is a regular point of $\sigma(K, c)$. For those points, we define $y = \langle c, v \rangle$ and $x_l = \langle c, u_l \rangle$ for $i = 1, \ldots, k$.

The derivation can be found at [Barvinok, 1994]. In fact, it can also be proven that calculating the terms $R(K, v, c)$ for primitive cones can be achieved by an algorithm that runs in polynomial time. Therefore, as long as cone decomposition into primitive cones can be done in polynomial time, the overall counting algorithm is polynomial time. This is essential for efficient computation of the number of accessible microstates, and for the calculation of entropies in our system.

Before detailing the procedure for cone decomposition, we need to define

the concept of index of a cone. This is essentially a natural number measuring how far a cone is from being primitive; Ind$K = 1$ is only true for primitive cones. It is, conversely, a measure of how complex the polynomial p_K is. Its precise definition is the number of integer points in Π, defined as

$$\Pi = \{x = \sum_{l=1}^{k} \alpha_l.u_l : 0 \leq \alpha_l < 1\} \tag{2.45}$$

As usual, $u_1, \ldots, u_k$ are the linearly independent generators of the cone K.

In his work in 1993, Barvinok's central finding was precisely that this cone decomposition can be achieved in polynomial time [Barvinok, 1994]. His proof is presented inductively: his first step is to show that, for fixed $d \in \mathbb{N}$, there is a polynomial-time algorithm that constructs at most 2^d simple rational cones $K_i \subset \mathbb{R}^d$ for any given cone $K \subset \mathbb{R}^d$. It also computes integral numbers $\epsilon_i \in -1, 1$. The relationship between the constructed cones K_i and the original cone K is such that

$$\text{Ind } K_i \leq (\text{Ind } K)^{(d-1)/d}, \ \forall i \tag{2.46}$$

$$K = \sum_{i \in I} \epsilon_i.K_i \text{ and } \sigma(K, c) = \sum_{i \in I} \epsilon_i.\sigma(K_i, c) \tag{2.47}$$

We can see that the index of the constructed cones are smaller than that of the original one. Barvinok shows that there is a finite number of steps from an original simple rational cone K to a family of cones K_i that are rational primitive cones. If we combine this with Equation (2.39) and a choice of c that is never a singular point for the function $\sigma(K_i, c)$ (that can also be calculated in polynomial time), we arrive at the expression

$$\#(P \cap \mathbb{Z}^d) = \sum_{v \in \text{Vert}P} \sum_{i \in I_i} \epsilon_i.R(K_i, v, c) \tag{2.48}$$

where the symbol # denotes the cardinality of a set, and we have completed the calculation of the number of integer points in our polyhedron P. This means that we can calculate the number of accessible microstates quickly from a set of constraints defined by filaments and cross-linkers, and therefore the computation of entropy in our system is efficient.

2.4.4 The *barvinok* library

In our work, we have extensively used the functionalities offered by the *barvinok* library, written in C [Verdoolaege]. This is a library specifically built for counting the number of integer points in parametric and non-parametric polytopes. This is not the first implementation of Barvinok's algorithm; LattE has been available since 2002 [Latte], implementing Barvinok's algorithm at least since 2006.

Even if it was not the first publicly available implementation of that algorithm, the ease of integration with regular C code was the most important point in choosing *barvinok* over LattE; the latter performs the computations we would need, but only through a standalone executable rather than function calls. It was, also, less open to modifications.

The *barvinok* library bas been built on top of PolyLib [Loechner, 1999], a library dealing with objects made up of unions of polyhedra in any dimension; however, due to the extensive rewriting and improvement of algorithms implemented in PolyLib, the dependence on that library is currently being phased out.

Instead, many of the functionalities necessary to *barvinok* are now implemented as a separate library: the Integer Set Library (ISL) [Verdoolaege, 2010]. This is a library for manipulating sets and relations of integer points delimited by linear constraints. Of course, linear constraints also define polyhedra; however, by concerning itself only with integer points, ISL is able to be a more focused library than PolyLib, and more apt for our work, for example. ISL routines are also exposed enough that we are able to use them directly without using the *barvinok* wrappers, which makes using custom data structures easier.

Given the current in-between status of the library, versions of *barvinok* at the moment include both ISL and PolyLib. In addition to that, the library uses the Number Theory Library (NTL) [Shoup et al., 2009] and it can be compiled with support to the GNU Scientific Library (GSL) [Gough, 2009] and the GNU Multiple Precision Arithmetic Library (GMP) [Granlund]. The latter one is of special interest to us; very high-dimensional polyhedra will have very large numbers of integer points, meaning that even very long integer representations in standard C would not be enough. GMP allows for integers

with arbitrary precision, bypassing that problem.

2.5 Uniform sampling in high-dimensional convex polytopes

There are many reasons to sample from a convex polytope P in a high-dimensional space $\mathbb{R}^n$. Our model also requires this: in our case, this is the equivalent of sampling a microstate at random. This sampling will be necessary when we need to examine microstate-specific quantities, which is necessary for values where computing the global ensemble average is not feasible (for example, the number of lateral overlap sites available for cross-linker binding).

To achieve this task, multiple algorithms are available [Smith, 1984]. Some approaches might rely on transformational or rejection techniques. Transformation approaches work through generating a point X uniformly distributed inside a hypercube in n dimensions and, then, mapping X through a smooth function T onto the desired region P. However, T is known and relatively simple only for a limited class of P, and does not generalize to all polytopes.

Rejection techniques sample in an even simpler way: it generates a uniformly distributed point inside a region D that encloses our region of interest P and, then, accepts it if it lies inside P and rejects it otherwise. Common choices for D are paralleletopes, hyperspheres and simplexes, and the points might be generated using transformation techniques if necessary. However, the number of generated points before an acceptance grows very quickly with the dimension n and might become computationally infeasible [Smith, 1984].

The efficient solutions for this problem are all based on random walks [Dyer et al., 1988; Lovász, 1991; Kannan et al., 1997]. Amongst these, the hit-and-run random walk shows up as the best of the bunch: it has the same worst-case complexity as its ball walk counterpart, but is commonly faster in practice [Lovász and Vempala, 2003].

2.5.1 The hit-and-run algorithm

Thus, we will use the hit-and-run algorithm as our main method for sampling random microstates in our systems, whenever this is necessary. We will still define a polyhedron from the constraints that emerge from the existing filaments and cross-linkers, and then use this search algorithm for finding a random point inside it uniformly.

The basic principle behind the hit-and-run algorithm is remarkably simple: starting from a point x inside the region of interest P, a point θ on the surface of a n-dimensional unit hypersphere centered around x is picked at random. That defines a line passing through x and θ; a point is, then, sampled from the intersection of that line with the region P, and the process is restarted with this point as x [Kiatsupaibul et al., 2011].

An alternative solution is to pick the random direction of motion for each time step not in the surface of a unit sphere, but as a unit vector in one of the coordinate directions. The complexity involved in calculating the line section inside the polytope is reduced significantly, but our mixing time results will not apply any more [Berbee et al., 1987]. Regardless, we have chosen to use the coordinate directions instead of the hypersphere directions.

This process defines a Markov chain that can be shown to be strongly mixing, that is, that it will converge to a uniform distribution over the whole region P for a sufficient large number of time steps. It is also true that serial correlations between any two points X_k and X_{k+M} goes to zero as the number of time steps M separating them becomes large [Smith, 1984].

Our issue, then, is to estimate how many iterations are necessary for enough mixing to occur and good enough uniformity to be established, i.e., the mixing time of this algorithm. It is important to note that the exact mixing time depends heavily on the initial point x chosen for the algorithm; we will return to this point later [Lovász and Vempala, 2006]. For now, we will present some general case results.

In the very first paper presenting the hit-and-run algorithm, Robert L. Smith shows that, for any measurable set $A \subseteq P$, [Smith, 1984]

$$|P(X_m \in A | X_0 = x) - \lambda(A)| < \left(1 - \left(\frac{\gamma}{n2^{(n-1)}}\right)\right)^{m-1} \tag{2.49}$$

In this equation, γ is the ratio of the n-dimensional content of P to the n-dimensional content of the smallest sphere that can contain P, and λ is a stationary initial distribution. Therefore, it shows that the difference between the sampled distribution and a uniform one is bounded by an exponentially-decreasing term on the number of time steps m.

Lovász goes further and tries to approximate the actual number of time steps necessary for mixing. He shows, that, indeed, mixing occurs in $O(n^2R^2)$ steps, where n is the dimensionality and R is the radius of the ball containing P. They further argue that, through pre-processing, it is possible to achieve $R = O(n)$, reducing the order of the mixing time to $O(n^3)$ [Lovász, 1999].

Now, as previously mentioned, these are upper bounds; it is possible to establish more specific results given an initial distribution for the starting point. Indeed, Lovász and Vempala arrive at exactly this result [Lovász and Vempala, 2006]. Being P a convex polytope containing a ball of radius r and contained in a ball of radius R, and being the starting distribution concentrated at a single point at a distance d from the boundary, and σ_m the distribution of the current point after m time steps, for

$$m_{min} \propto \frac{n^3R^2}{r^2} \ln \frac{R}{d\epsilon} \tag{2.50}$$

the total variation distance of σ_m and a uniform distribution is at most ϵ [Lovász and Vempala, 2006]. As we can see, ideally we would like to maximise d so that mixing can happen as fast as possible. We will return to this problem later.

Calculating movement ranges

When trying to pick a point at random in a polyhedron, which is our aim for this section so that we can sample uniformly from all possible microstates in our system, we iteratively pick a random direction to move and a distance to move in that direction.

At every time step, after picking a random direction for movement, the hit-and-run algorithm requires us to pick a random point in the line set that is the intersection of the line defined by the direction and the current point and the polytope. This step has been suggested to be the most computationally

intensive for this algorithm [Berbee et al., 1987].

The procedure for calculating our movement ranges, however, is the same regardless of the direction picked. Here, it makes more sense to think of each individual inequality from our $A\mathbf{x} \geq \mathbf{b}$ polytope representing the constraints from filaments and cross-linkers separately; therefore, we will posit our polytope as

$$A_i\mathbf{x} \geq b_i \ , \ (i = 1, \ldots, m) \tag{2.51}$$

where m is the number of inequalities defining the constraints.

Given that the current point in the hit-and-run random walk is X_k, we obtain a vector v that will define a movement direction, trying to explore the polytope. Afterwards, we need to determine

$$\lambda_i = \frac{b_i - A_i X_k}{A_i v} \ , \ (i = 1, \ldots, m) \tag{2.52}$$

There are, now, m values for the λ_i constants. The maximum distance that can be travelled in the chosen direction is, then,

$$\lambda^+ = \min_{1 \leq i \leq m} \{\lambda_i | \lambda_i > 0\} \tag{2.53}$$

and the maximum distance that can be travelled in the opposite to the chosen direction is

$$\lambda^- = \max_{1 \leq i \leq m} \{\lambda_i | \lambda_i < 0\} \tag{2.54}$$

Therefore, we can calculate the next point in the random walk as

$$X_{k+1} = X_k + \left(\lambda^- + u(\lambda^+ - \lambda^-)\right) v \tag{2.55}$$

where u is a real number chosen from a uniform distribution on $[0, 1]$ [Berbee et al., 1987]. This procedure, when done iteratively, will allow us to explore the polytope and sample from it uniformly after the Markov chain defined by consecutive points in the hit-and-run algorithm mixes. This will allow us to sample a microstate at random from all accessible microstates.

Calculating the Chebyshev centre

When trying to sample a microstate at random for our simulations, it is important to start from a point far from the boundaries of the polytope defined by the constraints written from the filaments and cross-linkers. This will allow us to minimize the mixing time of the hit-and-run algorithm. There is a second problem: the algorithm presumes any given point is internal to the polyhedron for the calculation of the next point in the random walk, while we have never established any procedure to obtain such a point.

Both problems can be solved if we can calculate the Chebyshev centre of a polytope. This is the point that is the centre of the largest inscribed ball of a polyhedron P. By definition, this is the point that has the largest minimum distance to one of the limiting hyperplanes of P. Given our estimate for the mixing time m in Eq. (2.50), this is the point with maximum d, which minimizes the mixing time necessary to obtain a uniform distribution.

The easiest formulation of this problem is that of a linear program: essentially, what we want is to maximize a radius r. That is, if we represent the inscribed ball as

$$\mathcal{B} = \{x_c + u| \ ||u|| \leq r\} \tag{2.56}$$

then our variables in the problem are the centre x_c and the radius r. Our constraints for maximisation of r are that $\mathcal{B} \subseteq P$.

That means that every point of $\mathcal{B}$ needs to obey every single constraint of P. We can write such a condition for a single constraint as

$$a_i(x_c + u) \leq b_i \tag{2.57}$$

following the notation first introduced in Eq. (2.51). We will be able to rewrite this inequality as

$$a_i x_c + r||a_i|| \leq b_i \tag{2.58}$$

by using the identity

$$\sup\{a_i u| \ ||u|| \leq r\} = r||a_i|| \tag{2.59}$$

Now, this is a linear inequality in x_c and r. The same process can be done for

every single inequality that defines P, therefore we can rewrite the condition that $\mathcal{B} \subseteq P$ as the ensemble of all inequalities of this form. Finally, that means that the problem of finding the Chebyshev centre can be written as a linear program of the form

$$\begin{aligned} &\text{maximise} && r \\ &\text{subject to} && a_i x_c + r||a_i|| \leq b_i, \quad i = 1, \ldots, m \end{aligned} \tag{2.60}$$

on the radius r and the point x_c.

Finally, we have defined the procedures and algorithms that will be used to simulate our bacterial division model. We have introduced a formulation for this problem and a way of representing different structures in a computational model. The existence of these structures and their interactions will define a set of inequalities that delimit the microstates that are accessible at any given time.

Then, we have established the algorithms that will be used for evolving these systems in time. These algorithms demand very computationally intensive calculations, especially when computing the entropy for these systems, requiring us to discuss an efficient, polynomial-time algorithm for counting integer points inside polyhedra, which can be mapped to the number of accessible microstates. Finally, we have discussed a procedure for sampling microstates at random, which will be necessary when trying to access quantities that can not be feasibly calculated for whole ensembles of microstates.

Chapter 3

Single-filament dynamics

3.1 Introduction

There are multiple examples in our everyday lives where confining molecules spatially can generate directed forces, such as the motion that a compressed gas piston exerts when force is not applied to it. It is rare, however, to see the same concept being used to explain subcellular processes, relying on statistical mechanics; it sounds reasonable that confining molecules that can diffuse around would give rise to the same kind of directed forces and, in fact, experimental evidence confirms that this is the case. In the following chapters, we investigate these directed forces in the context of bacterial division, as an alternative to the common explanations for the generation of contractile forces without molecular motors.

Lansky et al.[Lansky et al., 2015] introduce this idea in the very specific context of microtubule sliding. The diffusion of proteins along microtubules was already established [Helenius et al., 2006]; moreover, it had been previously shown that microtubule ends were effective diffusion barriers for microtubule cross-linkers [Braun et al., 2011]. Thus, diffusible molecules confined in space can generate directed entropic forces.

Finally, because microtubule-microtubule sliding was slowed in the presence of the protein Ase1 [Braun et al., 2011; Janson et al., 2007] and because that protein was shown to be capable of diffusing in microtubule overlaps [Braun et al., 2011; Kapitein et al., 2005], it was deduced that Ase1 was, in fact, a diffusible cross-linking. This allowed an experimental setup test of the

entropic force hypothesis in microtubule-microtubule sliding.

It was further shown that a small number of Ase1 molecules could be confined between two microtubules with a partial overlap. By keeping one of the microtubules fixed and moving the other one (in this case, by applying flow), the Ase1 molecules were confined to a smaller, effectively one-dimensional overlap area; when flow was removed, the free microtubule, as expected, slid directionally so that overlap was maximized again [Lansky et al., 2015].

In this simple system, it was possible to approximate the overlap expanding force and velocity analytically, by using a one-dimensional equivalent of the ideal gas law. That was the case since the number of cross-linkers in the overlap region is constant during the experiment; therefore, the force depends only on the entropy of the cross-linkers there, and the partition function for the system can be analytically calculated from the number of possible microstates that the system can access.[Lansky et al., 2015] In that case, the force expression can be derived as

$$F = \frac{k_B T}{\delta} \ln\left(\frac{l+1}{l+1-n}\right) \tag{3.1}$$

where δ is the length of each binding site, l is the number of binding sites in the overlap region and n is the number of cross-linkers there [Lansky et al., 2015]. This expression comes from the combinatoric nature of the number of ways of placing n cross-linkers in l binding sites, like a one-dimensional ideal gas law.

In this work, we extend this analytical approximation by developing a computational model that calculates entropy in a similar fashion (i.e. by explicitly counting the number of possible microstates a given configuration of a system can access in a combinatoric fashion). This approach is complemented by a model of binding and unbinding dynamics for cross-linkers and depolymerisation for filaments, allowing a computational Metropolis-Monte Carlo algorithm to be developed [Hastings, 1970]. Also, we concentrate on helical filaments; instead of two filaments, these systems require only one. A single helical filament also defines a ring-like region of space, a markedly different geometry from the Lansky work.

We show that the same expanding force in the overlapping region that was shown experimentally [Lansky et al., 2015] could, in this different geometry, be harnessed to generate contractility in helical filaments. Moreover, we show that the contractile force that can be generated is in the piconewton (pN) range, in good agreement with experimental data [Lansky et al., 2015].

Furthermore, this is the minimal system where we can test the helical geometry and the very first system where we can use the directed forces generated by diffusible cross-linkers to generate contractility in a way that might be relevant for bacterial cytokinesis, which is our model system.

We also show that, in this geometry, sustained contractility can be achieved by depolymerisation of the helical filament, and that the cross-linkers need to be strongly bound to the filament for contraction to be achieved. Finally, we show that there is a delicate balance between depolymerisation kinetics and the dynamics of cross-linking binding and unbinding when it comes to achieving significant constriction.

By coupling the existing model for directed forces in the presence of diffusible cross-linkers with filament and cross-linker dynamic kinetics, we can study contractility in an environment more closely related to what is actually going on *in vivo* and study the influence of dynamic processes of binding and unbinding on the forces being generated. We use the bacterial protein FtsZ as our closest biological reference and model system; bundling agents exist for this protein [Small et al., 2007], it is a tubulin analogue [Erickson, 1995] and it polymerises into a ring-like region in the center of dividing bacterial cells [Ma et al., 1996; Haeusser and Margolin, 2016], making this the more closely related biological case for the helical geometry.

3.2 Theoretical Background

In this section, we will start by going through the statistical mechanics for this system. Then, we will compare the performance of our computational model to the analytic predictions at the dilute limit, where the one-dimensional ideal gas law should be a good approximation.

Then, we will briefly discuss the nature of our computational implementation of such concepts, and re-analyse how the kinetics and dynamics of

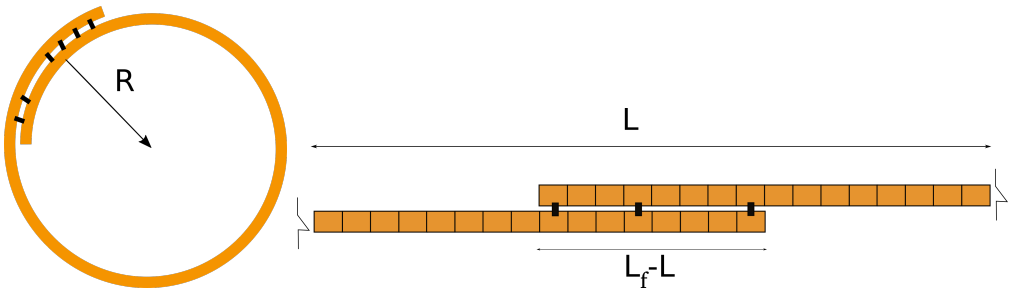

Figure 3.1: System with a single helical filament. We define $L = L_f - n * \delta$ where n is the number of monomers in the overlap area and δ is the size of a monomer, and approximate the radius of curvature R as $R = L/2\pi$; since R should be significantly bigger than the monomer size, that should be a decent approximation for the average radius of curvature of the filament. On the right, we see a lattice representation of the system, with the helix sectioned and opened up.

binding and unbinding are implemented in our code. Finally, we will discuss the Metropolis algorithm that simulates the temporal evolution of our system.

3.2.1 Analytic Expressions

In this chapter, we will mostly be concerned with a system of a single helical filament coiled around itself, as presented on Figure 3.1. This allows us to access lateral overlaps without a second filament, and it should yield contractility.

We start by considering the case of the single helical filament having length L_f with turn length L. The region where there is a lateral overlap of that filament with itself is, then, $L_f - L$. We will indicate the number of possible binding sites for cross-linkers as

$$l = \frac{L_f - L}{\delta} \tag{3.2}$$

where δ is the length of each binding site. In this way, we are able to render this quantity nondimensional.

We will assume that cross-linkers do not bind a side at a time, but rather at both sides at the same time. It makes the binding process one-step as opposed to two-step, and simplifies both the analytical expressions as the computational algorithm. This assumption has been shown to be valid for

Ase1 [Lansky et al., 2015], and we will assume it to be the case in our model system as well.

Furthermore, we will assume that this cross-linker binding process is non-cooperative; again, this is an assumption that is valid for Ase1, and we will consider it to be the case for our model. With that assumption, we are able to consider each binding or unbinding event as independent from all the others.

We are interested, initially, in writing down the expression for the overlap expansion force in this system. In one dimension, we can write the one-dimensional equivalent of pressure associated with this system as

$$P = \frac{\partial E}{\partial L} \tag{3.3}$$

which we approximate by

$$P = \frac{\Delta E}{\Delta L} = \frac{\Delta E}{\delta} \tag{3.4}$$

Therefore, for constant internal energy in the system, the force driving an increase in overlap length (which is, in this case, the contractile force) can be written as

$$F = \frac{\Delta S}{\delta} \tag{3.5}$$

this depends only on the change in entropy associated with the change in overlap length. Finally, we can write the force expression as

$$F = \frac{k_B T}{\delta} \ln \left[\frac{Z(l+1, n)}{Z(l, n)} \right] \tag{3.6}$$

where $Z(l, n)$ is the partition function for n cross-linkers in an overlap with l binding sites; for a system where n is constant, that is simply the number of ways the n cross-linkers can be organized in the l binding sites and be written as a combinatorial expression; that is,

$$Z(l, n) = \binom{l}{n} = \frac{l!}{(l-n)!n!} \tag{3.7}$$

This, however, does not take into account the translational freedom of the

filament over the helical region of interest; increasing the curvature $2\pi/L$ decreases the size of the region of interest and, therefore, translational freedom of the filament. This will be proportional to the circumference size L and we will see that the proportionality constant will not matter; therefore, we will take the partition function to be

$$Z(L, l, n) = L\binom{l}{n} = L\frac{l!}{(l-n)!n!} \tag{3.8}$$

Thus, we can rewrite our force to depend only on l, the number of binding sites in the overlapping region before expansion, n, the number of cross-linkers in this region, and L, the circumference size that defines the filament curvature, by simplifying the factorial expressions in Z and arriving at

$$F(l, n) = \frac{k_B T}{\delta} \ln\left[\frac{(L-1)}{L}\frac{(l+1)}{(l+1-n)}\right] \tag{3.9}$$

where an increased overlap region comes at the expense of decreasing the circumference from L to $L-1$ and, since $(L-1)(l+1) \geq L(l+1-n)$ for almost all cases (the exception is a single cross-linker and $l = L$), the existence of even a single cross-linker in the overlapping region is already enough to generate a positive constrictive force.

We consider the case where L is large, so $L \approx L - 1$. As previously stated, that force depends only on the number of monomers in the overlap and the number of cross-linkers in the overlap:

$$F = \frac{k_B T}{\delta} \ln\left[\frac{l+1}{l+1-n}\right] \tag{3.10}$$

It is clear that the maximum force that can be generated is, therefore, the case there $l = n$, where we have

$$F_{max} = \frac{k_B T}{\delta} \ln\left[n+1\right] \tag{3.11}$$

By using the appropriate value of $k_B T$ in $pN.nm$ and the value of $\delta = 5nm$ for the size of an FtsZ monomer, we could, therefore, calculate the hypothetical contractile force in piconewtons generated by a number of cross-linkers in a lateral overlap of a FtsZ filament, our model system.

$$F_{max} = \frac{4.114}{5} \ln [n+1]\, pN \tag{3.12}$$

The maximum force of a system with constant number of cross-linkers, therefore, scales with $\ln(n)$, leaving the scale of the force predominantly dominated by the prefactor.

The next point of interest is the force-velocity relationship in this system; Lansky et al. [Lansky et al., 2015] show that, for a constant number of cross-linkers, this is a linear relationship of the form

$$v = \frac{F}{\gamma_{MT}} \tag{3.13}$$

where γ_{MT} is an effective friction coefficient of the form

$$\gamma_{MT} = \frac{n\gamma}{2} \tag{3.14}$$

where the factor of 2 accounts for the fact that γ is the drag coefficient between a single head of the cross-linker and a filament. We assume cross-linkers to exclude each other, effectively implementing a sliding behaviour by taking cross-linkers to have an ordering associated with them. Finally, we can obtain the coefficient γ by Einstein's relation $k_B T/D$, where D is the diffusion coefficient of a single cross-linker over a single filament. Thus, we can write our velocity expression as

$$v(l,n) = \frac{2F}{n\gamma} \tag{3.15}$$

and we can, then, replace F by the previously calculated expression in Eq. (3.9) and γ by Einstein's relation, yielding

$$v(l,n) = \frac{k_B T}{\delta} \frac{D}{n k_B T} \ln \left[\frac{(L-1)}{L} \frac{(l+1)}{(l+1-n)} \right] \tag{3.16}$$

and, finally, that can be simplified to

$$v(l,n) = \frac{2D}{n\delta} \ln \left[\frac{(L-1)}{L} \frac{(l+1)}{(l+1-n)} \right] \tag{3.17}$$

which depends on the diffusion coefficient of a single linker over a single filament rather than on the more complicated factor γ_{MT}.

Now, we want to calibrate the results from our model, using the calculation of forces and velocities as specified above, versus a one-dimensional equivalent of the ideal gas law. To do that, we will compare the equilibrium point of the system from our simulations to what would be achieved through the ideal gas law.

Therefore, we need to be able to calculate what the equilibrium radius (equivalent to cell size) of a contracting helical filament would be, given its bending rigidity, initial size, intrinsic curvature and the number of cross-linkers in the system, based on the ideal gas law.

We will define the length $L = 2\pi R$, where R is the radius of curvature of the filament. We define the bending energy H following the Canham-Helfrich Hamiltonian [Helfrich, 1973] as

$$H = \frac{1}{2}\int_S \kappa \left(\frac{1}{R} - c_0\right)^2 ds \tag{3.18}$$

where κ is the bending rigidity of the filament, which means that

$$H = \frac{\pi}{2} L_f \kappa \left(\frac{2\pi}{L} - \frac{1}{L_0}\right)^2 \tag{3.19}$$

where we are approximating R as a constant around the whole filament for simplicity. Here, L_f is the length of the filament and $L_0 = 1/c_0$ is the inverse of the preferred curvature of the filament.

From the one-dimensional lattice gas law, we have that the force generated by the cross-linkers is

$$F_s = k_B T \frac{N}{L_f - L} \tag{3.20}$$

where n is the number of cross-linkers and $L_f - L$ is the length of the overlap region.

At equilibrium length, we have that the contractile entropic force from the cross-linkers should balance the force generated by the filament bending. Therefore, we have

$$F_s = -\frac{\partial H}{\partial L} \tag{3.21}$$

This mechanical equilibrium condition is a third-order polynomial in L, that can be analytically solved for the equilibrium length by taking the real (or positive) root. We will present our findings in the Results section.

3.2.2 Our computational Model

In this section, we discuss how the simulation of this system over time is performed in different cases, based on different experimental scenarios.

We have built a total of three separate set-ups for our computational model: in the first one, we assume that there is no binding or unbinding of cross-linkers at the overlap region; this is inspired by an experimental set up in which, after binding, the remaining free cross-linkers would be washed away with buffer and the bound cross-linkers are very strongly bound. In the second one, we allow only for unbinding; this is a similar set up to the first one, but where the binding between cross-linkers and filament is weak enough that it can be broken, causing unbinding to occur. For the third one, we allow for both binding and unbinding, mimicking a set up where the remaining free cross-linkers are not washed away.

Importantly, we set our time step small enough to allow us to use the expressions from the previous section. As long as the typical binding or unbinding time is long enough compared to the simulation time step, we can consider the system as having a constant number of cross-linkers at each individual time step. Simultaneously, such time step should be long compared to the diffusive timescale associated with the cross-linkers.

Furthermore, in all of those set ups our helical filament is allowed to depolymerise and change curvature, except where explicitly mentioned otherwise. That means that the overlap region length can be changed by these two processes: the contractile force will want to increase the overlap length, which comes at the expense of increasing curvature, while depolymerisation will want to decrease the overlap length by releasing energy stored in monomer-monomer binding. The resulting force over the filament depends on the size of the overlap, the number of cross-linkers and the curvature of the filament, and it can be either contractile or expansive.

We can think of Eq. (3.6) as the force being an energy divided by a

distance. In fact, we can think of it as the difference between the free energy of the system between two states, divided by the distance over which a force would be applied to do work equal to that difference in energies. Therefore, we can define a difference in energy $\Delta\Omega$

$$\Delta\Omega = k_B T \ln\left[\frac{Z(L-1, l+1, n)}{Z(L, l, n)}\right] = k_B T \left(\ln\left[Z(L-1, l+1, n)\right] - \ln\left[Z(L, l, n)\right]\right) \tag{3.22}$$

Note that, here, we use the convention of $\Delta\Omega$ positive for contractile forces. If we are to think in terms of free energy, we need a negative difference for a positive force. Therefore, we will define a free energy Ω as

$$\Omega(L, l, n) = -k_B T \ln\left[Z(L, l, n)\right] \tag{3.23}$$

This, however, only takes into consideration the process related to the contractile force, since it is based on the entropy of cross-linkers in the overlapping region. It is necessary, thus, to incorporate filament curvature into this picture to have a valid Hamiltonian for the system.

For that, we will use a simple term for bending of the filament, given its bending rigidity κ and its preferred curvature c_0:

$$U(c) = \frac{\kappa}{2}(c - c_0)^2 \tag{3.24}$$

where c is the curvature at a given point in the simulation; that is, $c = 2\pi/L$ given that L is the turn length of the helical filament. Again, we are approximating the radius of curvature R to be constant over the filament.

We can rewrite U to depend in L, and also rewrite Ω to depend on L_f, L and n given a size of monomer δ:

$$U(L) = \frac{\kappa}{2}\left(\frac{2\pi}{L} - c_0\right)^2 \tag{3.25}$$

$$\Omega(L, L_f, n) = -k_B T \ln\left[Z(L, \frac{L_f - L}{\delta}, n)\right] \tag{3.26}$$

and, finally, we can put them all together for a single free-energy expression of the form

$$H(L, L_f, n) = \frac{\kappa}{2}\left(\frac{2\pi}{L} - c_0\right)^2 - k_B T \ln\left[Z(\frac{L_f - L}{\delta}, n)\right] \tag{3.27}$$

When a contractile event happens ($L \to L - 1$), both parts of the equation change with opposite signs if we consider c_0 to be low; since $2\pi/L$ drifts further from c_0, the first part increases, while the increased overlap length means the second part increases in magnitude, but its negative sign means it actually decreases.

These two factors will oppose each other at most times in our simulation, and, of course, the equilibrium turn length L to which the system will contract, given a certain L_f and n, will be defined by

$$\frac{\partial H}{\partial L} = 0 \tag{3.28}$$

The logarithmic part of the expression means there is no analytical solution for this transcendental equation, which means the only way to study this deceptively simple system, even in the case where filament length and quantity of cross-linkers is fixed, is through computational work.

3.2.3 Overlap expansion velocity at the dilute limit

In this section, we will show that, in the dilute limit, overlap expansion velocities (i.e. contractility) should not depend on the number of cross-linkers in the overlap region, but only on the size of that region and the diffusion constant for the cross-linkers, which is the case for the one-dimensional lattice gas; we seek to show that the way we calculate expansion velocities from the simulations agrees with the theoretical prediction at low densities.

We start from equation Eq. (3.15), that tells us what the force-velocity relationship is. However, instead of using Eq. (3.9) for the force in this system, we will approximate it by the ideal gas law; this approximation should be good for low density of cross-linkers in the overlap region.

Therefore, we will have

$$F = \frac{k_B T}{\delta}\frac{n}{l} \tag{3.29}$$

where we follow the notation conventions of Eq. (3.9). Replacing it in the velocity expression, we get

$$\nu(l,n) = \frac{2k_BT}{\delta}\frac{n}{l}\frac{1}{n\gamma} \tag{3.30}$$

Finally, we can apply Einstein's relation for the friction coefficient γ, obtaining

$$\nu(l,n) = \frac{2k_BT}{\delta}\frac{n}{l}\frac{D}{nk_BT} \tag{3.31}$$

which, after simplifying, yields

$$\nu(l,n) = \frac{2D}{L} \tag{3.32}$$

where $L = \delta l$ is the total length of the overlap region. Importantly, the number of cross-linkers n cancels out and is not part of this equation.

We can see the comparison between overlap expansion velocities from the ideal gas law and the simulations in Figure 3.2.3 as a sanity check. The numerical values were obtained using the diffusion coefficient of Ase1 molecules over microtubules due to the lack of data for FtsZ. We obtain the expansion velocity computationally for different number of cross-linkers and by the Eq. (3.32). The plotted points are only those where the density of cross-linkers $n/l < 0.5$, and their difference to the ideal gas law converge to zero when the density of cross-linkers becomes small.

3.2.4 Kinetics and dynamics

In anything but the most basic of cases (fixed filament length and number of cross-linkers), we need to define the kinetics on which processes will occur. Essentially, there are three processes that involve binding/unbinding of proteins: depolymerisation of the filament, binding and unbinding of cross-linkers. In this chapter, no additional polymers will be added after the initial set up.

We should note that we have chosen not to address polymerisation in this system. Allowing for filaments to grow concurrently with shrinkage would mean increasing the overlap region without necessary contraction, meaning that growing filaments would not achieve constriction by definition and are of no interest to this work.

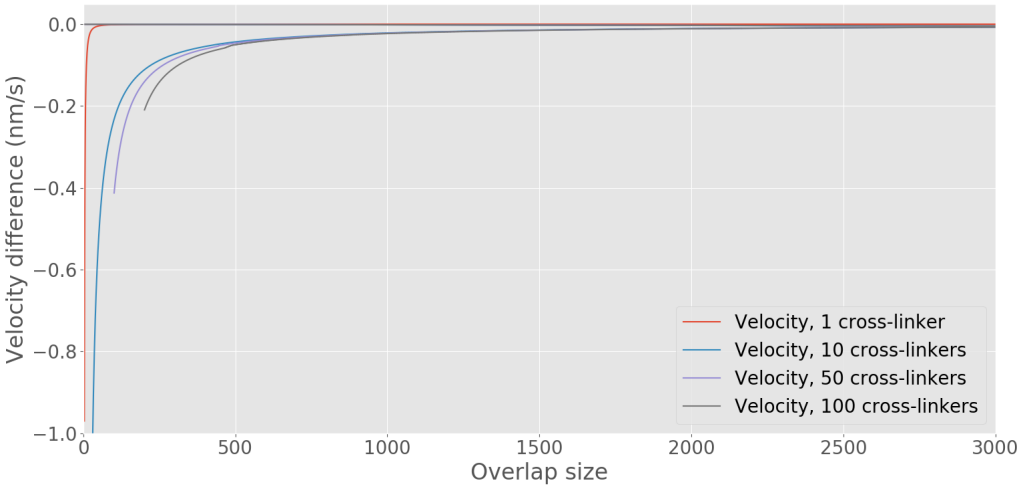

Figure 3.2: The prediction that overlap expansion velocity does not depend on the number of cross-linkers for low density of cross-linkers is also confirmed, with their difference to the ideal gas law converging to zero. We plot all data points with densities lower than 0.5.

Similarly, systems with polymerisation rates lower than depolymerisation rates would be effectively shrinking with an effective depolymerisation rate and are, therefore, very similar to our system without polymerisation.

The common thread between the three kinds of kinetics existing in this system is the fact that they are considered to be Poisson processes; that means that they are memoryless, and that the distance between two consecutive events in time is an exponential random variable with probability density function

$$f(t,k) = \begin{cases} ke^{-kt}, & t \geq 0 \\ 0, & t < 0 \end{cases} \tag{3.33}$$

where k is the reaction rate for the process at hand.

For a single filament, we take the depolymerisation rate to be constant; it has been shown that the GTP hydrolysis rate in FtsZ filaments is much higher at the ends than in the middle [Mateos-Gil et al., 2012], and therefore we consider monomers to be dissociating from the ends and that no breakage of filaments can happen during the simulation. Since we consider the number

of ends to stay constant, there is no reason for the depolymerisation rate to be variable.

The binding of new cross-linkers happens independently at each possible binding site. In this case, that is the whole overlapping region except for the sites already occupied for existing cross-linkers. Therefore, we have

$$k_{bind} = k^0_{bind}(L_f - L - n) \tag{3.34}$$

where k^0_{bind} is the binding rate per free binding site and n is the number of existing cross-linkers in the system. This changes over time during the simulation, and therefore the effective rate k_{bind} is also variable over time, increasing with increased overlap and decreasing cross-linker quantities.

Conversely, the unbinding of cross-linkers also happens at each one of them independently, meaning there is a typical time scale for the life of a cross-linker. The effective unbinding rate is, therefore, proportional to the number of bound cross-linkers in the system:

$$k_{unbind} = k^0_{unbind} n \tag{3.35}$$

this is also variable over time.

The fact that we have kinetic rates that are variable over time would pose a problem to our simulations if we were not assuming processes to be Poissonian. Since they have the property of being memoryless, every time any rate changes in time (i.e. at any time the number of cross-linkers change or the overlapping region size changes) we can simply re-sample the waiting time for the next event from an updated exponential distribution with the new rate without issue.

Thus, by having the reactions set up through the calculation of waiting times to the next event allow us to simplify the code by using an event-driven algorithm and have a "clock" that immediately advances to the next reaction event instead of having to check for them at every single time step.

3.2.5 Metropolis Algorithm

In the presence of these reactions, we must account for the changes in entropy and free energy with regards to the actual event happening, to make sure that

event transitions obey detailed balance; in that sense, we have decided to use a Metropolis algorithm for our simulation. Negative changes in free energy are accepted, and positive ones are accepted with probability

$$p = e^{\frac{-\Delta E}{k_B T}} \tag{3.36}$$

That means that the probability of acceptance decreases exponentially with the size of the energy barrier that would need to be "climbed" for that event to happen.

The free energy of the system can be described by

$$E = U - TS \tag{3.37}$$

where U is the internal energy of the system and S is the entropy. We can easily calculate the entropy from the partition function Z presented at Eq. (3.8) using the expression

$$S = -k_B \ln Z \tag{3.38}$$

and, therefore, we can rewrite the free energy as

$$E = U - k_B T \ln Z \tag{3.39}$$

For any given reaction, we can then calculate the change in free energy ΔE

$$\Delta E = E - E_0 = U - U_0 - k_B T \ln \frac{Z}{Z_0} \tag{3.40}$$

where the subscript 0 is given for the values before the reaction occurs.

Alternatively, we can write the expression for the change in free energy ΔE as

$$\Delta E = \Delta U - k_B T \ln \frac{Z}{Z_0} \tag{3.41}$$

Since we already have an expression for Z given L_F, L, n and δ, we just need expressions for ΔU for each possible reaction to have their equivalent ΔE expressions that will allow us to test them according to the Metropolis scheme. Since ΔU represents the change in internal energy of the system when a certain

reaction happen, we can certainly do that.

For depolymerisation, the reaction corresponds to the loss of a binding site and hence an increase in internal energy. However, a single monomer gains entropy when going from a bound state to an unbound state in the bulk. For a given temperature, we can conflate both effects, with appropriate signs, into a single value E_s; that is a parameter in our model that quantifies how favourable depolymerisation is, and it is also the change in internal energy ΔU for a depolymerisation reaction.

Upon binding of a cross-linker, we gain the binding energy between a cross-linker and two sides of the filament, while losing the translational entropy of the cross-linker, since it becomes bound. The freedom it has when bound is already accounted for in our system entropy calculated in Eq. (4.22). Again, we can conflate both effects in a single parameter E_b that indicates how strongly bound cross-linkers are. Importantly, the unbinding process is the exact reverse of this, and therefore there are no extra parameters. The difference in internal energy ΔU is, therefore, $-E_b$ for the binding process and E_b for the unbinding process. E_s is defined negative and E_b is defined positive.

Finally, we can write expressions for the change in free energy ΔE for our three processes as:

$$\Delta E_{depol} = E_s - k_B T \ln \frac{Z}{Z_0} \tag{3.42}$$

$$\Delta E_{bind} = -E_b - k_B T \ln \frac{Z}{Z_0} \tag{3.43}$$

$$\Delta E_{unbind} = E_b - k_B T \ln \frac{Z}{Z_0} \tag{3.44}$$

Note that the second term of all of those expressions are negative in case $Z > Z_0$, that is, in case the reaction means the system can have more possible microstates; those reactions are, therefore, more likely to happen and be accepted. The effect of binding energies and bulk entropies depend on the signs and magnitudes given to the parameters E_s and E_b.

We finally have all the pieces necessary for simulating this system. We have decided how to calculate the entropic forces trying to expand the overlapping region, how often different events will take place and how to evaluate those, based on the change in entropy and internal energy they require. In the

next section, we present the results achieved from the simulations performed.

3.3 Results

3.3.1 Computational model agrees with analytical and experimental data

The simplest possible application of our model is to replicate the results from the analytic model developed by Lansky et al. [Lansky et al., 2015]. In this approximation, there are two filaments of constant size cross-linked by a constant number of cross-linkers; no binding or unbinding occurs [Braun et al., 2011].

In this case, the expansion force behaves like an one-dimensional analogue to the ideal gas law, and their analytical model predicts correctly the range of maximum forces generated by the system and the trend of measured velocities qualitatively; quantitative tests are difficult due to experimental uncertainty.

Given that our model calculates the partition function of the system in precisely the same way as their analytic model, it is no surprise that their analytic results are replicated exactly by our computations. Their figure of approximately 2.4 pN of maximum force in a system with 100 cross-linkers is exactly what our model generates, as indicated in Fig. 3.3.

We can also recover the result that forces scale linearly with cross-linker density in the overlap, in the low-density case. In the previous section, we have also shown that the overlap expansion velocities agree with the predicted values, including the fact that velocities do not depend on the number of cross-linkers at the overlap region when the density of cross-linkers in the overlap $n/l \ll 1$.

3.3.2 Helical geometry generates contractility

Next, we will use the helical filament geometry previously presented. The inspiration for this geometry comes from bacterial cell division, where it is thought that FtsZ filaments form a ring-like structure [Ma et al., 1996; Haeusser

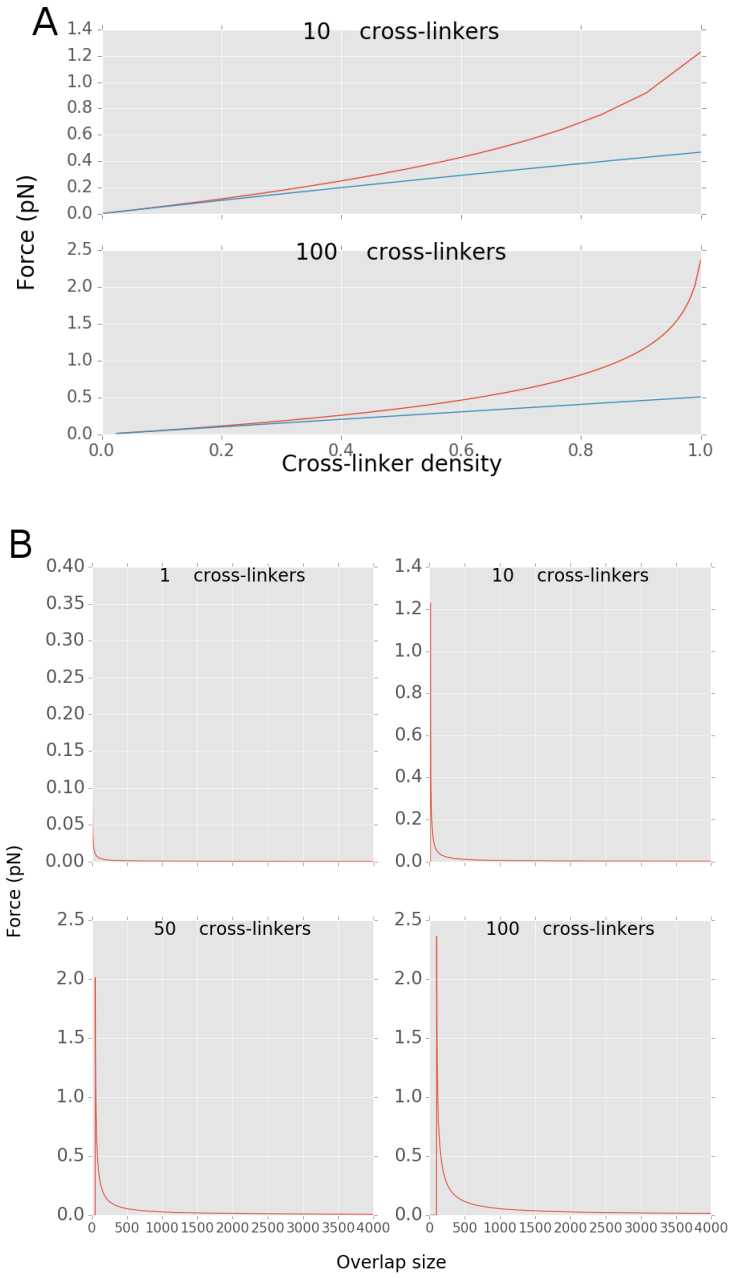

Figure 3.3: Comparisons between computational results from our model and analytical predictions from Lansky et al. [Lansky et al., 2015] A) Overlap expansion force for 10 and 100 cross-linkers. We confirm the maximum value of 2.4 pN for 100 cross-linkers when all overlap sites are occupied and the linear increase in force with cross-linker density for small densities. Blue lines are linear predictions from a one-dimensional ideal gas law, red lines are computational calculations. B) Force values (in pN) as a function overlap size for different numbers of cross-linkers.

and Margolin, 2016] at the center of the cell and generate contractile force [Erickson, 2009].

The simplest system to test the contractile potential of this system using diffusible cross-linkers is a single helical filament that is long enough to be cross-linked to itself, as shown on Figure 3.1.

In our computational model, we define a region of interest with a length that will define the filament's curvature radius; radial contractility, therefore, is equivalent to a decrease the filament turn length (defined as the helical length between laterally interacting monomers), and therefore in the area size. Inside this area, our initial set up places a filament of length L_f. Since we are interested in lateral interactions of this filament with itself, we establish that our area has total length $2L$ with turn length L, such that $L < L_f < 2L$. The overlap length is, therefore, the filament length that exceeds the turn length, or $L_f - L$. The choice of limiting total filament length to two turn lengths is purely for convenience.

As in the microtubule overlap experiment, we can introduce n cross-linkers in the overlap region and study the resulting force and velocity. Just like with the microtubules and as we have shown in the previous section, even the presence of a single cross-linker drives the overlap to expansion, which means that a contractile force is generated, since a decrease in the turn length L means an increased overlap. However, the filament curvature needs to be taken into account; increasing the filament curvature is energetically unfavourable if its intrinsic curvature is lower than the current one [Landau and Lifshitz, 1958; Kratky and Porod, 1949].

A first consistency check that can be performed in this new geometry is comparing our results with the ideal gas law. In the dilute limit where the density of cross-linkers in the overlap region is small, they should agree. We have presented the theoretical background for calculating analytically the equilibrium lengths based on the one-dimensional ideal gas law in Section 3.2.3.

Figure 3.4 shows the results of this comparison. In fact, we can see that, contrary to the predictions in the previous section, the ideal gas law slightly overestimates the available force rather than underestimate it. This is due to the decreasing rotational freedom when the radius of the filament decreases, which is a factor not accounted for in the ideal gas law.

Furthermore, when we increase the filament rigidity, not much contraction is achieved and the system is "stuck" on a configuration of smaller overlap size; a consequence is that the dilute limit approximation may start to break down, and the ideal gas law, even without taking the rotational freedom into account, starts underestimating the force once again. This is the case for the very last point at the top right of Fig. 3.4.

We can now study the effect of filament rigidity on the equilibrium length attained by the system, in the absence of depolymerisation and addition or removal of cross-linkers. In this configuration, the filament size will not change at all over time.

Fig. 3.5 illustrate our findings. Here, we are using a monomer size of 5 nm [Mingorance et al., 2005; Lan et al., 2009] as opposed to the 8 nm of the microtubules [Holy and Leibler, 1994]; this reflects the difference in size between FtsZ and tubulin. The addition of cross-linkers makes the filament capable of constriction, with the final curvature being limited by its persistence length and intrinsic curvature.

If we want to approximate this system to our model system of bacterial cell division, we can think of this filament strongly bound to a membrane. Now, contraction needs to not only change curvature on the filament, but also on the membrane [Helfrich, 1973]. Reducing the system size requires a force strong enough to surpass both requirements. The degree of constriction achieved is now limited by both the filament's and membrane's rigidity and intrinsic curvature, but the dynamics are not substantially changed.

3.3.3 Filament dynamics can create sustained contraction

In order to achieve constriction couple to filament kinetics, we need to introduce filament depolymerisation. We will limit ourselves to dealing with depolymerisation in this section; the assumption is that no membrane-bound monomers or polymers are added to the system and that we are only interested at the single-filament level. More details about assumptions and implementation of our model are given in Section 3.2.

Our filament depolymerises with a constant kinetic rate k_{off}. We con-

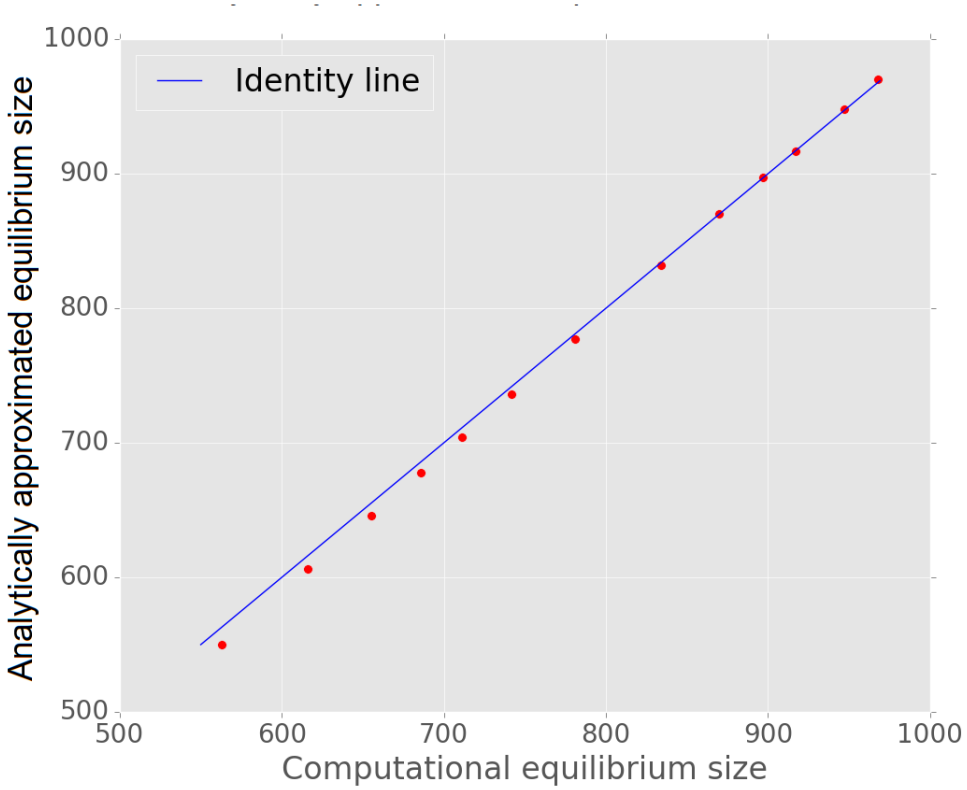

Figure 3.4: Comparison between the analytically predicted equilibrium lengths (defined as 2π times the radius of the contractile zone) and the computational results, given different filament rigidities. The equilibrium length is underestimated by the ideal gas law, meaning that the contractile forces are overestimated. This is due to the decreasing rotational freedom of the filament being neglected in the analytical calculations. The starting point for these systems is $L_f = 1100$, $L = 1000$ and $n = 10$. Cross-linkers were given infinite binding energies. Filament bending rigidities varied from 20 to 500 arbitrary units.

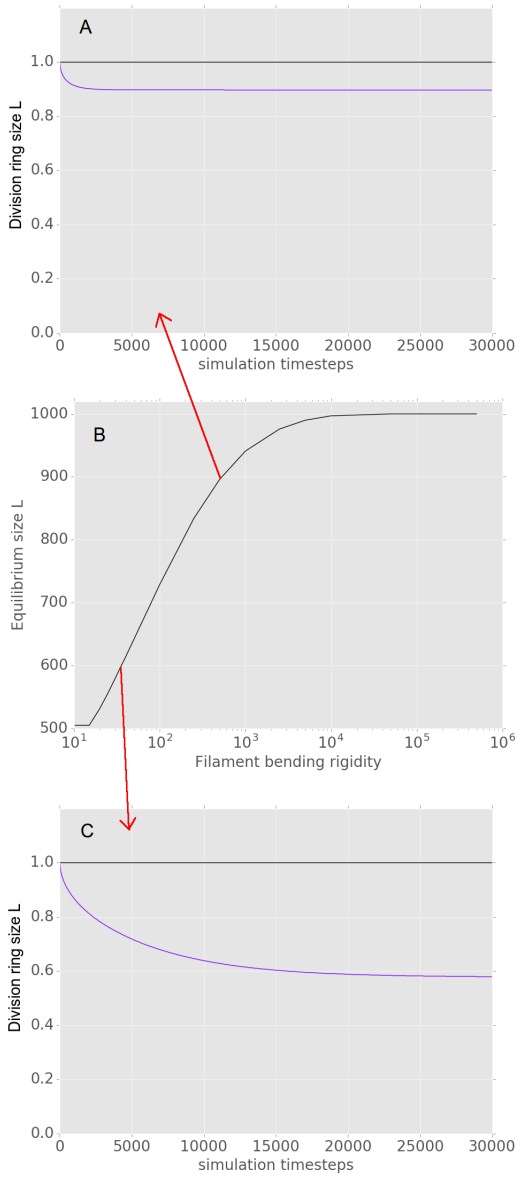

Figure 3.5: Filament rigidity determines the final state of a system without depolymerisation, addition or removal of cross-linkers, but contraction is achieved for the whole range of parameters. Plots A and C show the contraction curves for two examples: one with low rigidity (A, 30 arbitrary units) and one with high rigidity (C, 750 arbitrary units). All cases consider the filament to have intrinsic curvature equals to $1/L_0$, where L_0 is the initial length of the system, so that absence of contractility would yield an equilibrium length L_0. Low-rigidity systems contract until the filament nearly fills available space. Initial conditions for these simulations was $L_0 = 1000$, $L_f = 1010$ and $n = 10$, meaning that we start at the point of maximum force. System sizes are shown as relative to initial turn length.

sider this rate to be independent of filament size, given that depolymerisation will only happen from the ends [Mateos-Gil et al., 2012]. Now, the value L_f is a decreasing variable, meaning that our previous limits for maximum curvature (as shown in Fig. 3.5) do not apply any more.

We present the results in Fig. 3.6. Here, we can see that depolymerisation tends to shorten overlap length, as opposed to contraction, which means the contractile force does not decrease as it previously did and the constriction can be more pronounced than in the same system without depolymerisation. Thus, depolymerisation acts to keep cross-linker density high, and therefore increase the contractile force.

Changing the value of the depolymerisation kinetic rate k_{off} allow us to access different regimes of contraction. In summary, there are two possible limiting factors for contraction speed: the depolymerisation rate or the effective cross-linker friction γ_{MT} mentioned in Eq. (3.13). High friction means the turn length decreases slower for the same force.

Importantly, to be able to calculate the partition function (and, hence, the force), we assume that cross-linker diffusion is fast when compared to the rate of change in overlap length, meaning that cross-linkers can equilibrate after each change in overlap length and ensemble approaches can be applied.

At low depolymerisation rates (and/or low cross-linker friction), changes in turn length occur relatively fast compared to depolymerisation and we hit the same minimum system size as in the previous case; that is, turn length cannot decrease because the filament nearly fills the system. Contractility becomes, then, limited by the depolymerisation rate; it has been shown that the rate of GTP hydrolysis, which is analogous to the depolymerisation rate, correlates with cytokinesis rate [Bisson Filho et al., 2016].

At higher k_{off} values (and/or higher cross-linker friction), the overlap length decreases until cross-linker density is high and it remains so, which means that we are always close to maximum force. Contraction proceeds at a rate that is mostly determined by the friction caused by the cross-linkers, until that force is insufficient to bend both filament (and structures bound to it, if present) any further, as shown in Fig. 3.7.

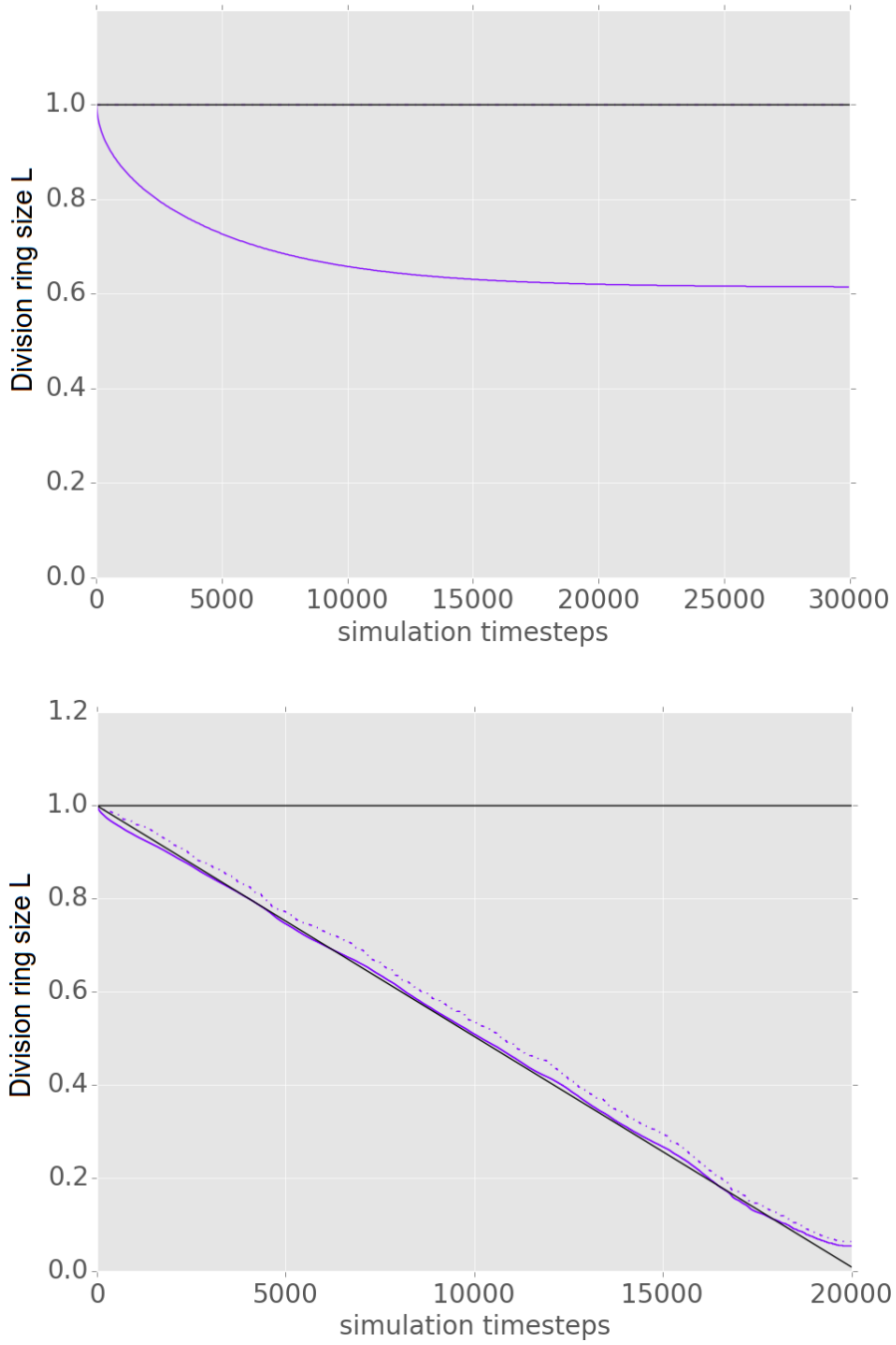

Figure 3.6: We compare the same system with and without depolymerisation kinetics, for a single realisation. Without it, contraction stalls relatively early in the process, while the system with depolymerisation can keep shrinking to much higher curvatures. Solid lines are turn lengths, dashed lines are filament sizes. Black line represents the theoretical prediction for free depolymerisation. Both turn lengths and filament lenghts are presented in relative terms to their initial values.

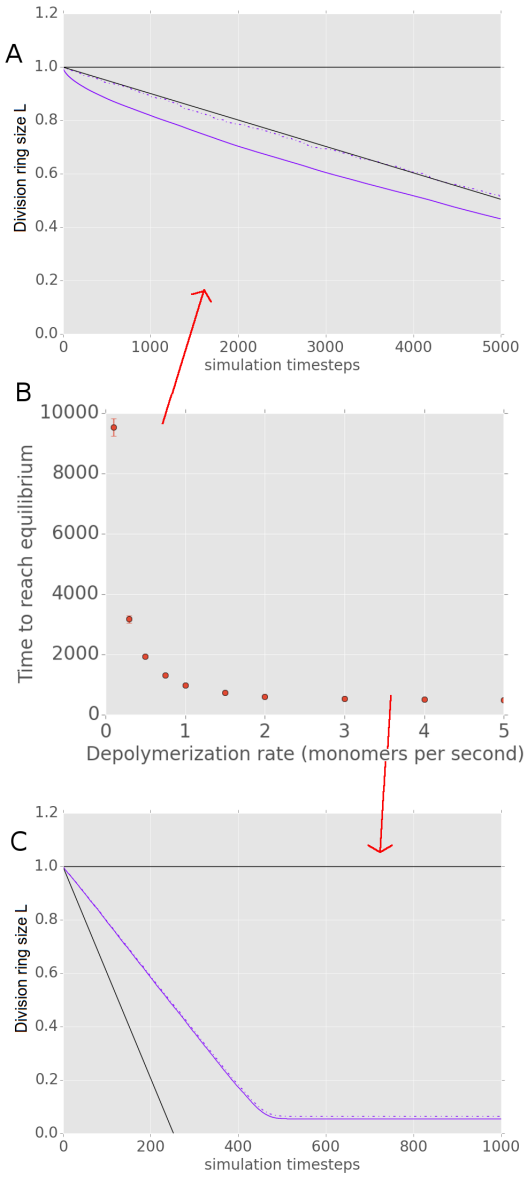

Figure 3.7: Different contractility regimes depending on depolymerisation rate. A) low depolymerisation rate of 0.01 monomers per simulation time step means that contraction events are limited by the the depolymerisation rate. B) Time to reach equilibrium verus depolymerization rate. C) faster depolymerisation with rate 1.00 monomer per simulation time step mean that the system leaves the depolymerisation-limited regime before reaching the stalling point defined by filament stiffness and membrane tension. In this regime, contraction velocity depends only on the net force being generated and the cross-linker friction. Solid lines are system sizes, dashed lines are filament sizes. Black line represents the theoretical prediction for free depolymerisation. Both turn lengths and filament lenghts are presented in relative terms to their initial values.

3.3.4 Cross-linker kinetics are central to model filament constriction

In this section, we want to test two scenarios related to cross-linker kinetics: in the first one, we introduce cross-linkers in the overlap region at the beginning of the simulation and they can unbind from the filaments, but no new cross-linkers bind to it. This scenario mimics the experiment where, after Ase1 molecules bind to microtubules, unbound Ase1 molecules are washed away and no extra binding happens [Lansky et al., 2015]. Depolymerisation can still happen.

In the second scenario, we simulate a situation where the experimental buffer would be rich with cross-linkers; the initial system only presents an overlap region, but no cross-linker is bound to it yet. Here, we test how binding (k_{bind}) and unbinding (k_{unbind}) kinetics influence the contractile mechanics. The kinetics for binding are assumed to be proportional to the number of available overlap sites, and those for unbinding are proportional to the number of bound cross-linkers. Also here the filament is free to depolymerise.

We obtain the insight that the cross-linkers need to be strongly bound to the filaments for contraction to occur, as can be seen from Fig. 3.8. In short, when cross-linker pressure builds in the overlap region, the system is faced with two options to relieve it: remove a cross-linker or reduce the system size and, therefore, increase the overlap region length (or stall, if the mechanical restoring force is large enough). When the cross-linker binding energy is not strong, the former is more energetically favourable than the latter, and thus we end up with a system with no cross-linkers and no contractility.

On the other hand, when depolymerisation becomes necessary for further contraction (i.e. the density of cross-linkers is close to 1), removing monomers requires the removal of cross-linkers as well, since our model does not allow for cross-linkers to be bound in only one side. Large binding energies for the cross-linkers make this process harder, and further contraction more difficult. This situation is exemplified in Fig. 3.9. It seems that binding energies for the cross-linkers need to be very carefully poised between being able to stay bound when pressure builds in the overlap region but unbind when in the dense limit.

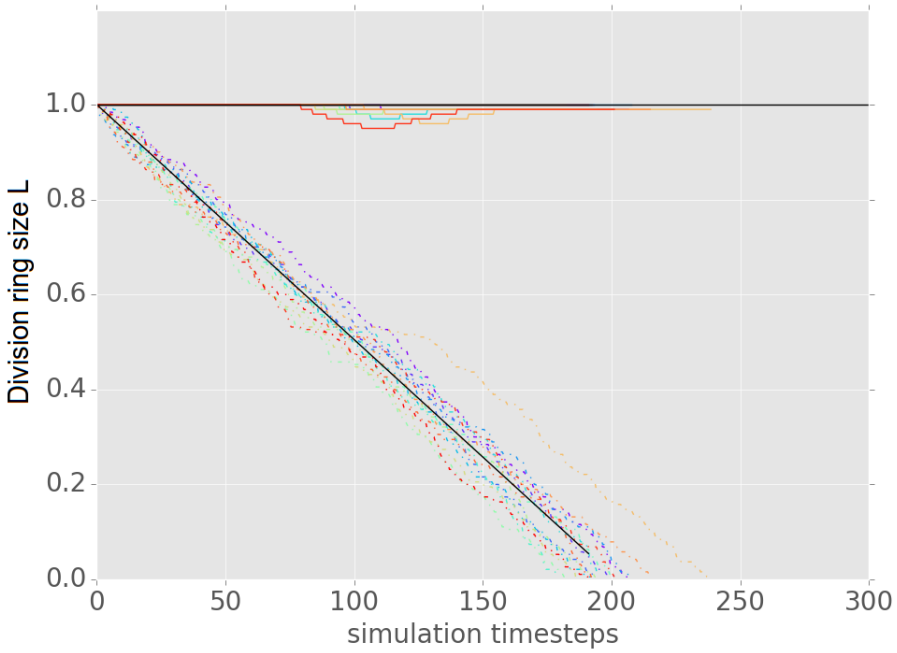

Figure 3.8: System with weakly-bound cross-linkers. When the system achieves enough entropic force to drive contraction, that pressure can be relieved by removing the cross-linkers instead of reducing the system size, and in this scenario that is what happens. Free from cross-linkers, the filament depolymerises freely and the system size relaxes to equilibrium. Solid lines are system sizes over 16 realizations (different colours for different realizations), dashed lines are filament sizes. Sloped black line represents the theoretical prediction for free depolymerisation. Both turn lengths and filament lenghts are presented in relative terms to their initial values.

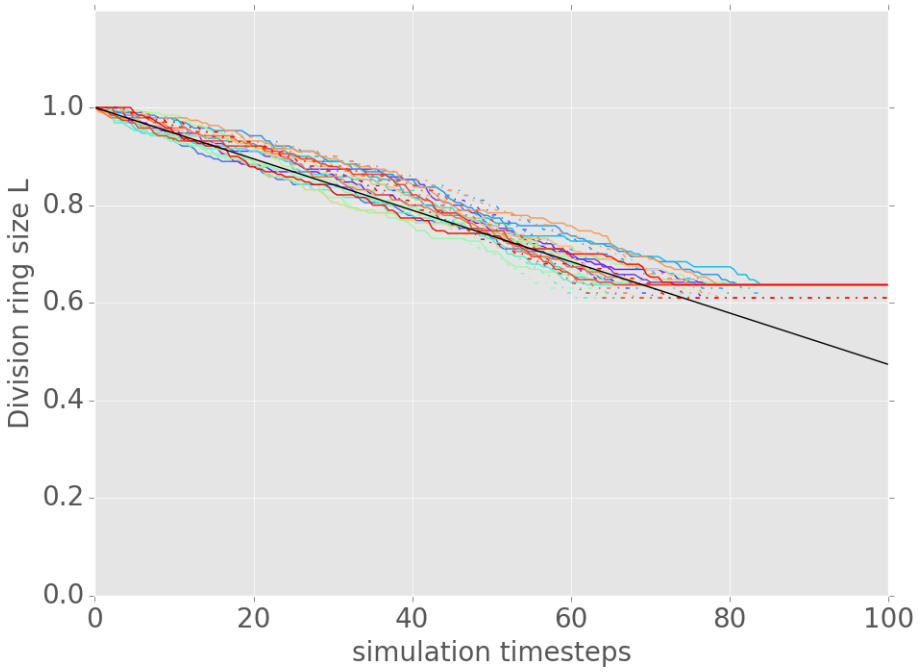

Figure 3.9: System with strongly-bound cross-linkers. When the system reaches a dense state and needs further depolymerisation to keep contracting, cross-linkers with high binding energies can impede that process.The filament stops depolymerising and contraction stops. Solid lines are system sizes over 16 realizations (different colours for different realizations), dashed lines are filament sizes. Sloped black line represents the theoretical prediction for free depolymerisation. Both turn lengths and filament lenghts are presented in relative terms to their initial values.

We uncover an interesting interplay between the filament depolymerization and cross-linker binding rates, as can be seen from Fig. 3.10. When depolymerisation is fast compared to binding, the overlap region becomes very short very rapidly, and the few available overlap sites mean that few cross-linkers are introduced into the system. In fact, the relatively few free overlap region binding sites mean that the rate of cross-linker binding is also reduced.

Consequently, the maximum force that the system can achieve will not be large when compared to systems with slower depolymerisation, but at the same time the cross-linker friction is low; contraction is arrested early, but the equilibrium length is achieved quickly. When the opposite is true, there is time for many more cross-linkers to bind (and at a higher rate) before filament size decreases. Therefore, the maximum force is larger and contraction is arrested much later, but happens at a slower pace due to the increased cross-linker friction.

It is clear, then, that when it comes to a fully dynamic system, there is a trade-off to be achieved: to achieve maximum contractility, lower depolymerisation is required. The downside is the much longer time scale to achieve it. To achieve fast contraction, higher depolymerisation rates are required, although contraction may be reduced.

3.4 Discussion

3.4.1 The presence of diffusible cross-linkers generates contractility in helical filaments

Out model system mimics the experimental system involving microtubules and the cross-linker Ase1 [Braun et al., 2016; Lansky et al., 2015]. Our helical filament exhibits contractile behaviour in the presence of diffusible cross-linkers. The entropic force present in a filament overlap acts to expand the overlap length, causing the effective force to be contractile. This effect is independent of filament rigidity or length, provided there is a lateral overlap and diffusible cross-linkers present.

In fact, this is an effect that is independent of depolymerisation, binding or unbinding of cross-linkers; as long as the basic building blocks are in place,

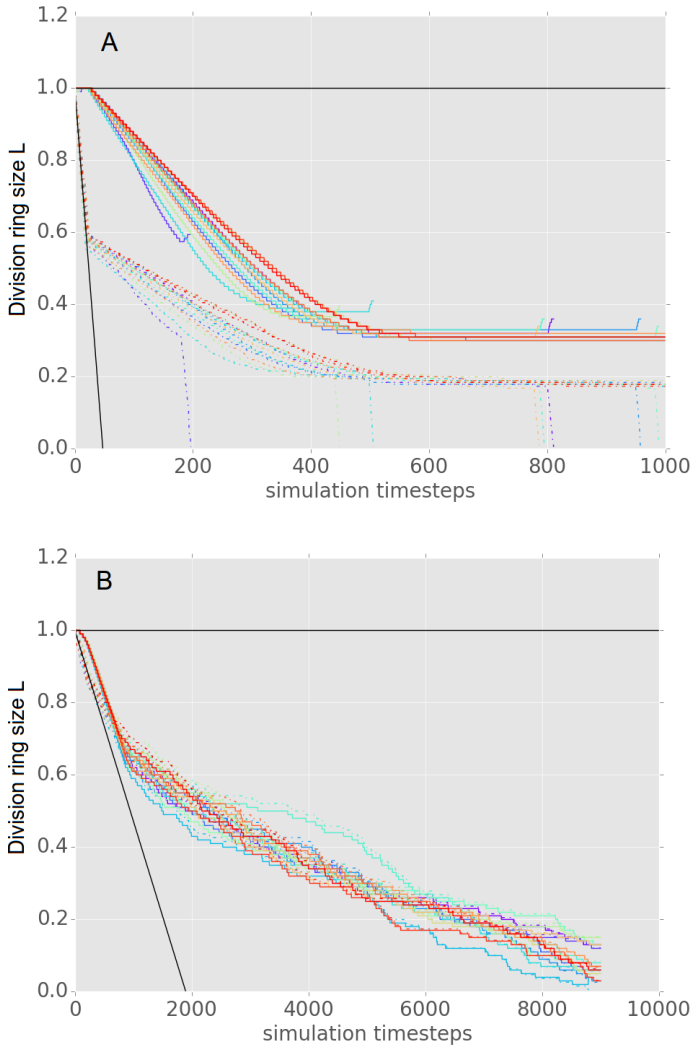

Figure 3.10: Different contractility regimes depending on the interplay between depolymerisation rate and cross-linking. Cross-linking rate is constant at 0.01 cross-linker added per free overlap site per simulation time step. A) High depolymerisation rate of 4.0 monomers per second means that the filament shortens quickly, fewer cross-linkers bind to it, and maximum contraction is small but fast. B) lower depolymerisation rate of 0.1 monomer per simulation time step mean that more cross-linkers bind to the filament. Further constriction can be achieved, but at a slower rate (note the different time scales). Solid lines are system sizes over 16 realizations (with different colours for different realisations), dashed lines are filament sizes. Sloped black line represents the theoretical prediction for free depolymerisation. Both turn lengths and filament lenghts are presented in relative terms to their initial values.

the contractile force acts without any need of protein binding or unbinding.

The contractile force is capable of overcoming filament (and eventual membrane) rigidity to cause effective contraction of the system. Conversely, it is possible to derive the values of the relevant rigidities from the contraction curves; we expect this to be an alternative method for experimental calculation of system stiffness in the presence of diffusible cross-linkers.

3.4.2 Depolymerisation kinetics are essential for sustained contractility

Assuming that filaments (and membranes) have rigidity and intrinsic curvatures, and that forces decrease very rapidly with increased overlap length, a system with no depolymerisation kinetics will stall. From the initial state, the overlap length will increase, decreasing the entropic force and allowing for the existing rigidity to impede any further contraction.

There are two possible mechanisms for achieving contraction: increase the density of cross-linkers in the overlapping region, by either having more cross-linkers binding there, or reduce the length of the region by depolymerisation of the filament. We would argue that, in our biological model system, a depolymerisation-based system makes more sense, since increasing the number of cross-linkers would probably require up-regulating the production of proteins, and there would be a significant lag involved in this process that is inconsistent with the quick dynamics seen *in vivo* during bacterial division.

A minimal requirement to achieve sustained constriction is depolymerising the filaments. Depolymerisation decreases the overlap length, increasing the cross-linker density (and therefore the contractile force) doing work against the contractile restoring force. The energy stored in the polymerised filament is, thus, effectively harnessed to achieve further constriction.

Furthermore, we have shown that the kinetics of cross-linkers can affect the contraction. Weakly-binding cross-linkers will mean that pressure in the overlapping region acts to remove the cross-linkers rather than to contract the system, meaning that effective constriction is only achieved in systems with strongly-bound cross-linkers. However, very strongly bound cross-linkers will inhibit further contraction when they become dense. The binding energy of

the cross-linkers is a sensitive control parameter.

When binding kinetics are incorporated into the model, the number of cross-linkers in the overlap can increase, the balance between binding and depolymerisation kinetics is essential: fast depolymerisation leads to a low number of cross-linkers, which means lower maximum force and faster constriction, while slower depolymerisation rates allow for more cross-linkers to bind and take constriction further, albeit at a slower pace.

3.4.3 Range of generated forces is biologically relevant

Our work shows that the maximum entropic forces of overlap expansion are in the range of few piconewton. This result agrees with the experimental data derived from the experiment with microtubules [Lansky et al., 2015], and it would be greater in a system with FtsZ filaments because the FtsZ monomer size is smaller than tubulin.

Considering the cell wall remodelling machine at work during bacterial cell division, the FtsZ ring would need to exert a force of roughly 8 pN [Lan et al., 2007] to drive division; while our system does not achieve this value, it is simple to see that in the existence of multiple non-interacting filaments the forces would add up. Therefore, a handful of filaments with enough cross-linkers could easily achieve this task.

Chapter 4

Multi-filament dynamics

4.1 Introduction

In the previous chapter, we have shown that, given a certain helical geometry and the presence of diffusible cross-linkers, we can harness entropic forces to generate a contractile effect. This subcellular process to generating directed forces can, now, be generalized for the case of multiple filaments.

Contractile bundles have been studied before: in particular, an essential part of the eukaryotic cytoskeleton is formed by bundles consisting of filamentous actin and myosin motors [Warshaw et al., 1990; Onishi et al., 2006]. These are responsible for contraction and force generation in both muscle and nonmuscle cells [Sellers et al., 1981; Lowey and Trybus, 2010].

This particular kind of bundle can appear in many different compositions and configurations, being used for muscle contraction [Lowey and Trybus, 2010], cell migration [Sabass et al., 2008] and cell division [Enrique et al., 2000]. In this case, the mechanics involved in generating forces are well understood at a microscopic level, and they involve the action of myosin as a molecular motor [Walcott et al., 2009].

Therefore, these systems are very different from the ones we are concerned with at a very fundamental level: our systems do not present any molecular motors, and force generation needs to arise purely from entropic forces at filament overlaps rather than by the directed motion of a protein.

Furthermore, there is no equivalent to the Lansky experiment [Lansky et al., 2015] for bundles of filaments. In this chapter, we will extend the two-

filament experiment to model systems with an arbitrary number of filaments and cross-linkers. We show that, under certain circumstances, these will also generate contractile directed forces. We are able to relate the kinetics and dynamics from bacterial division to results predicting constriction and the onset of cytokinesis.

As in the previous chapter, we establish a computational model that calculates entropy by explicitly counting the number of possible microstates a given configuration of a system can access, a more complex affair than previously. This is complemented by similar dynamics for cross-linkers and depolymerisation of filaments as was employed for the single-filament studies. Here, the filaments will exist in a ring-like region of space, and co-alignment is assumed a priori; this seems to be a reasonable assumption given the structure of the Z-ring [Szwedziak et al., 2015].

This extension of the single-filament model to a multi-filament model will allow us to add new filament kinetics related to filament addition, allowing us to study contractility in a more realistic model that more closely reflects the *in vivo* case. We make predictions for contractility and the onset of cytokinesis.

4.2 Theoretical Background

In this section, we first outline the physics of the model. Then, we overview our computational model, and look further into how the kinetics and dynamics of binding and unbinding are implemented in multi-filament systems. Finally, we will discuss the Metropolis algorithm that used in this chapter to simulate the temporal evolution of our systems.

4.2.1 Analytic Expressions

Here, we are concerned with systems of multiple (helical) filaments in a ring-like region, as presented in Figure 4.1. This allows us to establish a model of the Z-ring that is more realistic.

We can still write an approximate equivalent pressure for this system as

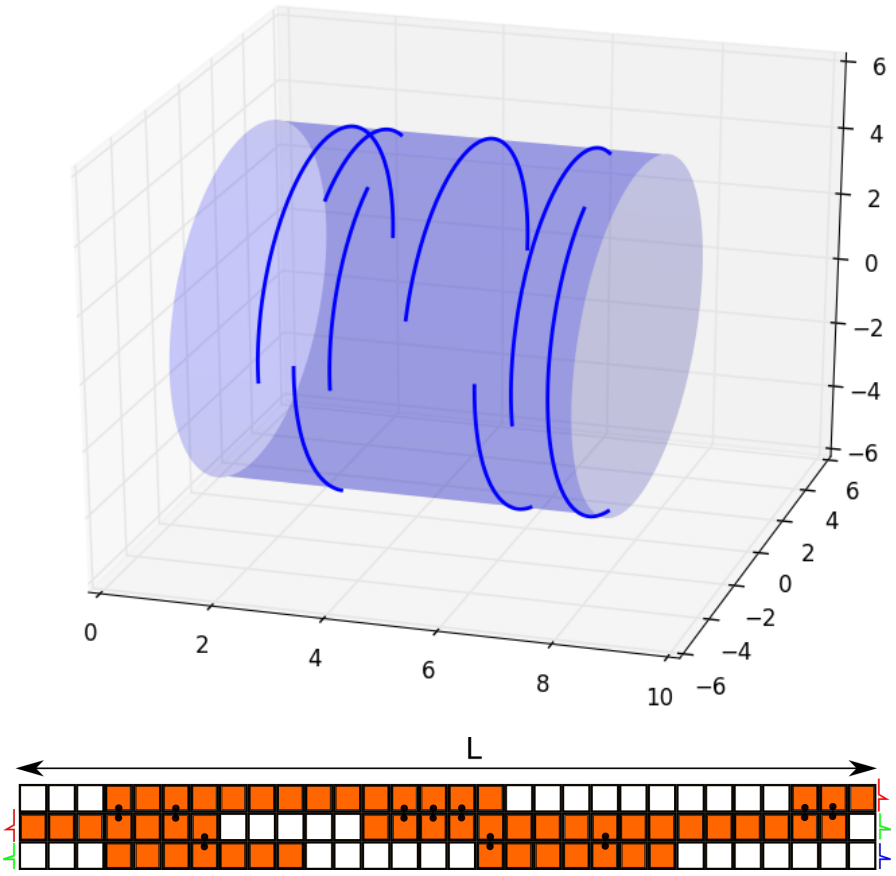

Figure 4.1: System with multiple (helical) filaments. In this system, $L = 2\pi R$ where R is the mean curvature of the ring-like cylindrical region where the filaments are contained. Length units are arbitrary./ Below, as an example, we see a two-dimensional lattice representation of what a system with three turn lengths could look like. Orange sites are occupied, white sites are empty and the two-headed black structures are cross-linkers

$$P = \frac{\Delta E}{\Delta L} = \frac{\Delta E}{\delta} \tag{4.1}$$

Which means that, for constant internal energy in the system, the contractile force can still be written as

$$F = \frac{T\Delta S}{\delta} \tag{4.2}$$

and it still depends only on the change in entropy. Finally, we can write the force expression as

$$F = \frac{k_B T}{\delta} \ln \left[\frac{Z(L-1)}{Z(L)} \right] \tag{4.3}$$

where $Z(L)$ is the partition function given the turn length L defined by the mean curvature radius R of the region where filaments are contained. For convenience, since we are interested with contractility, we make the dependence of Z on L explicit, but it also depends on the filaments and cross-linkers. From now on, we will consider this region to be a "membrane"; later on, we will apply the Helfrich hamiltonian to calculate the restoring force for systems outside the preferred membrane and filament mean curvature.

Importantly, there is no closed form, analytical expression for Z any more. This will still be proportional to the number of microstates accessible to a given configuration of the system, but calculating this number is now a difficult problem. By writing inequality constraints for the positions of individual filaments and cross-linkers, we can define a high-dimensional polytope, and then calculate the number of points with integer coordinates inside this polytope by using the algorithm detailed in Section 2.4.

The contractile force, now, depends non-trivially on both L and the specific configuration in which the system is at a given point, with no possible analytical solution.

Furthermore, this force is not necessarily contractile. In fact, we will show later that the net force is only contractile in very specific cases. To account for these cases, we also need to calculate the changes in free energy that an expansion event would cause.

In large systems, these changes in free energy would be the opposite of

each other. In our limited size model, we separate both cases by referring to the changes in energy by ΔE_{cont} and ΔE_{exp}, for contraction and expansion events, respectively. For constant internal energy, these quantities will only depend on their equivalent ΔS values. Thus, we need to calculate two values for ΔS, one for the entropy under a contractile event

$$\Delta S_{cont} = k_B T \ln \left[\frac{Z(L-1)}{Z(L)} \right] \tag{4.4}$$

and one for the entropy change under an expansion event

$$\Delta S_{exp} = k_B T \ln \left[\frac{Z(L+1)}{Z(L)} \right] \tag{4.5}$$

Usually, only one of those will be positive, indicating an increase in the number of accessible microstates and a preferred force direction, or both will be negative, indicating that the current size is a stable point for the turn length size L and the system configuration. The sign of ΔS indicates the directionality of the resulting force (contracting or expanding), and its magnitude is given by Equation (4.2).

We now come to the force-velocity relationship in this system. We assume the friction term to be dominated by the cross-linkers and approximate it as linear, arriving at

$$v = \frac{F}{\gamma} \tag{4.6}$$

with γ dependent on the number of cross-linkers. Given the previous expressions for force and changes in entropy, we could rewrite the contractile/expansive velocities as

$$v_{cont} = \frac{k_B T}{\delta} \frac{\ln \left[\frac{Z(L-1)}{Z(L)} \right]}{\gamma} \tag{4.7}$$

$$v_{exp} = \frac{k_B T}{\delta} \frac{\ln \left[\frac{Z(L+1)}{Z(L)} \right]}{\gamma} \tag{4.8}$$

Again, these would be the opposite of each other in large systems. Restoring forces will act where curvature deviates from the equilibrium value. We have

previously defined the radius of curvature R of the membrane as being $R = L/2\pi$. We can write the Helfrich hamiltonian [Helfrich, 1973] for the bending energy associated with this system as

$$H = \frac{1}{2}\int_S \kappa \left(\frac{1}{R} - c_0\right)^2 ds \tag{4.9}$$

or

$$H = \frac{1}{2}\int_S \kappa \left(\frac{2\pi}{L} - \frac{2\pi}{L_0}\right)^2 ds \tag{4.10}$$

where we approximate R as a constant. Here, $L_0 = 1/c_0$ is the inverse of the preferred curvature of the membrane and κ is a bending rigidity that can take into account both the cell membrane and the cell wall.

4.2.2 Our computational Model

In this section, we discuss how the simulation of this system over time is performed in different cases, mirroring similar procedures done in the previous chapter.

Here, we have also built three separate set-ups for our computational model: in the first one, we start from a system constructed by hand and allow no dynamics other than contraction and expansion; In the second one, we allow for depolymerisation of the filaments, but no binding or unbinding of cross-linkers. In the third one, we allow for full dynamics, including binding and unbinding of cross-linkers, addition of new filaments and depolymerisation of filaments.

In all of those set ups we allow the system to contract or expand, effectively changing curvature. Each individual lateral overlap is driven towards increase in overlap length; however, if these filaments have no constraints, no force will be generated since they can always instantly align to maximise the overlap size. When constrained, the contractile force will appear. At the same time, the steric interactions between filaments will generate an analogue of pressure, effectively causing an expansive force to exist, independently of the constraints on the filaments' positions. Furthermore, the membrane will effect a restoring force towards its preferred curvature, and that will be contractile

for very low curvature and expansive for high curvature.

Again, we identify Eq. (4.3) as the force, being an energy divided by a distance, i.e. the difference between the free energy of the system between two states, divided by the distance over which the difference in energies occurs. Therefore, we can define a difference in energy $\Delta\Omega$ for both contractile and expansive events:

$$\Delta E_{cont} = k_B T \ln\left[\frac{Z(L-1)}{Z(L)}\right] = k_B T \left(\ln\left[Z(L-1)\right] - \ln\left[Z(L)\right]\right) \tag{4.11}$$

$$\Delta E_{exp} = k_B T \ln\left[\frac{Z(L+1)}{Z(L)}\right] = k_B T \left(\ln\left[Z(L+1)\right] - \ln\left[Z(L)\right]\right) \tag{4.12}$$

Then, we need to incorporate the restoring forces into this picture to have a valid Hamiltonian for the system. We have written that expression before given the membrane bending rigidity κ and its preferred curvature c_0:

$$U(c) = A\frac{\kappa}{2}(c - c_0)^2 \tag{4.13}$$

where $c = 1/R$, and A is the area of the division ring. Again, we are approximating the radius of curvature R to be constant over the filament.

We can rewrite U to depend on L:

$$U(L) = A\frac{\kappa}{2}\left(\frac{2\pi}{L} - c_0\right)^2 \tag{4.14}$$

and, finally, we can put both things together for a single free-energy expression of the form

$$H(L) = A\frac{\kappa}{2}\left(\frac{2\pi}{L} - c_0\right)^2 - k_B T \ln\left[Z(L)\right] \tag{4.15}$$

Contractile and expansive events might cause changes with either positive or negative signs for the two parts of the previous equation, depending on how the curvature $1/L$ compares to c_0 and how the number of possible microstates changes with the aforementioned event.

4.2.3 Kinetics and dynamics

Similarly to the single filament case, we define our notation for the kinetics for processes to happen. This time, we will have four possible processes that involve binding/unbinding of structures in this system: addition of a new filament, depolymerisation of a filament, binding and unbinding of cross-linkers.

We still assume all processes to be Poisson processes, meaning that we can still calculate the time between two consecutive events from the probability density function

$$f(t,k) = \begin{cases} ke^{-kt}, & t \geq 0 \\ 0, & t < 0 \end{cases} \tag{4.16}$$

where k is the reaction rate for the process.

Instead of taking the depolymerisation rate to be constant, in this multi-filament environment we need to account for the number of filaments present in the system. We will still consider the filaments to only depolymerise from the ends, though; no breakage of filaments can happen during the simulation. Since the number of ends will scale with the number of filaments, we have

$$k_{off} = k^0_{off} n_{fils} \tag{4.17}$$

where n_{fils} is the number of filaments present in the system.

The binding of new cross-linkers happens independently at each possible binding site. In this case, that is each site in each overlapping region except for the sites already occupied for existing cross-linkers. Therefore, we have

$$k_{bind} = k^0_{bind} n_{over} \tag{4.18}$$

where k^0_{bind} is the binding rate per free binding site and n_{over} is the total length of lateral overlaps in the system. Note that this length will be different for different microstates.

Unfortunately, obtaining an ensemble average for n_{over} is not computationally feasible. However, we can sample a microstate at random and use its n_{over} instead. For that, we use the hit and run algorithm, as specified in Section 2.5.1. Evidently, these quantities changes over time during the simula-

tion, and therefore the effective rate k_{bind} is also variable over time, increasing with increased overlap and decreasing cross-linker quantities.

Conversely, the unbinding of cross-linkers also happens independently, meaning there is a typical time scale for the life of a cross-linker. The effective unbinding rate is, therefore, proportional to the number of bound cross-linkers in the system:

$$k_{unbind} = k^0_{unbind} n_{cross} \tag{4.19}$$

where n_{cross} is the number of cross-linkers in the system.

That, of course, is also variable over time. However, as opposed to the binding rate, it does not require sampling microstates.

Once again, we assume processes to be Poissonian. Since they are memoryless, every time any rate changes in time (i.e. at any time the number of cross-linkers change or a new filament is added to the system) we can simply re-sample the waiting time for the next event from an updated exponential distribution with the new rate without issue.

4.2.4 Metropolis Algorithm

As in the single filament case, also here we need to account for the changes in entropy and free energy with regards to the events, and make sure our event transitions obey detailed balance; in that sense, we will also use a Metropolis algorithm for our simulation, as detailed in Section 2.3. Negative changes in free energy are accepted, and positive ones are accepted with probability

$$p = e^{\frac{-\Delta E}{k_B T}} \tag{4.20}$$

just like before.

We will still write the free energy of the system as

$$E = U - TS \tag{4.21}$$

where U is the internal energy of the system and S is the entropy. We will calculate the entropy from the partition function Z using the expression

$$S = -k_B \ln Z \tag{4.22}$$

and, therefore, we can rewrite the free energy as

$$E = U - k_B T \ln Z \tag{4.23}$$

For any given reaction, we can then calculate the change in free energy ΔE

$$\Delta E = E - E_0 = U - U_0 - k_B T \ln \frac{Z}{Z_0} \tag{4.24}$$

where the subscript 0 is given for the values before the reaction occurs.

We can also write the expression for the change in free energy ΔE as

$$\Delta E = \Delta U - k_B T \ln \frac{Z}{Z_0} \tag{4.25}$$

We do not have a closed expression for Z, but we know how to calculate it. Therefore, we just need expressions for ΔU for each possible reaction to have their equivalent ΔE expressions that will allow us to test them according to the Metropolis scheme. Once more, ΔU represents the change in internal energy of the system when a certain reaction happen.

When a new filament is added to the system, the system gains the binding energy between each monomer and the membrane, and there is a loss of entropy from the unbound filament in the bulk. We will use ΔE_{mon} for the binding energy between a monomer and the membrane relative to a free monomer, and ΔE_{fil} for the entropy of the unbound filament in the bulk relative to the bound state.

For depolymerisation, the reaction involves the loss of a binding energy between two filament monomers, a binding energy between the monomer and the membrane and gains entropy for a single unbound monomer entering the bulk. For a given temperature, we can conflate the first and the last effects, with appropriate signs, into a single value ΔE_s; that is a parameter in our model that quantifies how favourable depolymerisation is. Given that we have defined ΔE_{mon} as the binding energy between a monomer and the membrane relative to a free one, the second effect has an energy difference of $-\Delta E_{mon}$.

For cross-linker binding, we gain the binding energy between a cross-

linker and two sides of the filament, while losing the bulk entropy of the cross-linker, since it becomes bound. The entropy it has then is already accounted for in our system entropy. Again, we can conflate both effects in a single parameter ΔE_b that indicates how strongly bound cross-linkers are. Importantly, the unbinding process is the exact reverse of this, and therefore no extra parameters appear. The difference in internal energy ΔU is, therefore, ΔE_b for the binding process and $-\Delta E_b$ for the unbinding process.

Finally, we can write expressions for the change in free energy ΔE for our four processes as:

$$\Delta E_{pol} = \Delta E_{fil} - l_i \Delta E_{mon} - k_B T \ln \frac{Z}{Z_0} \tag{4.26}$$

$$\Delta E_{depol} = \Delta E_{mon} + \Delta E_s - k_B T \ln \frac{Z}{Z_0} \tag{4.27}$$

$$\Delta E_{bind} = \Delta E_b - k_B T \ln \frac{Z(n+1)}{Z_0(n)} \tag{4.28}$$

$$\Delta E_{unbind} = -\Delta E_b - k_B T \ln \frac{Z(n)}{Z_0(n+1)} \tag{4.29}$$

where l_i is the length of the i-th filament, the one being added in the relevant event. It is important to clarify that Z and Z_0 are not the same in each of those expressions. Z_0 always refers to the partition function before the event and Z to the partition function after the event. In the case of binding and unbinding of a cross-linker, for example, they would just switch positions in the expression. Note that the final term of all of those expressions are negative in case $Z > Z_0$, that is, in case the reaction means the system can have more possible microstates; those reactions are, therefore, more likely to happen and be accepted.

We have defined how to calculate the entropic forces acting to expand the overlapping region, how often different events will take place and how to accept or reject those, based on the change in entropy and internal energy they require. In the next section, we present the results achieved from the simulations performed.

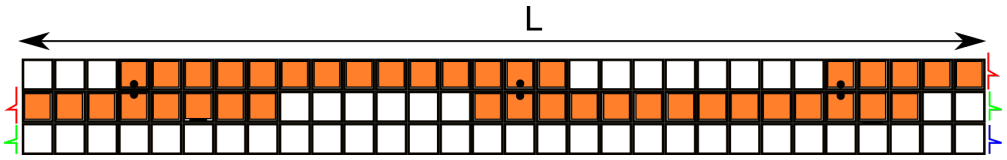

Figure 4.2: Minimum contractile bundle with three filaments and three cross-linkers. System size L defines the curvature of the membrane.

4.3 Results

4.3.1 Percolating clusters generate contractility

In this section, we study the contractile behaviour of bundles of filaments. As we did with single filaments, we will begin this by looking at the simplest possible systems, with the minimum amount of kinetics, and gradually move towards more complex systems with richer dynamics.

The simplest bundle capable of contraction that we can build is shown in Fig. 4.2. It includes three filaments and three cross-linkers, with each pair of filaments cross-linked to each other. We will show later that all cross-linkers are necessary for this bundle to be able to contract. This is the minimum number of filaments to achieve contraction because two filaments cross-linked to each other would, essentially, be similar to the system with two microtubules from Lansky et al. [Lansky et al., 2015]; the two filaments could always maximise their lateral overlap without needing to change the membrane curvature.

In this Subsection, we have defined a region of interest of three turn lengths of size 100 unless otherwise noted.

We define the concept of a percolating cluster as a structure made up of multiple filaments connected by cross-linkers that spans the whole circumference of the cell region and that is cross-linked to itself in a manner similar to the single filament systems presented in the previous chapter.

We construct two other simple systems that will be capable of contraction: one with five filaments and five cross-linkers, to evaluate how the size of a cluster impacts its ability to generate constriction, and one that will consist of two of the clusters presented in Figure 4.2 in parallel to each other, to investigate the effects of multiple percolating clusters. These two systems are

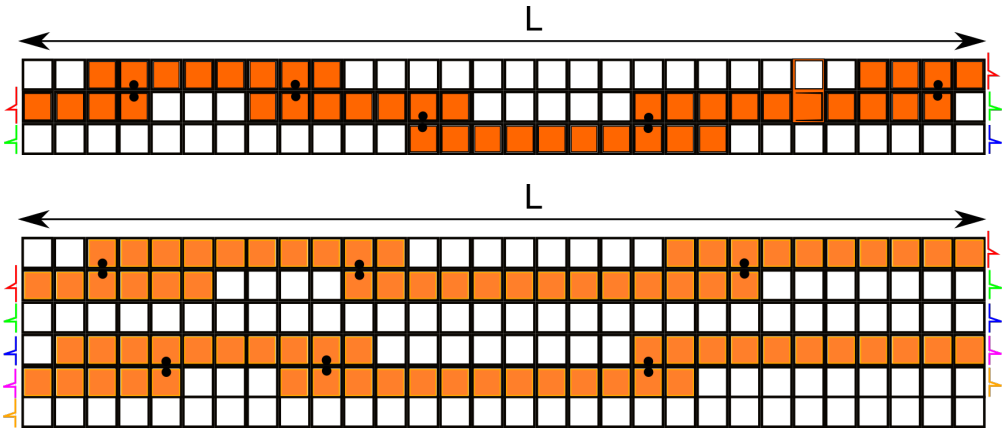

Figure 4.3: Two other simple systems capable of contraction that will be studied. ABOVE: bundle with five filaments and five cross-linkers. BELOW: two bundles with three filaments and three cross-linkers each, in parallel. System size L defines the curvature of the membrane.

presented in Figure 4.3. For the system with two parallel clusters, we have increased the region of interest to 6 turn lengths.

We can, now, study the behaviour of these simple systems in the absence of any dynamics. We temporarily suppress depolymerisation, binding or unbinding of cross-linkers and/or addition of polymers. In this way, we will look at the effect a configuration of filaments and cross-linkers has on the membrane curvature.

For simplicity, we will refer to these three systems as (A), (B) and (C), in the order they were presented in Figures 4.2 and 4.3. Starting with (A), we can see in Fig. 4.4 that the net force is initially contractile, increasing membrane curvature (by decreasing system size L). Since there is no depolymerisation, this causes the overlap regions to increase in size, decreasing the effective force. That proceeds until the net force reaches zero. Importantly, the net force here incorporates also the restoring force of the membrane being curved; that is why the net force will decrease to zero.

We compare that behaviour to what happens to system (B). (A) and (B) are qualitatively very similar, but with a different number of filaments and cross-linkers. As we can see in Fig. 4.4, the net force for this system is expansive. The contractile effect previously discussed is counteracted by the extra translational freedom the filaments would have if membrane curvature

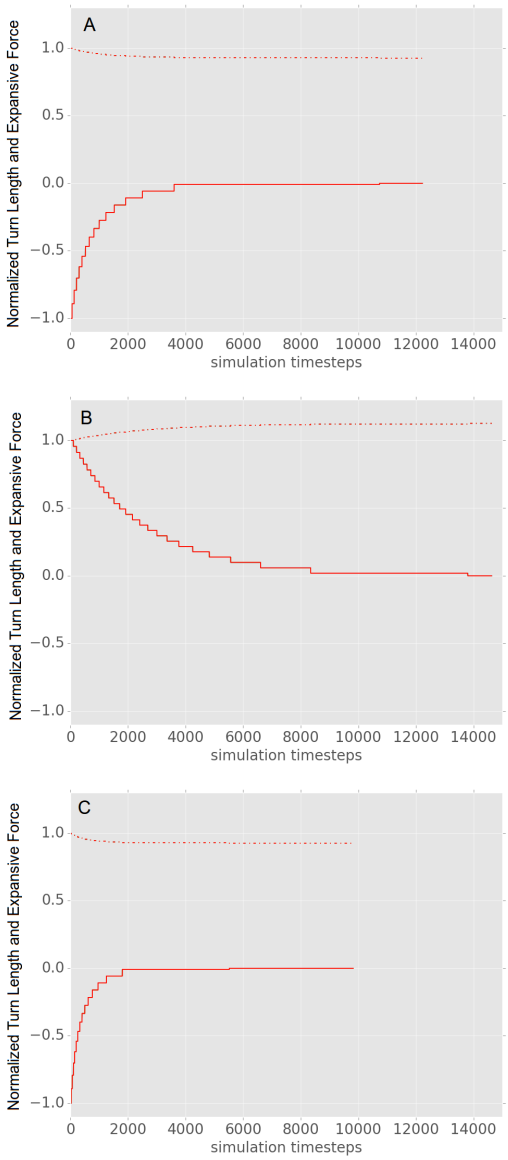

Figure 4.4: Normalized turn length (i.e. system size $L = 2\pi/R$, inversely proportional to membrane curvature, as seen in Fig. 4.3) and normalized expansive force for the systems previously shown in Fig. 4.2(A) and 4.1 (B and C, respectively) in the absence of depolymerisation, addition of filaments, addition and removal of cross-linkers. Forces are shown in solid lines, length in dashed ones. Negative forces indicate net contractility; the system (A) starts with a strong contractile behaviour, the system (B) starts with an expansive behaviour and the system (C) starts with an even stronger contractile behaviour. All forces decay towards zero. Forces and lengths were normalized to make the strongest and longest 1 in magnitude. Unless otherwise noted, this will be the usual normalization done for most plots.

decreased. Similarly to the previous example, the net force eventually decays to zero upon system expansion, due to the restoring force from the membrane being bent outside its preferred curvature.

Finally, we can study system (C) under the same conditions and see how the existence of two clusters of filaments in parallel affects the forces in the system. We see the results in Fig. 4.4. It is not surprising that the behaviour is similar to system (A): an initial contractile force shrinks the system size L until that force decays to zero. Since the forces are normalized, we do not see here that the initial force is, effectively, twice as strong as the one from system (A), which explains why the system shrinks faster and reaches zero net force faster. We can also see that the final membrane curvature is the same as in system (A).

Next, we can see the influence of depolymerisation dynamics in the contractile potential of these systems. We will repeat the same simulation already presented for these 3 systems, but introducing a depolymerisation rate of 1 monomer per end per simulation time step (unless otherwise noted, this rate will be maintained for the whole chapter). We present these results for systems (A), (B) and (C) (in this order) in Fig. 4.5.

We see that the general behaviour for those three systems is very similar now. The system contracts in a linear fashion in time, reflecting the linear force-velocity relationship we have established for this system, which agrees with the fact that force is approximately constant during this process. The linear coefficient relating these two quantities will change from system to system, given that this depends on the number of cross-linkers in the system. This can be seen from the plots easily: even if the system (C) has twice is much contractile force as (A) (as we will see later), it takes longer than half the time to achieve a stalling point.

Another detail that is different between the systems is the initial forces: we can see that (A) and (C) start with a positive contractile force, while (B) seems to start at a negative one and only achieve constriction after some time steps. This is in agreement with our previous simulations: system (B) only becomes contractile after some depolymerisation confines the cross-linkers to shorter overlap regions. Finally, different simulations stall at different points in time, with different final membrane curvatures. This happens because depoly-

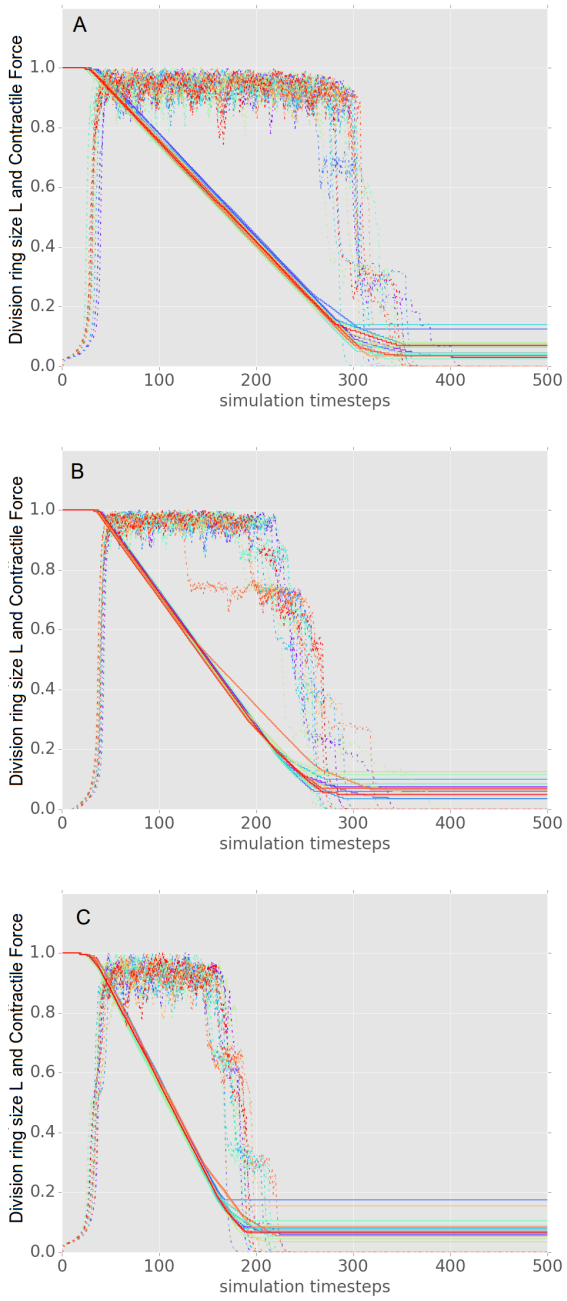

Figure 4.5: Normalized turn length (i.e. system size $L = 2\pi/R$, inversely proportional to membrane curvature, as seen in Fig. 4.1) and normalized contractile force for the systems shown in Fig. 4.2 and 4.3, when depolymerisation dynamics are introduced. Forces are shown in dashed lines, length in solid ones. Positive forces indicate net contractility; the systems contract until a "jammed" state. Figure shows the results of 16 simulations, with forces averaged with exponential weights over a span of 1 simulation timestep.

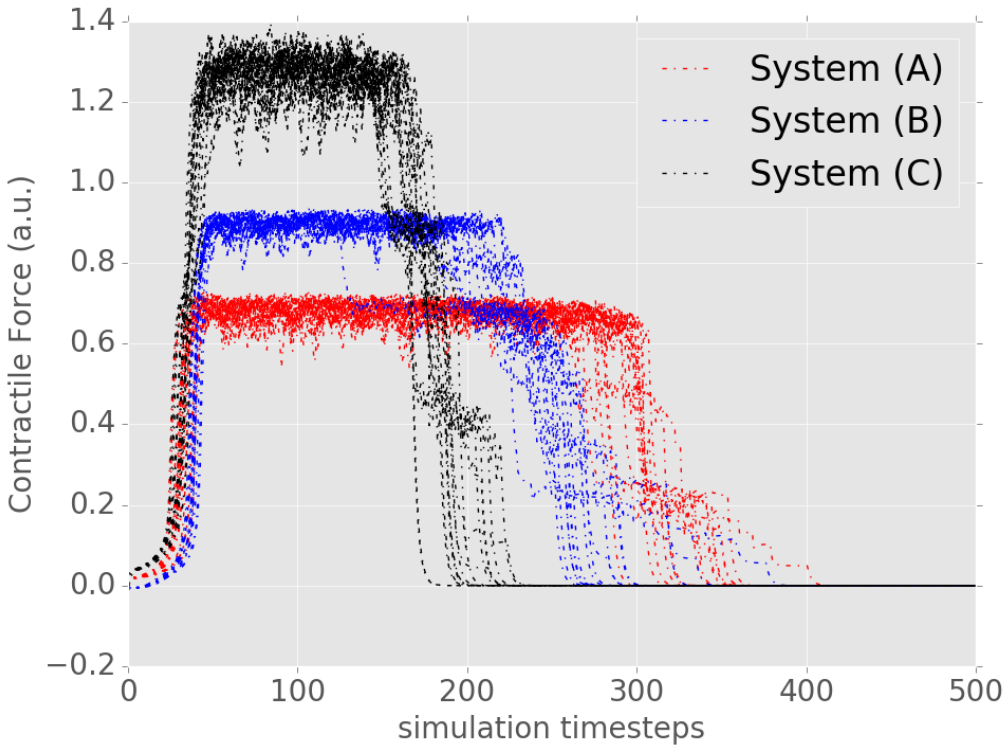

Figure 4.6: Forces for the three systems, in a single plot. As mentioned, contractility increases from system (A) to (B), and from (B) to (C), and force in system (C) is twice as strong as in system (A).

merisation is a stochastic process. Different simulations will result in different filament sizes, leading to "jammed" configurations at different points in time.

We can also compare the magnitude of the forces in the three systems. As mentioned, the forces increase from system (A) to (B) and from (B) to (C). We can see that in Fig. 4.6. All the features from the previous plots are still there, and it is easier to compare them to each other here. Interestingly, we can note that the force generated by system (C) is roughly twice as strong as the one from system (A): therefore, force generation scales linearly with the number of parallel clusters present in the system.

We have posited that percolation is necessary for force generation; we have not shown that to be true yet. Here, we will define a percolating cluster as a group of filaments connected by cross-linkers where, starting from one

filament, it is possible to traverse to other filaments in the cluster by following cross-linkers and arrive at the initial one again by using each lateral overlap region not more than once, and traversing one turn length. All our systems (A), (B) and each of the two clusters in system (C) are percolating, given this definition.

Following that postulate, the removal of any single cross-linker in systems (A) and (B) and a cross-linker from each cluster in system (C) should render these systems completely incapable of generating constriction. As we can see on Fig. 4.7, this is true for system (A). This situation presents a very weak expansive behaviour. The force magnitudes are small and this effect should not be relevant *in vivo*. This is also true for the other two systems, with very similar results that are not shown here. The fact that removing a single cross-linker makes constriction impossible is consistent with our assertion that contractility requires percolation.

We have seen that the structure of the percolating clusters and the number of these in a system affect the forces being generated in these systems. Finally, we want to investigate how the depolymerisation rates affect the contractile potential of systems. For that, we use system (A) and vary the depolymerisation rate per end per simulation time step. The results are in Fig. 4.8. We plot the depolymerisation rates versus the final equilibrium length L for the system; high equilibrium lengths indicate low equilibrium membrane curvature, and therefore low contractility. We see that very low depolymerisation rates indicate very low contractile rates, but the equilibrium length very quickly decreases and reaches a plateau, where systems are completely "jammed".

4.3.2 Percolation is necessary but not sufficient for constriction

In the previous section, we have shown that the presence of a percolating cluster of filaments is necessary to generate contractile forces. In this section we will show that, while that is a necessary condition, it is sufficient.

In fact, we have seen in system (B) from the previous section that, in the absence of depolymerisation dynamics, there was no contractility even

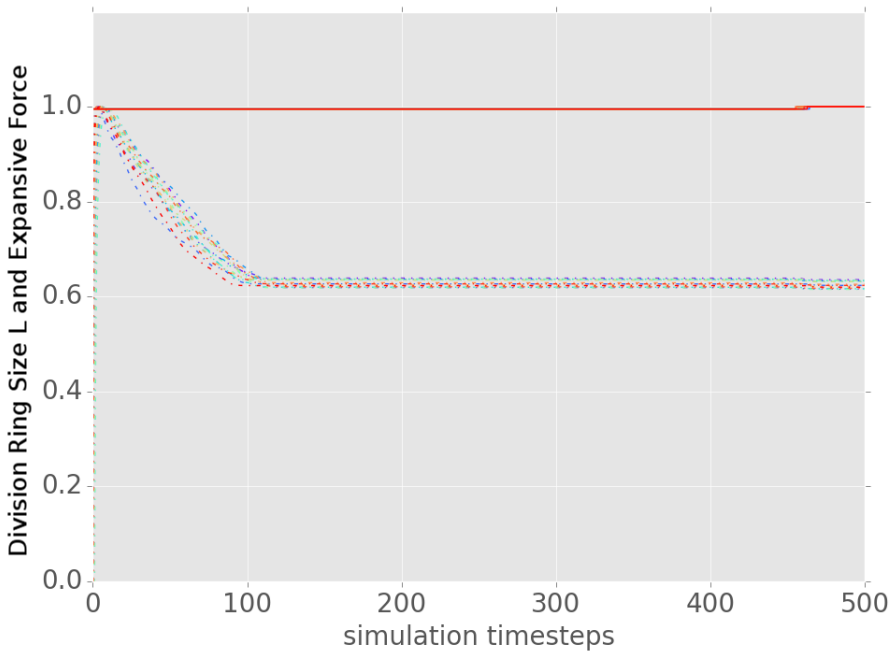

Figure 4.7: Normalized turn length (i.e. system size L, inversely proportional to membrane curvature) and normalized expansive force for the system with three filaments and only two cross-linkers, with depolymerisation dynamics. Forces are shown in dashed lines, length in solid ones. Positive forces indicate net expansion; there is absolutely no contracility and the system expands indefinitely.

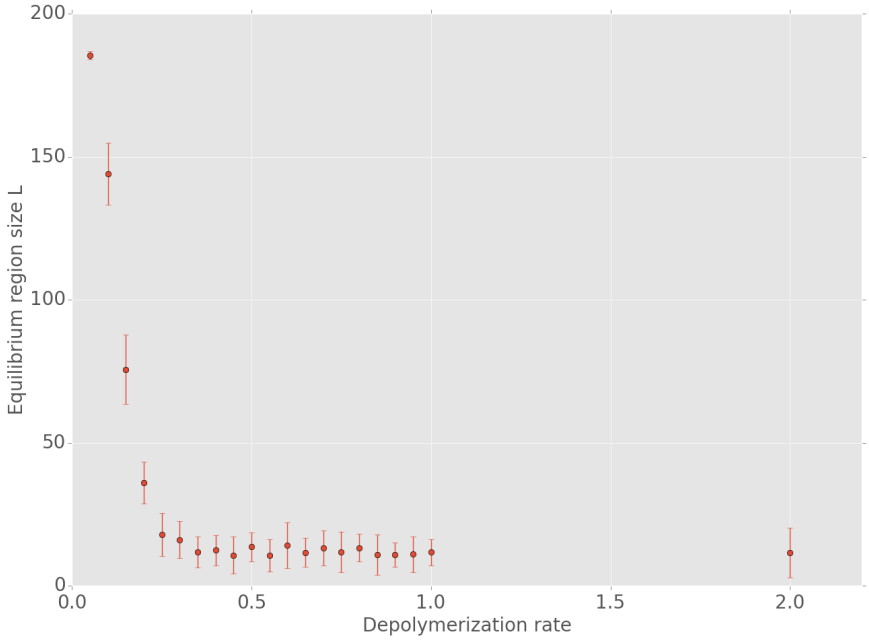

Figure 4.8: Equilibrium lengths L *versus* depolymerisation rates for system (A). High equilibrium lengths indicate low contractile forces. Increasing depolymerisation rates indicate increasing contraction up to the "jammed" state, where the equilibrium lengths reach a plateau.

though that was a percolating cluster of filaments. The results can be seen on Fig. 4.5, and have been already discussed.

Furthermore, we can show that, even in the presence of all the dynamics we propose for this model, it is still possible to achieve situations where percolating clusters are insufficient to generate a net contractile force. Here, we initialise a system with no filaments nor cross-linkers and allow for addition of polymers, depolymerisation, addition and removal of cross-linkers, contraction and expansion. Unless otherwise noted, we will use $k_{on} = 0.1$ filament per empty space per simulation time step, $k_{bind} = 0.01$ cross-linker per lateral overlap site per simulation time step and $kunbind = 0.01$ cross-linker per simulation time step and a region of interest with 5 turn lengths of size 50 for the remainder of this chapter.

In Fig. 4.9, we can see the results of 16 simulations of this system. We see that there are many situations where a percolating cluster is formed, but only a few where a net contractile force is achieved; from those, only one achieves such a result over an extended amount of time.

Therefore, even in situations where depolymerisation is happening (and, therefore, lateral overlap regions are shrinking), not every percolating cluster will be enough for the system to achieve net contraction. It can be postulated that a larger number of filaments in the system make it less likely to be contractile; we have seen that this was the case in the previous section when comparing systems (A) and (B), and filaments that are not part of the percolating cluster will be an even bigger obstacle to net contractility due to the increased translational freedom they would have available in the case of an expansion event.

4.3.3 Generating contractile bundles

We have established that the first step towards creating contractility in bundles of filaments with diffusible cross-linkers is to have percolation. Previously, we have constructed percolating systems by hand and analysed their behaviour; in this section, we study whether it is possible to create such structures from more realistic *in vivo* dynamics.

Therefore, we develop simulations where we start from an empty sys-

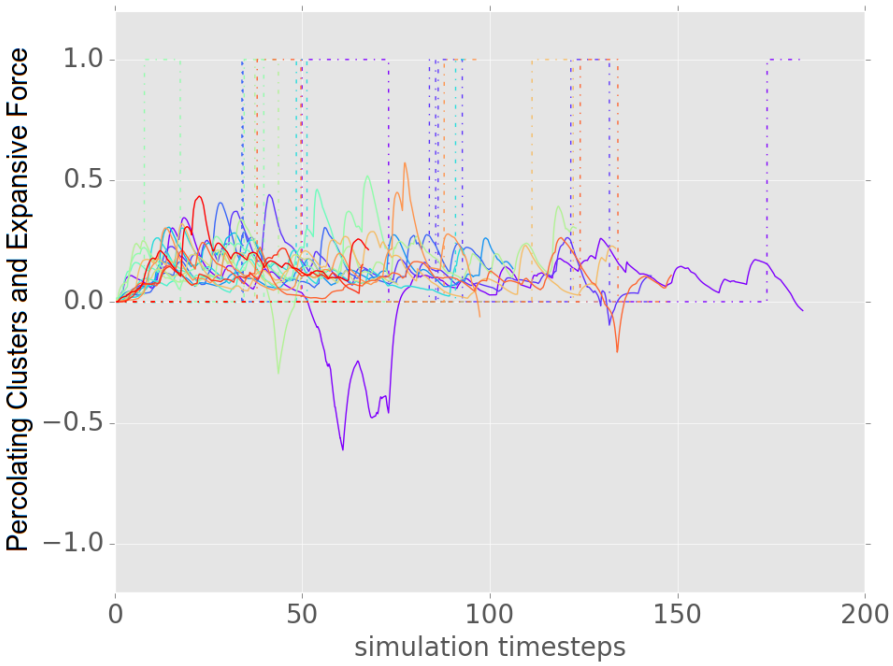

Figure 4.9: Number of percolating clusters (in dashed lines) and expansive forces (in arbitrary units) for 16 realizations of a system that starts empty and incorporates all dynamics that have been presented: addition of polymers, depolymerisation, addition and removal of cross-linkers. Negative forces indicate contraction.

tem, without any filaments or cross-linkers present, and allow the addition of filaments dynamically, in addition to maintaining the kinetics of depolymerisation, binding and unbinding of cross-linkers. This way, the creation of filament bundles will be completely driven by the stochasticity in the model.

Initially, we investigate the possibility of genertating contractile bundles from these dynamics without any time-dependent change on parameters. In this case, all the kinetic constants are invariant in time. We have tested a range of values for the parameters k_{off} and E_{stick}. These parameters were chosen due to their ability to control polymerisation/depolymerisation mechanics and cross-linking, respectively. Then, we are able to have a simple picture of which regimes for those dynamics can generate percolation and, therefore, potential contraction.

Our results show that, for large depolymerisation rates, percolation rates are very close to zero; these regimes are not conducive to percolation, with filaments shrinking quickly and not persisting for long enough to create large-scale structures.

The low depolymerisation, low cross-linker energy regime seems to be the most conducive to percolation. However, some simulations with high cross-linker energy and low depolymerisation seemed to achieve some high percolation rates, albeit not consistently. This can be explained by positing that some of the realizations in this regime had filaments arranged in a percolating cluster, that would then be very stable due to the high cross-linker energy, achieving a percolation rate close to 1. Other realizations, however, would not have the same fortune, and the non-percolating structures would be also very stable and suffer very low turnover, with a percolation rate close to zero.

As we have already established, percolation does not necessarily translate to constriction. We also examine the average force per timestep. Systems where contraction happens would be likely to have lower forces on average. We can see the results on Fig. 4.10. These results generally agree with the previous ones; low cross-linker energy regimes are the most likely to contract, with low depolymerisation ones being particularly suited. Note that all systems, however, have positive average expansive forces, indicating that either percolating clusters are still relatively rare or the entropic forces from non-percolating structures are stronger than the contractile effects.

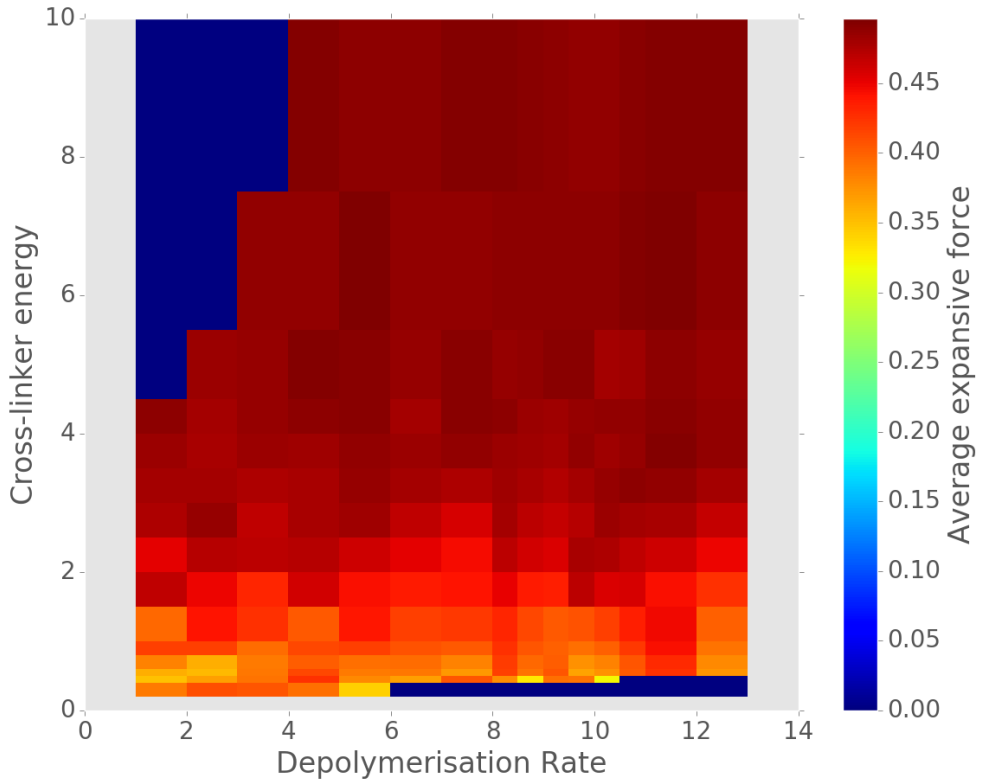

Figure 4.10: Heat map for average expansive forces for values of depolymerisation rate and cross-linker energy. These are the values for the expansive force (defined as positive) on average of each time step, over 16 realizations. Lower expansive forces indicate a higher likelihood to contract; zero-value forces indicate lack of data. Cubic interpolation was used for obtaining values in data gaps.

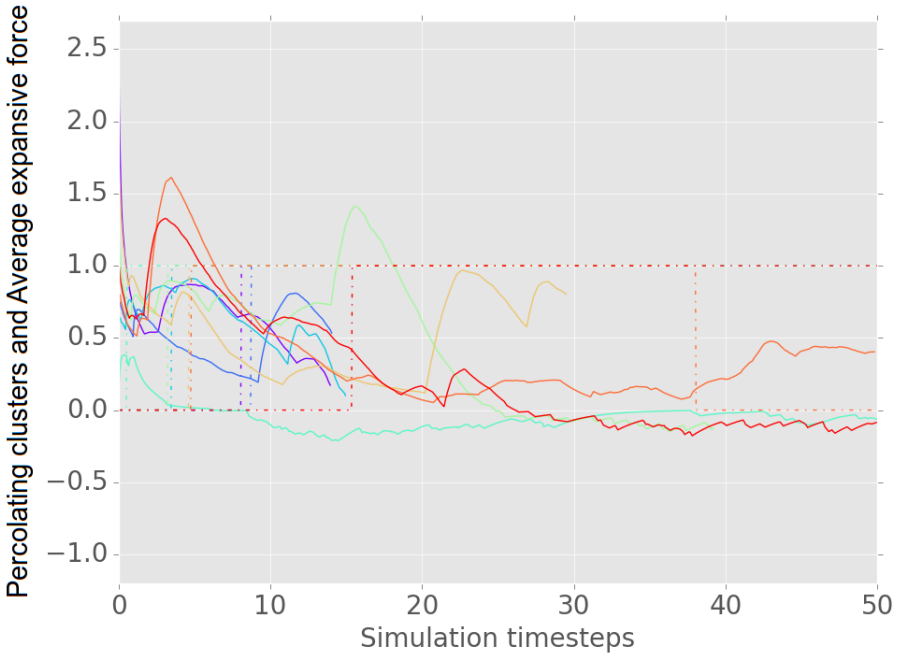

Figure 4.11: Number of percolating clusters (in dashed lines) and expansive forces (in arbitrary units) for 8 realizations of high-percolation rate systems, with low depolymerisation rates, low cross-linker energies, high polymerisation and cross-linking rates. Negative forces indicate contraction.

We will, therefore, focus on the systems where we can find percolating clusters more often: low depolymerisation, low cross-linker energy ones. These are systems where filaments have a relatively long persistence time, but that can remodel often due to the relatively weak cross-linking. In fact, by increasing filament creation and cross-linking rates, we were able to achieve 60-70% percolation rates; we plot 8 realizations of such systems in Fig. 4.11.

These systems, however, reach a "jammed" limit - they will reach percolation through having a very high density of filaments and cross-linkers, as it can be deduced by the rates and energies being used to generate them. Then, these percolating systems are not very successful at generating constriction, since the contractile force that the percolating cluster can generate is counteracted by the entropic forces from all the other filaments and cross-linkers, which are expansive in nature.

Another problem from "jammed" systems can be seen in Fig. 4.11 - not

many time steps could be simulated. These systems have many filaments and cross-linkers, which means many constraints, and Barvinok's algorithm can become extremely slow when calculating the number of microstates in these situations. Therefore, for these systems in specific we will take an approximate approach to calculating the entropy changes in the system. Instead of using the exact values for the number of integer points given by Barvinok's algorithm, we will approximate that number by the approximate volume of the polytope defined by the constraints, calculated by the Polyvest algorithm [Ge and Ma, 2015].

Therefore, if we want to generate contractility in these systems, it is necessary to move them away from these states. We have, then, tried to increase the depolymerisation rate three-fold after percolation occurs. We have implemented a routine for detecting percolating clusters to trigger such a change, and when such event happens we manually modify the depolymerisation rate.

With that system in place, we will both decrease the number of other filaments and cross-linkers and push the percolating bundle towards contraction. This is one way that a contractile system might be engineered *in vivo*. We can see the behaviour of these systems in Fig. 4.12.

Most of the realizations achieve constriction at some point and that the depolymerisation scheme was necessary for such result - however, constriction is not very stable, due to the weak nature of the cross-linkers. In Fig. 4.13, we focus on the initial timesteps of these realizations, so we can see where most of them achieve constriction.

Over the first 40 time steps, most of the realizations follow a similar path - there is an initial expansive force that, upon percolation and change in depolymerisation rates, dips significantly (especially noticeable between timesteps 10 and 25). For some of those realizations, this dip takes them into contractile forces, where for others it is only enough to decrease expansion. Then, the stability of the percolating cluster is disrupted, and expansion increases again.

An alternative way of looking at these systems is tracking the system size. For this simulation, we have capped the maximum system size to 1.2 times the initial size, to mimic the effects of an external cell wall and stop the system from ballooning in size. We can see the results in Fig. 4.14. We can see

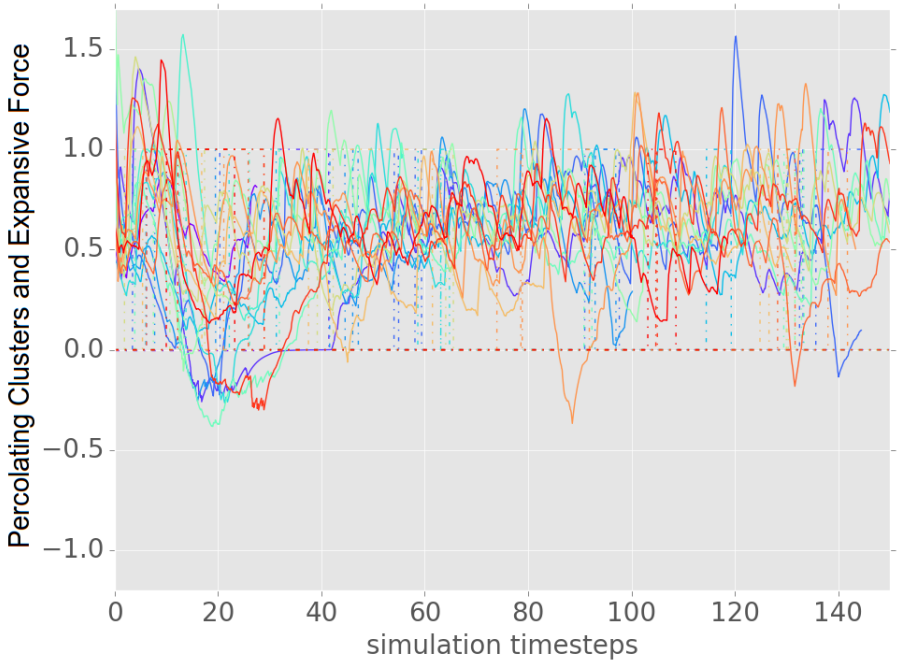

Figure 4.12: Number of percolating clusters (in dashed lines) and expansive forces (in arbitrary units) for 16 realizations of depolymerisation-switched systems, with low depolymerisation rates, low cross-linker energies, high polymerisation and cross-linking rates and increasing depolymerisation rates after percolation. Negative forces (in arbitrary units) indicate contraction.

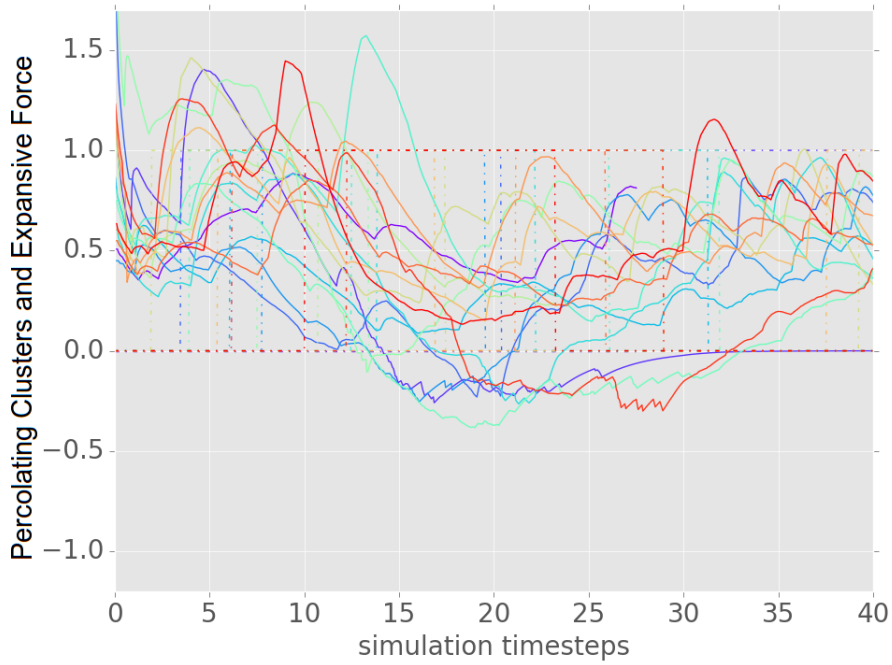

Figure 4.13: Number of percolating clusters (in dashed lines) and expansive forces (in arbitrary units) for the initial timesteps of 16 realizations of depolymerisation-switched systems, with low depolymerisation rates, low cross-linker energies, high polymerisation and cross-linking rates and increasing depolymerisation rates after percolation. Negative forces (in arbitrary units) indicate contraction.

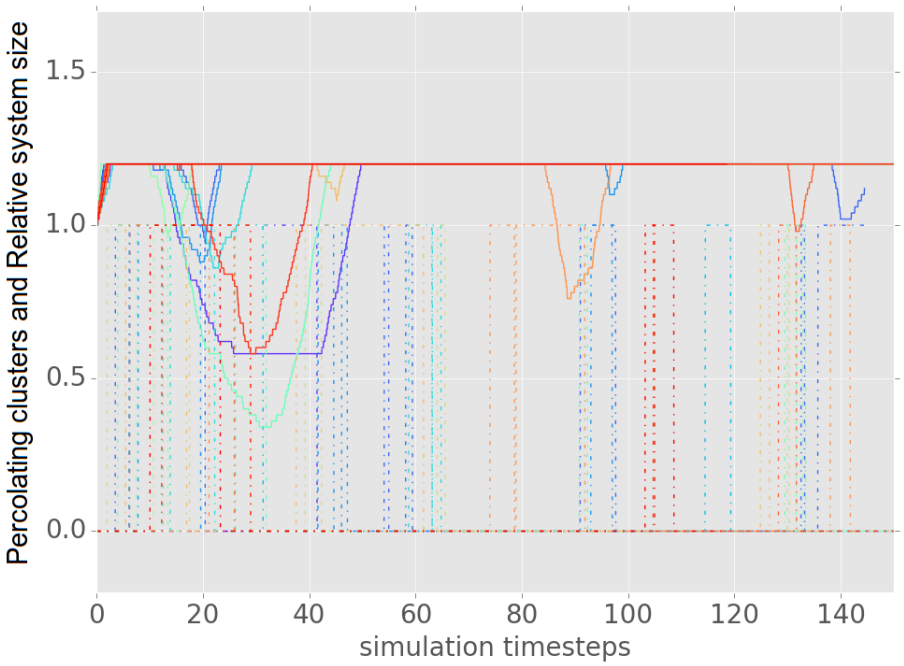

Figure 4.14: Number of percolating clusters (in dashed lines) and relative system size (as fraction of initial size) for 16 realizations of depolymerisation-switched systems, with low depolymerisation rates, low cross-linker energies, high polymerisation and cross-linking rates and increasing depolymerisation rates after percolation.

that all systems initially increase to the maximum cap due to the expansive forces, and most of them go through at least one cycle of contraction, with variable extents in size and time scales.

4.4 Discussion

4.4.1 The presence of diffusible cross-linkers in bundles can generate contraction

In this chapter, we extended the work presented in chapter 3 from single filaments to bundles of cross-linked filaments. The central result here is that, similarly to the systems with only one filament, the presence of diffusible cross-linkers can also create a net contractile force in bundles of filaments. There,

any cross-linker would be enough to create a contractile force that would need to be countered by restoring forces due to filament rigidity; here, the conditions for generating constriction are much more strict.

We have constructed some simple systems with multi-filament bundles and studied their behaviour. In the absence of dynamics, two of the three systems with percolating bundles have presented contractility; however, contraction was quickly stalled due to the decreasing forces after the expansion of lateral overlap regions and increased restoring force from the Hamiltonian that models bending rigidities.

When depolymerisation dynamics were introduced, all three systems presented constriction. All of them contracted until a "jammed" state, where further depolymerisation is impossible, though at different rates. We show that the forces generated at each system increase from (A) to (B) to (C), with the force at system (C) (consisting of two three-filament clusters in parallel) was roughly twice as strong as the one at system (A) (with only one three-filament cluster), indicating that percolating clusters in parallel contribute to the net force additively.

Finally, we show that the percolating aspect of these bundles is essential to generating contractile forces. We repeat the previous simulations on all three systems without one of the cross-linkers (in the case of system (C), one cross-linker removed from each cluster). By removing a single cross-linker, these systems go from presenting significant contractility to expanding very weakly, which shows that non-percolating clusters will not generate any constriction at all.

4.4.2 Percolation does not guarantee constriction

Following the previous section, we have decided to investigate whether the existence of a percolating cluster was sufficient to generate a net contractile force. In fact, we had already seen that would not be the case when simulating system (B); in that case, net constriction is only achieved through depolymerisation dynamics.

To study the generality of this assertion, we generated simulations of systems where all dynamics of interest are active (polymer addition, depoly-

merisation, cross-linking, removal of cross-linkers, contraction and expansion). Also in this case, we see that many instances in which percolating clusters emerge are not contractile at all. Especially in the case of short-lived clusters, they do not seem to be able to overcome the entropic forces due to all the other "free" polymers and cause net contraction. In the specific case simulated by us, only in one of the 16 runs we achieved to establish a cluster for long enough to generate sustained contraction over many simulation time steps. If bundling agents (i.e. cross-linkers) act to stabilise filaments, a situation where non-percolating structures depolymerise faster than contractile ones could mitigate this issue.

4.4.3 Dynamics alone are not enough for reliable constriction

We generate percolating clusters starting from an empty system with no filaments or cross-linkers. We populate filaments via polymerisation and introduce cross-linking kinetics. We started by studying the effect of the parameters k_{off} and E_{stick} in systems where no parameters changed in time, finding that low depolymerisation and low cross-linking energies led to more percolation and contractility.

Next, we have optimized all the parameters for maximum generation of percolating bundles, arriving at low depolymerisation rates, low cross-linker energies, high polymerisation and cross-linking rates. These systems were able to achieve 60-70% percolation rates, although they ended up in "jammed" configurations, where the slow depolymerisation of the non-percolating structures led to a net expansive force.

Finally, we examined whether it is possible to achieve sustained contraction by increasing depolymerisation rates upon the onset of percolation. In this situation, most realizations had at least one cycle of contractile behaviour, with the extent of contractility, both in time and space, being variable.

Thus, it is definitely possible to generate contracting bundles of filaments from this system. However, the transient nature of the contractility in this model contrasts with the sustained contracting behaviour that happens *in vivo*. It is not clear whether this is an effect from the small system size or

an intrinsic feature of this model. While we have shown that entropic forces generated by cross-linkers are at scales that render them biologically relevant, it is unlikely that the dynamics outlined here capture completely the force generation responsible for cytokinesis during bacterial division.

It is important to notice, however, that living cells are more complex than this model. Importantly, evidence for a polar nature of FtsZ filaments has been shown recently, with treadmilling being observed *in vivo* [Bisson Filho et al., 2016]. Directional movement of filaments would lead to an intrinsically different paradigm for studying force generation during bacterial division.

Chapter 5

Experimental Work

As part of this Ph.D. project and according to the EU guidelines for the Marie Curie Innovative Doctoral Programs, an international secondment was to be undertaken at an academic partner outside the UK.

For this project, the chosen partner was Duke University, with a visiting position at Prof. Harold Erickson's laboratory, part of the Cell Biology department. This secondment took part between October 2014 and March 2015, for a total of six months, during which the main focus was to learn laboratory techniques and develop fluorescence assays and experiments to investigate the assembly of FtsZ mutant ftsZ84 (G105S).

5.1 Motivation

Studies of temperature-sensitive mutant ftsZ84(Ts) have given us crucial information regarding of FtsZ localization during the proper functioning of cell division. Strains containing the aforementioned mutation fail to divide when under nonpermissive conditions (42°), and exhibits a failure to localise [Addinall and Lutkenhaus, 1996].

It has been shown [Addinall et al., 1997] that switching the ftsZ84(Ts) strains from permissive (30°) to nonpermissive conditions (42°) brings the formation of long, filamentous cells lacking any Z rings, due to failed localization of FtsZ. Furthermore, it has been demonstrated that mildly overexpressing ftsZ84 provides complementation (i.e. normal cell function in the absence of wild-type protein), and the lethal cell division defect is thus rescued [Phoenix

and Drapeau, 1988].

Our understanding of FtsZ function has been greatly advanced by studying this mutant. As an example, the fact that ftsZ84 has a significantly reduced GTPase activity *in vitro* [de Boer et al., 1992; RayChaudhuri and Park, 1992] with a much less dynamic Z ring in vivo [Stricker et al., 2002], but can still have fundamentally normal cell division at the permissive conditions [Addinall et al., 1997] shows us that the high GTPase activity of the wild-type protein [de Boer et al., 1992; RayChaudhuri and Park, 1992] is not really essential for its in vivo function [Lu et al., 2001].

Despite the measured GTPase activity and the complementation studies showing normal cell cycle time at permissive temperature, only sedimentation studies seem to show any degree of assembly for the ftsZ84 mutant [Bramhill and Thompson, 1994]. Moreover, no apparent temperature dependence seems to exist for the activity *in vitro*, and there is evidence showing this mutant to have some degree of ATPase activity [RayChaudhuri and Park, 1994].

Therefore, the aim of this work is to probe ftsZ84 assembly through a variety of means. First of all, following the previous work done by Chen et al. [Chen and Erickson, 2011], mutations introducing tryptophan were to be performed on ftsZ84 DNA. Assembly could, then, be reported through a change in fluorescence when adding GTP to the protein. The specific mutations chosen for this work were previously reported [Chen and Erickson, 2011] as successful cases of FtsZ mutations where assembly could be probed using tryptophan fluorescence as a proxy measure.

In addition to that, electron microscopy was to be performed on the Z84 mutant under assembly conditions. Finally, we have decided to replicate the previous work on the GTPase activity of this mutant, looking into concentration and temperature dependence.

Five mutants were studied in this work, all on *E. coli* FtsZ: the original ftsZ84 mutation (G105S) and four further mutations added to the G105S background: L68W, Y222W, L189W and T151C/Y222W. All mutants except for the latter were checked through tryptophan fluorescence, while the very last one was labelled with a fluorescent dye and the fluorescence change measured at the fluorophore's wavelength, with the tryptophan acting as quencher.

We will henceforth refer to these mutants by adding the designation

"/84" to their original name: L68W/84, Y222W/84 and so on. This is to clarify that the referred mutations were added to the ftsZ84 protein, and not to wild-type.

5.2 Experimental Procedures

All studies were done with *E. coli* FtsZ. Mutants of FtsZ were constructed using site- directed mutagenesis in the plasmid pET11b-FtsZ, using the tryptophan mutants' DNA as a template. FtsZ proteins were expressed and purified as described previously [Chen et al., 2005; Chen and Erickson, 2005]. Briefly, the soluble bacterially expressed protein was purified by 15% ammonium sulfate precipitation, followed by chromatography on a source Q 10/10 column (GE Healthcare) with a linear gradient of 50-500 mM KCl in 50 mM Tris, pH 7.9, 1 mM EDTA, 10% glycerol. Peak fractions were identified by SDS-PAGE and stored at $-80\,^{\circ}$C.

The FtsZ mutant T151C/ Y222W was labelled with BODIPY FL N-(2-aminoethyl) maleimide (BODIPYaem; Molecular Probes) before use. Briefly, a 5-fold molar excess of dye was incubated with FtsZ protein at room temperature for 2 hours. After adding 1 mM DTT, free dye was removed through dialysis. The labelling efficiency was around 10%, so the protein could be used without any further dilution. Labelled protein was stored at $-80\,^{\circ}$C.

Most experiments were done in HMK buffer (50 mM HEPES pH 7.7, 5 mM MgAc, 100 mM KAc), and assembly was initiated by adding 0.5 mM GTP. The protein concentration was determined using a BCA assay and corrected for the 75% color ratio of FtsZ/BSA, as described previously [Lu et al., 1998], or by measuring the protein's absorbance at 280nm and using the mutant's extinction coefficient, given that all mutants have tryptophans.

GTPase activity was measured using a continuous, regenerative coupled GTPase assay [Ingerman and Nunnari, 2005]. In this assay, all free GDP in solution is rapidly regenerated into GTP, in a reaction that consumes one NADH per GDP. The GTP hydrolysis rate is measured by the decrease in absorption of NADH, in a Shimadzu UV-2401PC spectrophotometer, using the extinction coefficient 0.00622 $\mu M^{-1} cm^{-1}$ at 340 nm. Our assay mixture included 1 mM phosphoenolpyruvate, 0.8 mM NADH, 20 units/ml pyruvate

kinase and lactate dehydrogenase (Sigma-Aldrich), and 0.5 mM GTP. A 3-mm path cuvette was used for measurement. Hydrolysis was plotted as a function of FtsZ concentration. Measurements were made in a thermostatically controlled cell at 25 °C, except where otherwise noted.

Fluorescence measurements were made with a Shimadzu RF-5301 PC spectrofluorometer. FtsZ assembly kinetics were measured following addition of GTP to 0.5 mM. All fluorescence measurements were taken in a thermostatically controlled cell at 25 °C, unless otherwise noted. For most tryptophan mutants, tryptophan emission spectra were measured between 300 nm to 420 nm, with excitation at 295 nm. Assembly kinetics were monitored by measuring the tryptophan emission at 340 or 350 nm, with excitation at 295 nm.

Some fluorophores can be efficiently quenched by a tryptophan that is close enough to form van der Waals contacts and perhaps ring stacking. We added the Z84 mutation to FtsZ double mutant T151C/Y222W, in which cysteine is close to the tryptophan (10 Å between the alpha carbons). A similar construct has been shown strong tryptophan-induced quenching of the fluorophore, with quenching being reduced upon assembly. [Chen and Erickson, 2011] BODIPY fluorescence spectra were measured between 500 nm and 600 nm with excitation at 490 nm, and assembly kinetics were measured at the peak 515 nm, with excitation at 490 nm. All measurements were taken at 25 °C, unless otherwise noted.

FtsZ filaments were imaged by negative stain electron microscopy (EM). Approximately 10 μL of sample in the appropriate buffer was incubated with GTP for 1-2 min and applied to a carbon-coated copper grid. Samples then were negatively stained with 2% uranyl acetate and photographed using a Philips 301 electron microscope at various magnifications.

Unless otherwise noted, all variability between experiments comes from technical replicates.

5.3 Fluorescence Assays

Preliminary work showed no signal change for the mutants L68W/84, Y222W/84 and L189W/84, which indicates that no assembly occurred. Therefore, our main focus will be on T151C/Y222W/84, our mutant labelled with BODIPY.

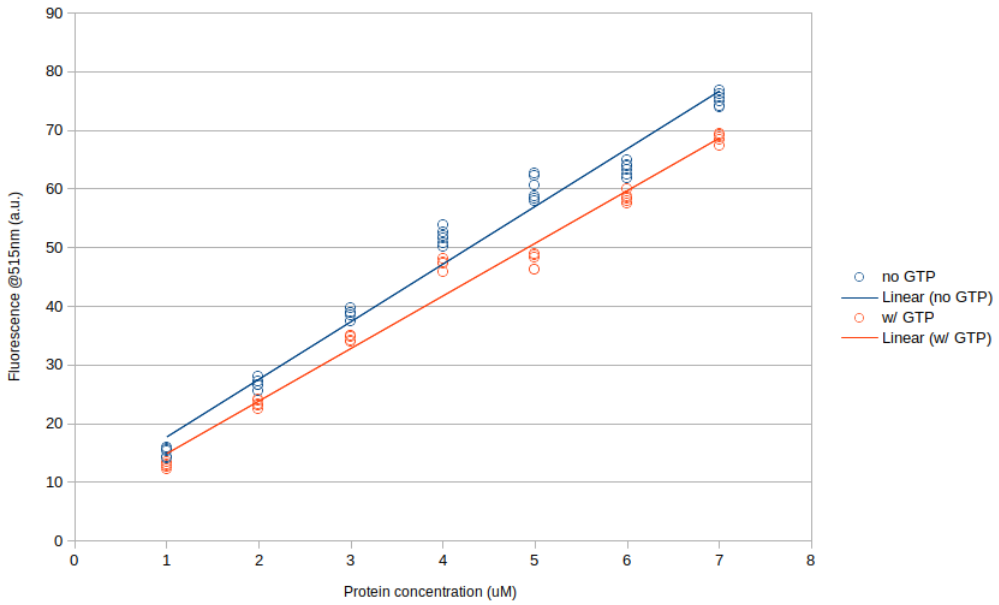

Figure 5.1: Fluorescence for different concentrations of the FtsZ mutant T151C/Y222W/84 at 515 nm when excited at 490 nm, with and without nucleotide. Measurements with GTP were taken after addition of 0.5 mM GTP.

For this mutant, it was necessary, before anything else, to check whether the addition of GTP caused any change in fluorescence for the protein. We have found that, albeit small, there was a consistent decrease in total fluorescence for all concentrations on addition of 0.5mM GTP, as see on Fig. 5.1. For comparison, we plot the observed spectra for the T151C/Y222W mutant without the Z84 mutation as published by Chen and Erickson [Chen and Erickson, 2011] as Fig. 5.2.

It is not clear, however, whether the source of this fluorescence decrease is due to protein assembly. To rule out any other reason such as GTP absorbance, a different assay was done. This time, a small concentration of the BODIPY-labelled mutant (0.5 μM) was introduced; this should be below the critical concentration and, therefore, should not assemble by itself. Then, an

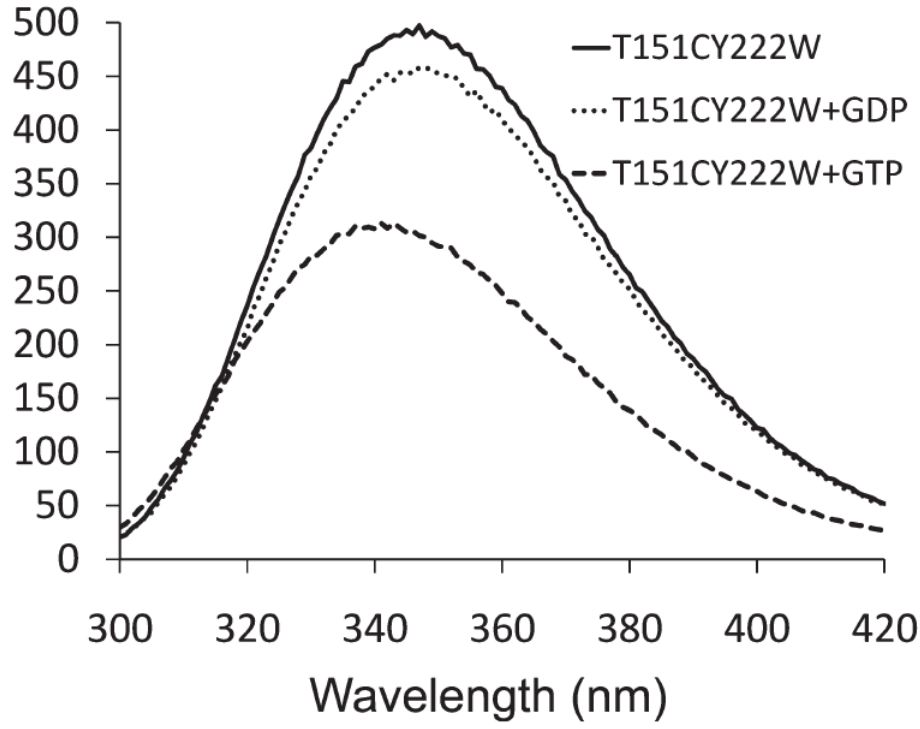

Figure 5.2: Emission spectra for the FtsZ mutant T151C/Y222W as presented by Chen and Erickson [Chen and Erickson, 2011]. mutant protein was diluted to 5 M concentration and excited at 295 nm, and the emission spectrum was recorded with no addition and with 1/20 volume of GDP or GTP (to 0.2 mM final concentration). Spectra were recorded after 1 min to achieve steady state.

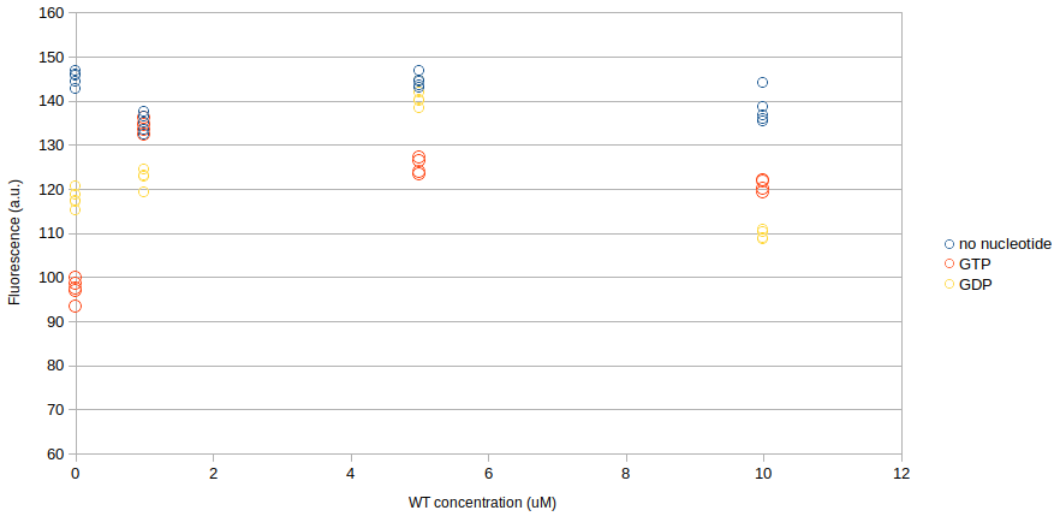

Figure 5.3: Fluorescence for different concentrations of wild-type FtsZ added to 0.5 μM FtsZ mutant T151C/Y222W/84 at 515 nm when excited at 490 nm, with and without nucleotides. Measurements with GTP were taken after addition of 0.5 mM GTP, and measurements with GDP were taken after addition of 0.5 mM GDP.

increasing concentration of wild-type protein was to be added. The change in fluorescence should still occur, were it to be due to assembly. Finally, we have also added GDP to the samples: in this case no assembly should occur, but the samples would otherwise be virtually identical to the ones with GTP.

In this case, as shown in Fig. 5.3, results seem to be mixed and inconclusive. As expected, the total fluorescence with no nucleotide was almost constant, with a maximum deviation of about 10%, since the amount of fluorescent protein being added was constant. However, the samples with GTP and GDP changed in a more significant way, but with no apparent trend. Samples with GTP have a considerably smaller fluorescence when no wild-type was added, almost the same as no nucleotide for 1μM wild-type and smaller decrease for higher wild-type concentrations. Samples with GDP started on a relatively low fluorescence (albeit higher than the GTP samples), increased up to 5μM wild-type (where it became almost indistinguishable from the sample with no nucleotide) and then had a sharp decrease for the higher wild-type concentrations.

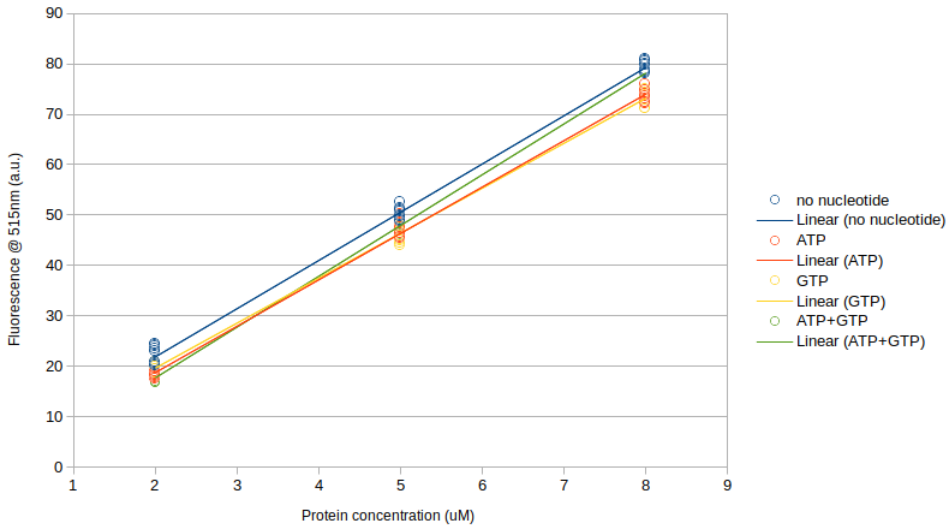

Figure 5.4: Fluorescence for different concentrations of the FtsZ mutant T151C/Y222W/84 at 515 nm when excited at 490 nm, with and without different nucleotides. Measurements with GTP were taken after addition of 0.5 mM GTP, measurements with ATP were taken after addition of 0.5 mM ATP and measurements with both were taken after addition of 0.5 mM ATP and 0.5 mM GTP.

Importantly, there seems to be no trend with regards to GTP or GDP samples having a higher fluorescence. It still is unclear, therefore, whether the decrease in fluorescence seen for most of the samples with any of the nucleotides is anyhow related to actual assembly.

Finally, we have probed the fluorescently-labelled protein for any change in activity on addition of ATP. On Fig. 5.4, we can see it was virtually impossible to differentiate between samples with GTP or ATP. Interestingly, samples with both nucleotides did not present significantly different fluorescence values, as it would be expected were the fluorescence changes to be due to nucleotide absorbance.

5.4 Electron Microscopy

Samples of protein were incubated with GTP and transferred to a carbon-coated grid for electron microscopy. Upon visual inspection, filament forma-

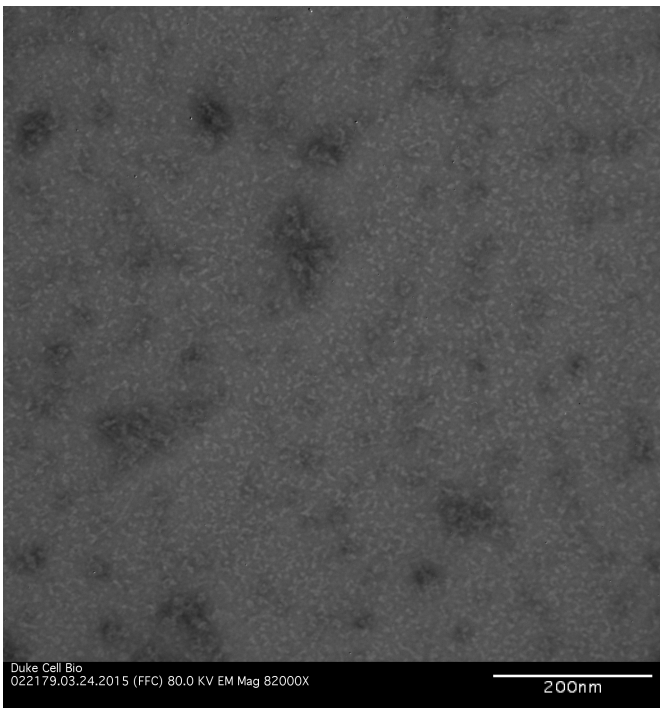

Figure 5.5: Electron micrograph for 10 μM FtsZ mutant T151C/Y222W/84 incubated for 1-2 minutes with 0.5 mM GTP shows no evidence of assembly.

tion could be evident in case of assembly.

First, we have obtained images from our T151C/Y222W/84 mutant, the same one used for most of the fluorescence studies. There were no evidence of assembly for this protein, with or without the addition of the fluorescent BODIPY dye, as seen in Fig. 5.5.

We, then, moved to the ftsZ84 mutant, without any extra mutations, given that no fluorescence was needed for the EM. Here, upon addition of GTP, aggregate structures seemed to appear very sparsely over the grids, as seen in Fig. 5.6. However, the addition of ATP did not seem to yield such results. Finally, by adding a large amount of GTP (5mM instead of the typical 0.5mM) we see the large, fibrous-like aggregates again, as shown in Fig. 5.7.

As a control, images were taken from wild-type protein and shown as Fig. 5.8. As expected, we see a collection of relatively short, individual filaments.

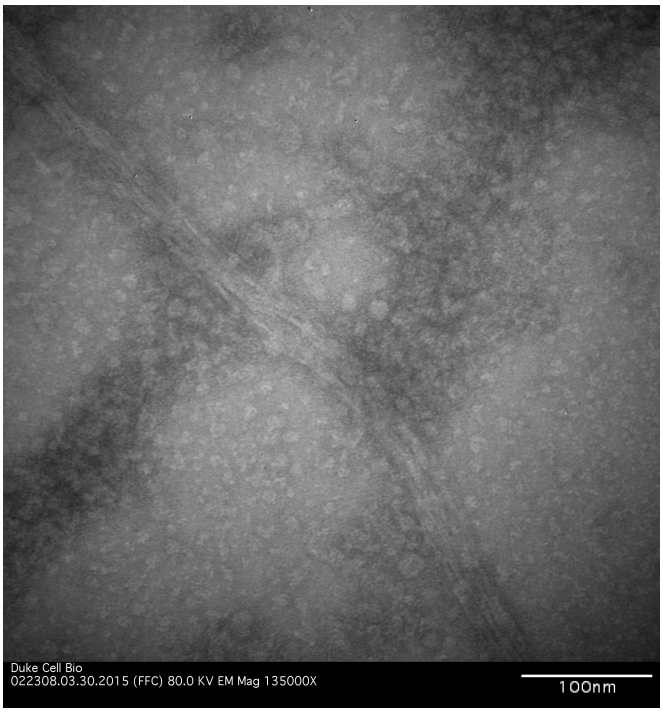

Figure 5.6: Electron micrograph for 10 μM FtsZ mutant Z84 (G105S) incubated for 1-2 minutes with 0.5 mM GTP shows sparse aggregate structures.

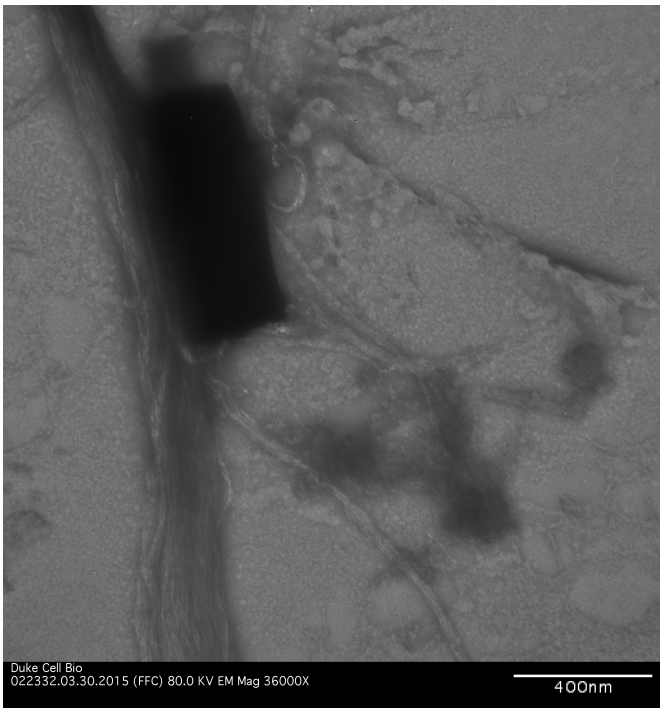

Figure 5.7: Electron micrograph for 10 μM FtsZ mutant Z84 (G105S) incubated for 1-2 minutes with 5 mM GTP shows large, fibrous aggregates.

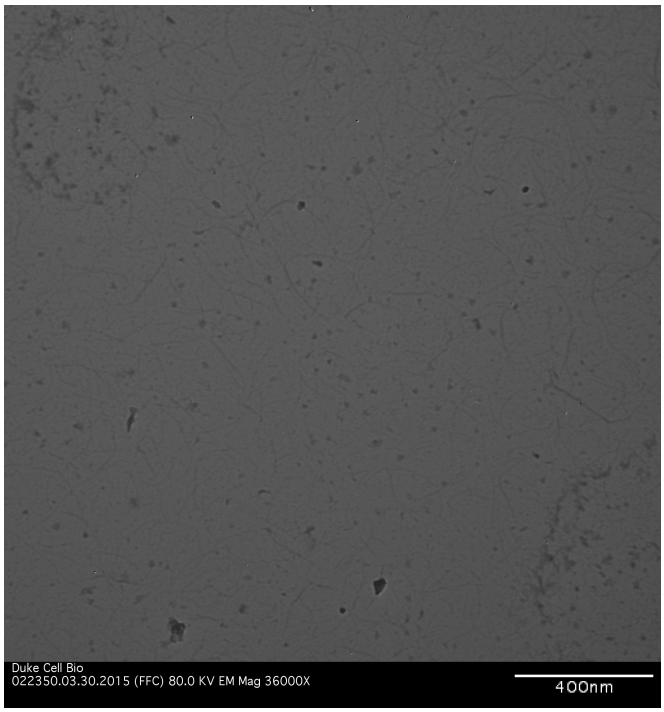

Figure 5.8: Electron micrograph for 10 μM wild-type FtsZ incubated for 1-2 minutes with 0.5 mM GTP shows short, individual filaments as expected.

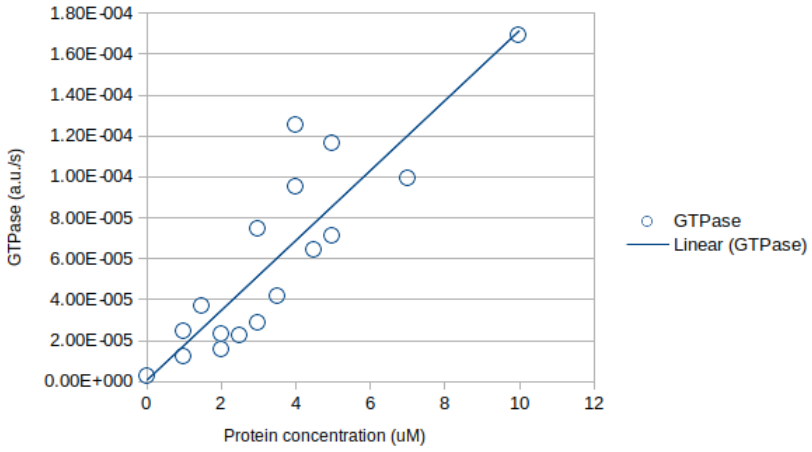

Figure 5.9: GTPase activity measured by proxy NADH absorption at 340 nm for the FtsZ mutant Z84 (G105S) with 0.5 mM GTP using a regenerative coupled GTPase assay.

5.5 GTPase assays

Finally, we use a regenerative assay for measuring GTPase activity on the ftsZ84 mutant. Again, there is no need for fluorescence, so the single mutant is used.

We see that, as expected, GTPase activity increases with concentration, as seen on Fig. 5.9, at a rate of approximately 1.7×10^{-5} arbitrary units per μM. As a comparison, we also measure GTPase activity for the wild-type protein, finding the same expected behaviour as evidenced on Fig. 5.10, with GTPase activity increasing at a rate of approximately 9×10^{-5} arbitrary units per μM. When comparing values, we find that the Z84 mutant tends to be roughly 5 times lower than the wild-type, significantly higher than the 10 times lower most commonly reported on the literature.

Finally, we decide to check on the temperature dependence of GTPase activity values. Here, we repeat the same experiment as before with the Z84 mutant at a constant concentration of 5μM and vary the temperature, with results presented on Fig. 5.11. We find that activity seems to increase with the temperature, going against the previous reports in the literature.

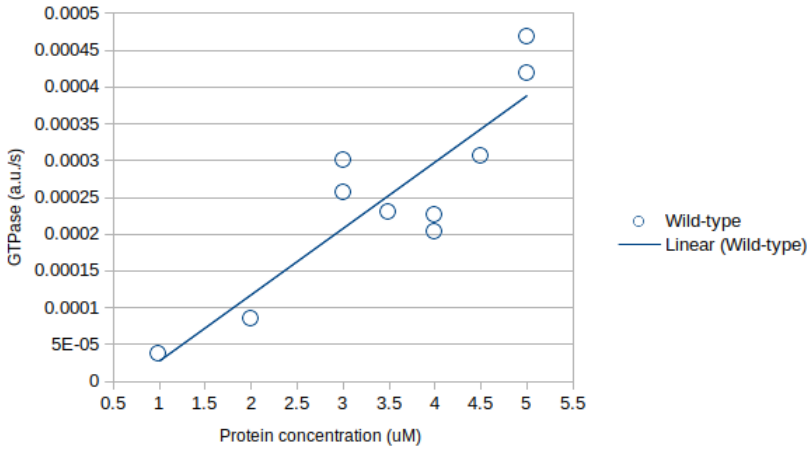

Figure 5.10: GTPase activity measured by proxy NADH absorption at 340 nm for the wild-type FtsZ protein with 0.5 mM GTP using a regenerative coupled GTPase assay.

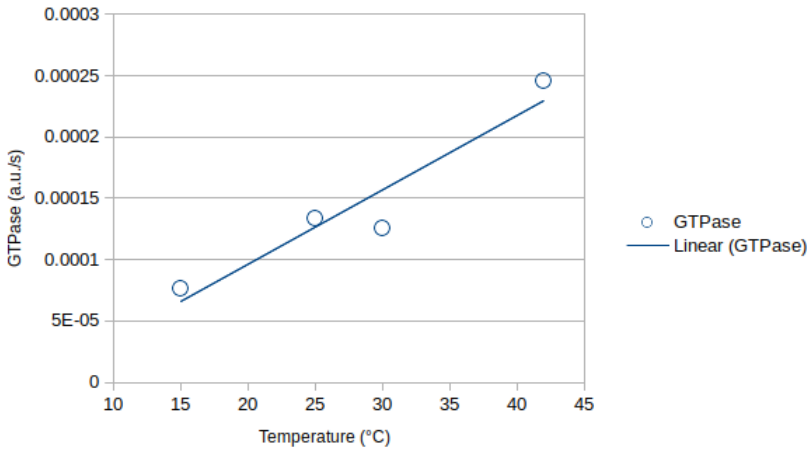

Figure 5.11: GTPase activity measured by proxy NADH absorption at 340 nm for the FtsZ mutant Z84 (G105S) at 5 μM with 0.5 mM GTP using a regenerative coupled GTPase assay at different temperatures.

5.6 Discussion

During this experimental work, we set out to probe the assembly of the temperature-sensitive mutant Ftsz84 by creating tryptophan mutants and using fluorescence assays. We have created 4 of those mutants: L68W/84, Y222W/84, L189W/84 and T151C/Y222W/84.

From these four mutants, three presented no signal change during preliminary work, indicating no activity; the Bodipy-labelled T151C/Y222W/84 became, then, the main focus of our study. This mutant, in which the added cysteine is close to the tryptophan, was labelled with Bodipy, a fluorophore, that was then quenched by the tryptophan, following the procedure outlined in previous works with a similar mutant [Chen and Erickson, 2011].

We measured the fluorescence spectra of this mutant in the presence of different nucleotides. Though the fluorescence measured in the presence of GTP was consistently lower than without the nucleotide, the difference was quite small and inconclusive with regards to the source of the decrease.

We, then, compared the effect of addition of GTP and GDP to a mix of sub-critical concentration of our mutant and a variable concentration of wild-type protein. Again, the results are inconclusive: adding nucleotide decreased fluorescence, but there was enough variability between samples to make any conclusions very doubtful. Furthermore, adding ATP and GTP or either one of them seemed to yield no significant difference, either.

Our electron microscopy work seems to show that addition of GTP to the mutant ftsZ84 yields aggregate structures with no discernible structure; increased GTP concentration created larger aggregates. However, the mutant T151C/Y222W/84 did not show any evidence of assembly, labelled or unlabelled.

Finally, we used a regenerative assay to measure the GTPase activity of the ftsZ84 mutant. We found it to increase linearly with protein concentration, as expected, and be roughly 25% of the wild-type activity. We have also found it to be increasing with temperature, as opposed to the previously reported in the literature.

Unfortunately, there is very little conclusive evidence regarding ftsZ84 assembly *in vitro*. The tryptophan mutants seemed largely inactive, with some

baffling results upon addition of nucleotides; as a result, it is hard to gauge how significant these results are, given the relatively small changes in fluorescence that are seen.

There is evidence for some assembly, though. The fact that this mutant presents roughly 25% of the GTPase activity of the wild-type and the presence of large aggregate structures in EM seem to indicate there is at least some degree of assembly taking place. However, the normal cell cycle times of this mutant *in vivo* are still unexplained.

Chapter 6

Conclusion

In the last few years, the scientific community and, increasingly, the political powers in multiple countries have recognized bacterial infections as a serious threat to healthcare at a global scale as we move towards a possible crisis situation where antimicrobial resistance becomes commonplace. The American Centers for Disease Control and Prevention (CDC) detailed a course of action to tackle this problem, concentrating on reducing antibiotic prescriptions, more investment in new diagnostics and drugs, preventing infections from spreading and improving resistance tracking [for Disease Control et al., 2014].

Meanwhile, the World Health Organisation pointed to gaps in reporting and surveillance of antimicrobial resistance internationally, and calls the situation "alarming". [Organization et al., 2014] The UK Chief Medical Officer expressed concerns over the outlook regarding this subject, and in 2013 the Government published a five-year plan with detailed targets to be met related to investment in new drugs, conservation of existing treatments and making the general public aware of the scale of the problem [Davies and Gibbens, 2013].

The process through which bacteria divide is still not completely understood. In particular, the mechanism for force generation during bacterial cytokinesis is unclear. Many of the proteins involved in these processes are well conserved amongst a wide range of bacteria, and are also essential to life. [Silver, 2011] Though currently not well explored, the proteins in the divisome are, thus, an excellent target for possible new antibacterial drugs [den

Blaauwen et al., 2014].

There are two main theories for how bacteria can generate the contractile force necessary for division without molecular motors. The first advocate a process of increasing lateral interactions between filaments by sliding [Erickson et al., 2010]. However, this requires dynamics that do not agree with the fast turnover of FtsZ monomers *in vivo* [Stricker et al., 2002; Anderson et al., 2004; Chen and Erickson, 2005], it does not agree with the existence of regions of low FtsZ density in the Z-ring [Rowlett and Margolin, 2014; Strauss et al., 2012; Holden et al., 2014] and it would require the breakage of many lateral bonds when sliding occurred [Erickson, 2009].

The second advocates a system based on "iterative pinching" [Li et al., 2007]: upon GTP hydrolysis, FtsZ filaments would change from a straight to a bent conformation, generating a local force. By keeping this process active throughout the Z-ring, a net contractile force could be achieved. There is some evidence for a conformational switch in FtsZ filaments [Erickson et al., 1996; Lu et al., 2000]; however, crystal structures of GTP and GDP-bound FtsZ monomers do not show conclusive evidence of any hinge-like mechanism [Ray-Chaudhuri and Park, 1992; de Boer et al., 1992; Mukherjee and Lutkenhaus, 1998; Erickson et al., 1996; Yu and Margolin, 1997; Bramhill and Thompson, 1994; Chen et al., 2005; González et al., 2003].

In this work, we have focused on exploring the role of assembly of the bacterial protein FtsZ in force generation during bacterial division. This was done both from a theoretical perspective, by modelling a novel mechanism for generating forces, and from an experimental perspective, studying the assembly of the mutant FtsZ84 and trying to understand the relationship between FtsZ assembly and constriction.

Importantly, we show that the presence of diffusible cross-linking proteins can generate contractility through entropic forces. Inspired by experimental work showing that the presence of such molecules cross-linking microtubules generate entropic forces that want to expand areas of lateral overlap [Lansky et al., 2015], we constructed a model to investigate the consequences of such mechanisms in the context of bacterial division, and to evaluate the possible relevance of these forces; in the experimental work of Lansky et al., the forces generated by this mechanism have been measured to be in ranges

that are relevant in biological processes.

We have shown that, using the same mechanism presented experimentally using tubulin and the cross-linker Ase1 [Braun et al., 2016; Lansky et al., 2015], a single filament cross-linked to itself would present contractile behaviour in the presence of diffusible cross-linkers. Just as in the experimental set up, the entropic force generated by the cross-linked wants to expand the overlap length, causing the effective force to be contractile. This effect does not depend on filament rigidity or length, as long as a lateral overlap exists and diffusible cross-linkers are present. It is also independent of any dynamics or kinetics. For some values of parameters, the effective force generated can overcome filament rigidity to cause contraction. Alternatively, it is possible to calculate the filament rigidity from the contraction profile.

To achieve the goal of sustaining constriction, we have shown that it is necessary to have, at least, kinetics of depolymerisation for the filament. This process works by decreasing the length of lateral overlap, increasing cross-linker density (and, thus, contractile force). This is, then, the opposite of what contraction does. The energy stored in the polymerised filament is, therefore, effectively harnessed to achieve further constriction. We have also demonstrated that the kinetics of cross-linkers can affect the generated contraction, with weakly-bound cross-linkers not being able to sustain contractile forces and cross-linkers that are too strongly bound "jamming" the system in the dense limit. Finally, our simulations highlighted the importance of the balance between binding and depolymerisation kinetics, with fast depolymerisation leading to lower maximum force and faster constriction, while slower depolymerisation means further constriction, but at a slower rate.

Next, we investigated the dynamics of filament bundles in the presence of diffusible cross-linkers. The same effective force is also at play in these systems; however, this acts towards maximizing the overlap regions between filaments, and for most cases this is done simply by aligning the filaments next to each other as seen in experimental data for tubulin [Braun et al., 2016; Lansky et al., 2015].

However, it is possible to use this mechanism to create net contractile forces in bundles of filaments. To achieve this goal, we constructed simple systems with the presence of multi-filament bundles. With no dynamics present,

two of the three systems with percolating bundles were contractile, but contraction stopped quickly since the forces decrease through expansion of lateral overlap regions and increased restoring force from the membrane Hamiltonian.

Upon the introduction of depolymerisation dynamics, all sample systems were contractile, decreasing in size until reaching a "jammed" state where no depolymerisation can occur. The forces being generated increase with increased number of lateral overlap areas, and we have shown that having multiple percolating clusters in parallel cause the net force to be the sum of the individual forces generated by each cluster.

We, then, make it clear that percolation in these bundles is essential to the constricting forces being generated. By removing a single cross-linker from the sample systems being simulated, all contractility is lost, and these bundles are incapable of generating any contractile forces, as seen in nature.

Furthermore, we have concluded that percolation is necessary but not sufficient to generate contractile forces. That was already the case when simulating one of the sample systems; it was percolating but, without depolymerisation dynamics, it was not contracting. To confirm how general that fact is, we have simulated systems with all available dynamics (polymer addition, depolymerisation, cross-linking, removal of cross-linkers, contraction and expansion). In this case, it was also clear that there were many situations with percolating clusters where the net forces were not contractile. The entropic forces generated by both the other, "free" polymers in the system and the translational freedom of the filaments in the percolating cluster both contribute to go against contractility, and might be stronger than that.

At the end of our theoretical work, we focus on generating percolating clusters from the dynamical behaviours we have defined previously. We studied the effect of depolymerisation rates and cross-linking energies, concluding that low depolymerisation and low cross-linking energies were conducive to percolation and contractility. Then, we were able to achieve 60-70% percolation rates by using low depolymerisation rates, low cross-linker energies, high polymerisation and cross-linking rates. However, these cases resulted in "jamming", which was both unfavourable to contraction and expensive to simulate. As a final step, we introduced time-dependent kinetics, increasing depolymerisation rates when percolation happened. Contraction could, then, be achieved, but

not in a reliable fashion. This indicates that it is unlikely that all relevant dynamics for cytokinesis have been captured by this model; as an example, filament treadmilling has not been included in this model, though the directional nature of filaments can be relevant in bypassing the percolation requirement.

Finally, some experimental work was undertaken while on secondment at Duke University. Our initial goal was to assay the assembly of the temperature-sensitive mutant ftsZ84 by measuring fluorescence changes in tryptophan mutants. Four different mutants were created: L68W/84, Y222W/84, L189W/84 and T151C/Y222W/84. After some initial screening, work was focused on the T151C/Y222W/84 mutant. This species, through the addition of a cysteine close to the tryptophan, could then be labelled with the fluorophore Bodipy. That fluorophore could, then, be quenched by the tryptophan.

We could, then, measure the fluorescence of this mutant in the presence of different nucleotides. Fluorescence was consistently lower in the presence of GTP than in its absence, but the difference was very small and the source of such difference was not clear. Then, a mix of sub-critical concentration of the mutant and added wild-type protein presented decreased fluorescence upon addition of both GTP and GDP, with variability between samples large enough to render the results unclear. Finally, adding ATP, GTP or both all yielded similar results.

Electron microscopy of the T151C/Y222W/84 mutant (both labelled and unlabelled with Bodipy) did not show any indication of assembly occurring. The mutant ftsZ84, however, shower aggregates with no clear structure upon the addition of GTP; higher GTP concentrations yielded larger aggregates. In addition to that, we have performed a regenerative assay to measure ftsZ84 GTPase activity. It increased linearly with protein concentration as predicted, but at roughly 25% of the activity presented by wild-type protein. Contrary to what was reported in the literature, we have also found this activity to increase with temperature.

The ftsZ84 assembly, then, remains elusive. The tryptophan mutants presented no clear activity with inconclusive results upon addition of nucleotides. The presence of aggregates in electron microscopy the detected GTPase activity (though much lower than the wild-type) seem to point towards at least some degree of assembly, though. It is not clear, however, the

mechanism through which normal cell cycle times can be possible for bacteria with this mutant.

At the end, this work has shown that diffusible cross-linkers are a credible source of forces at biologically relevant scales, and that ring-like geometries can be especially conducive to harnessing these forces into contraction. It is clear, however, that the unreliable nature of the contraction processes induced by the dynamics that are present in this model does not agree with the experimental evidence showing bacterial cytokinesis to be an extremely reliable process.

It is, therefore, unlikely that this model can be directly applied to bacterial division as is. Due to the focus on ensemble properties and equilibrium processes present in this work, there are certain features that simply cannot be captured without significantly reworking this model from the ground up: directional motion, preferential attachment of proteins at certain areas of the membrane, filament polarity are all features that can be relevant for bacterial division and that cannot be included in this model.

Furthermore, when thinking about this model in the context of bacterial cell division, it is important to keep in mind the lack of an experiment with similar results to the ones achieved by Lansky et al. [Lansky et al., 2015] for tubulin - however, the existence of many bundling agents that can bind to FtsZ [Pacheco-Gómez et al., 2013; Small et al., 2007] indicate that such discovery is possible; if the diffusion time scales associated with these cross-linkers are fast enough compared to the other processes occurring in FtsZ filament bundles, the results presented in this work would also be valid.

In addition to that, the mechanisms presented in this thesis are not exclusive to bacterial division. The results are general for any system with filaments or filament bundles obeying the assumptions that were made when constructing this model. As previously mentioned, fast cross-linker diffusion dynamics when compared to the other processes at hand are essential for the equilibrium approach adopted to work.

This, then, adds to the catalogue of possible mechanisms involved in the motor-free force generation in biological systems. We were able to demonstrate that forces at biologically relevant scales can be generated by filaments or bundles of filaments cross-linked by rapidly diffusing molecules, and that such

forces can be used for motor-free contraction in ring-like geometries.

Bibliography

Unknown_Siegel-Monte MW.pdf_Unknown.pdf.

S G Addinall and J Lutkenhaus. FtsZ-spirals and -arcs determine the shape of the invaginating septa in some mutants of Escherichia coli. *Molecular Microbiology*, 22(2):231–237, 1996.

Stephen G. Addinall, Chune Cao, and Joe Lutkenhaus. Temperature shift experiments with an ftsZ84(Ts) strain reveal rapid dynamics of FtsZ localization and indicate that the Z ring is required throughout septation and cannot reoccupy division sites once constriction has initiated. *Journal of Bacteriology*, 179(13):4277–4284, 1997. ISSN 00219193.

JF Allard and EN Cytrynbaum. Force generation by a dynamic Z-ring in Escherichia coli cell division. *Proceedings of the National ...*, 106(1):145–50, January 2009. ISSN 1091-6490. doi: 10.1073/pnas.0808657106. URL `http://www.pnas.org/content/106/1/145.shorthttp://www.pubmedcentral.nih.gov/articlerender.fcgi?artid=2629190\&tool=pmcentrez\&rendertype=abstract`.

Jane Smith Allen, Camille C Filip, Ralph A Gustafson, Robert G Allen, and James R Walker. Regulation of bacterial cell division: genetic and phenotypic analysis of temperature-sensitive, multinucleate, filament-forming mutants of escherichia coli. *Journal of bacteriology*, 117(3):978–986, 1974.

David E Anderson, Frederico J Gueiros-filho, P Erickson, and Harold P Erickson. Assembly Dynamics of FtsZ Rings in Bacillus subtilis and Escherichia coli and Effects of FtsZ-Regulating Proteins Assembly Dynamics of FtsZ Rings in Bacillus subtilis and Escherichia coli and Effects of FtsZ-Regulating Proteins. *Journal of Bacteriology*, 2004. doi: 10.1128/JB.186.17.5775.

David E Anderson, Michelle B Kim, Jared T Moore, Terrence E OBrien, Nohemy A Sorto, Charles I Grove, Laura L Lackner, James B Ames, and Jared T Shaw. Comparison of small molecule inhibitors of the bacterial cell division protein ftsz and identification of a reliable cross-species inhibitor. *ACS chemical biology*, 7(11):1918, 2012.

José M Andreu, Claudia Schaffner-Barbero, Sonia Huecas, Dulce Alonso, María L Lopez-Rodriguez, Laura B Ruiz-Avila, Rafael Núñez-Ramírez, Oscar Llorca, and Antonio J Martín-Galiano. The antibacterial cell division inhibitor pc190723 is an ftsz polymer-stabilizing agent that induces filament assembly and condensation. *Journal of Biological Chemistry*, 285(19): 14239–14246, 2010.

Anonymous. Less talk, more action. *Nature Reviews Microbiology*, 11(5): 295–295, apr 2013. doi: 10.1038/nrmicro3025. URL `https://doi.org/10.1038%2Fnrmicro3025`.

Matthew W Bailey, Paola Bisicchia, Boyd T Warren, David J Sherratt, and Jaan Männik. Evidence for divisome localization mechanisms independent of the min system and slma in escherichia coli. *PLoS genetics*, 10(8):e1004504, 2014.

Alexander Barvinok and James E Pommersheim. An algorithmic theory of lattice points. *New perspectives in algebraic combinatorics*, 38:91, 1999.

Alexander I Barvinok. A polynomial time algorithm for counting integral points in polyhedra when the dimension is fixed. *Mathematics of Operations Research*, 19(4):769–779, 1994.

H CP Berbee, C GE Boender, A HG Rinnooy Ran, CL Scheffer, Robert L Smith, and Jan Telgen. Hit-and-run algorithms for the identification of nonredundant linear inequalities. *Mathematical Programming*, 37(2):184–207, 1987.

Thomas G Bernhardt and Piet AJ De Boer. Slma, a nucleoid-associated, ftsz binding protein required for blocking septal ring assembly over chromosomes in e. coli. *Molecular cell*, 18(5):555–564, 2005.

Erfei Bi and J Lutkenhaus. Ftsz regulates frequency of cell division in escherichia coli. *Journal of bacteriology*, 172(5):2765–2768, 1990.

Erfei Bi and Joe Lutkenhaus. Ftsz ring structure associated with division in escherichia coli. *Nature*, 354(6349):161, 1991.

Kurt Binder, Dieter Heermann, Lyle Roelofs, A John Mallinckrodt, Susan McKay, et al. Monte carlo simulation in statistical physics. *Computers in Physics*, 7(2):156–157, 1993.

Alexandre Wilson Bisson Filho, Yen-Pang Hsu, Georgia Squyres, Erkin Kuru, Fabai Wu, Calum Jukes, Cees Dekker, Seamus Holden, Michael VanNieuwenhze, Yves Brun, et al. Treadmilling by ftsz filaments drives peptidoglycan synthesis and bacterial cell division. *bioRxiv*, page 077560, 2016.

Bernard Boigelot and Louis Latour. Counting the solutions of presburger equations without enumerating them. *Theoretical Computer Science*, 313 (1):17–29, 2004.

Peer Bork, Chris Sander, and Alfonso Valencia. An atpase domain common to prokaryotic cell cycle proteins, sugar kinases, actin, and hsp70 heat shock proteins. *Proceedings of the National Academy of Sciences*, 89(16):7290–7294, 1992.

D Bramhill and C M Thompson. GTP-dependent polymerization of Escherichia coli FtsZ protein to form tubules. *Proceedings of the National Academy of Sciences of the United States of America*, 91(13):5813–5817, 1994. ISSN 0027-8424. doi: 10.1073/pnas.91.13.5813.

Marcus Braun, Zdenek Lansky, Gero Fink, Felix Ruhnow, Stefan Diez, and Marcel E Janson. Adaptive braking by ase1 prevents overlapping microtubules from sliding completely apart. *Nature cell biology*, 13(10):1259–1264, 2011.

Marcus Braun, Zdenek Lansky, Feodor Hilitski, Zvonimir Dogic, and Stefan Diez. Entropic forces drive contraction of cytoskeletal networks. *BioEssays*, 38(5):474–481, 2016.

Michel Brion. Points entiers dans les polyedres convexes. *Ann. Sci. Ecole Norm. Sup*, 21(4):653–663, 1988.

Nienke Buddelmeijer and Jon Beckwith. A complex of the escherichia coli cell division proteins ftsl, ftsb and ftsq forms independently of its localization to the septal region. *Molecular microbiology*, 52(5):1315–1327, 2004.

Michael R Caplan and Harold P Erickson. Apparent cooperative assembly of the bacterial cell division protein ftsz demonstrated by isothermal titration calorimetry. *Journal of Biological Chemistry*, 278(16):13784–13788, 2003.

Joseph C Chen and Jon Beckwith. Ftsq, ftsl and ftsi require ftsk, but not ftsn, for co-localization with ftsz during escherichia coli cell division. *Molecular microbiology*, 42(2):395–413, 2001.

Joseph C Chen, David S Weiss, Jean-Marc Ghigo, and Jon Beckwith. Septal localization of ftsq, an essential cell division protein in escherichia coli. *Journal of bacteriology*, 181(2):521–530, 1999.

Yaodong Chen and Harold P. Erickson. Rapid in vitro assembly dynamics and subunit turnover of FtsZ demonstrated by fluorescence resonance energy transfer. *Journal of Biological Chemistry*, 280(23):22549–22554, 2005. ISSN 00219258. doi: 10.1074/jbc.M500895200.

Yaodong Chen and Harold P. Erickson. Conformational changes of FtsZ reported by tryptophan mutants. *Biochemistry*, 50(21):4675–4684, 2011. ISSN 00062960. doi: 10.1021/bi200106d.

Yaodong Chen, Keith Bjornson, Sambra D Redick, and Harold P Erickson. A rapid fluorescence assay for FtsZ assembly indicates cooperative assembly with a dimer nucleus. *Biophysical journal*, 88(1):505–514, 2005. ISSN 00063495. doi: 10.1529/biophysj.104.044149.

Ian Chopra. The 2012 garrod lecture: Discovery of antibacterial drugs in the 21st century. *Journal of Antimicrobial Chemotherapy*, page dks436, 2012.

Philippe Clauss and Vincent Loechner. Parametric analysis of polyhedral iteration spaces. In *Application Specific Systems, Architectures and Processors,*

1996. ASAP 96. Proceedings of International Conference on, pages 415–424. IEEE, 1996.

Brian D Corbin, Yipeng Wang, Tushar K Beuria, and William Margolin. Interaction between cell division proteins ftse and ftsz. *Journal of bacteriology*, 189(8):3026–3035, 2007.

Suzanne C Cordell, Elva JH Robinson, and Jan Löwe. Crystal structure of the sos cell division inhibitor sula and in complex with ftsz. *Proceedings of the National Academy of Sciences*, 100(13):7889–7894, 2003.

Alex Dajkovic, Ganhui Lan, SX Sun, Denis Wirtz, and Joe Lutkenhaus. MinC spatially controls bacterial cytokinesis by antagonizing the scaffolding function of FtsZ. *Current Biology*, 18(4):235–44, February 2008. ISSN 0960-9822. doi: 10.1016/j.cub.2008.01.042. URL `http://www.ncbi.nlm.nih.gov/pubmed/18291654http://www.sciencedirect.com/science/article/pii/S0960982208000894`.

SC Davies and N Gibbens. Uk five year antimicrobial resistance strategy 2013 to 2018. *London: Department of Health*, 2013.

P de Boer, R Crossley, and L Rothfield. The essential bacterial cell-division protein FtsZ is a GTPase. *Nature*, 359(6392):254–256, 1992. ISSN 0028-0836. doi: 10.1038/359254a0.

PA De Boer, Robin E Crossley, and Lawrence I Rothfield. Central role for the escherichia coli minc gene product in two different cell division-inhibition systems. *Proceedings of the National Academy of Sciences*, 87(3):1129–1133, 1990.

Piet AJ de Boer, Robin E Crossley, and Lawrence I Rothfield. A division inhibitor and a topological specificity factor coded for by the minicell locus determine proper placement of the division septum in e. coli. *Cell*, 56(4):641–649, 1989.

Jesús A De Loera, Raymond Hemmecke, Jeremiah Tauzer, and Ruriko Yoshida. Effective lattice point counting in rational convex polytopes. *Journal of symbolic computation*, 38(4):1273–1302, 2004.

Tanneke den Blaauwen. Prokaryotic cell division: flexible and diverse. *Current opinion in microbiology*, 16(6):738–744, 2013.

Tanneke Den Blaauwen, Miguel A De Pedro, Martine Nguyen-Distèche, and Juan A Ayala. Morphogenesis of rod-shaped sacculi. *FEMS microbiology reviews*, 32(2):321–344, 2008.

Tanneke den Blaauwen, José M Andreu, and Octavio Monasterio. Bacterial cell division proteins as antibiotic targets. *Bioorganic chemistry*, 55:27–38, 2014.

Paul Doucet and Peter B Sloep. *Mathematical modeling in the life sciences*. Ellis Horwood New York, 1992.

Claire E Dow, Alison Rodger, David I Roper, and Hugo A van den Berg. A model of membrane contraction predicting initiation and completion of bacterial cell division. *Integrative Biology*, 5(5):778–795, 2013.

Jorge Durand-Heredia, Eugene Rivkin, Guoxiang Fan, Jorge Morales, and Anuradha Janakiraman. Identification of zapd as a cell division factor that promotes the assembly of ftsz in escherichia coli. *Journal of bacteriology*, 194(12):3189–3198, 2012.

Jorge M Durand-Heredia, H Yu Helen, Sacha De Carlo, Cammie F Lesser, and Anuradha Janakiraman. Identification and characterization of zapc, a stabilizer of the ftsz ring in escherichia coli. *Journal of bacteriology*, 193(6): 1405–1413, 2011.

Martin Dyer, Alan Frieze, and Ravindran Kannan. *A random polynomial time algorithm for estimating volumes of convex bodies*. University of Leeds, School of Computer Studies, 1988.

Alexander JF Egan and Waldemar Vollmer. The physiology of bacterial cell division. *Annals of the New York Academy of Sciences*, 1277(1):8–28, 2013.

Nathaniel L. Elsen, Jun Lu, Gopal Parthasarathy, John C. Reid, Sujata Sharma, Stephen M. Soisson, and Kevin J. Lumb. Mechanism of action

of the cell-division inhibitor PC190723: Modulation of FtsZ assembly cooperativity. *Journal of the American Chemical Society*, 134(30):12342–12345, 2012. ISSN 00027863. doi: 10.1021/ja303564a.

M Enrique, Anna Mandinova, Michel O Steinmetz, Daniel Stoffler, Ueli Aebi, and Thomas D Pollard. Polymerization and structure of nucleotide-free actin filaments. *Journal of molecular biology*, 295(3):517–526, 2000.

H P Erickson. Modeling the physics of FtsZ assembly and force generation. *Proceedings of the National Academy of Sciences*, 106(23):9238–9243, 2009. URL `http://www.pubmedcentral.nih.gov/articlerender.fcgi?artid=2695047\&tool=pmcentrez\&rendertype=abstracthttp://www.pnas.org/content/106/23/9238.short`.

H P Erickson, D W Taylor, K a Taylor, and D Bramhill. Bacterial cell division protein FtsZ assembles into protofilament sheets and minirings, structural homologs of tubulin polymers. *Proceedings of the National Academy of Sciences of the United States of America*, 93(January):519–523, 1996. ISSN 0027-8424. doi: 10.1073/pnas.93.1.519.

Harold P Erickson. Ftsz, a prokaryotic homolog of tubulin? *Cell*, 80(3): 367–370, 1995.

Harold P Erickson, David E Anderson, and Masaki Osawa. FtsZ in bacterial cytokinesis: cytoskeleton and force generator all in one. *Microbiology and molecular biology reviews : MMBR*, 74(4):504–28, December 2010. ISSN 1098-5557. doi: 10.1128/MMBR.00021-10. URL `http://www.pubmedcentral.nih.gov/articlerender.fcgi?artid=3008173\&tool=pmcentrez\&rendertype=abstract`.

Olivier Espéli, Romain Borne, Pauline Dupaigne, Axel Thiel, Emmanuelle Gigant, Romain Mercier, and Frédéric Boccard. A matp–divisome interaction coordinates chromosome segregation with cell division in e. coli. *The EMBO journal*, 31(14):3198–3211, 2012.

Alfred S Evans. Causation and disease: A chronological journey the thomas parran lecture. *American Journal of Epidemiology*, 108(4):249–258, 1978.

Andrea Feucht, Isabelle Lucet, Michael D Yudkin, and Jeffery Errington. Cytological and biochemical characterization of the ftsa cell division protein of bacillus subtilis. *Molecular microbiology*, 40(1):115–125, 2001.

Centers for Disease Control, Prevention, et al. Antibiotic resistance threats in the united states, 2013. 2013. *Centers for Disease Control and Prevention, US Department of Health and Human Services: Atlanta, GA*, 2014.

Claudine Fraipont, Svetlana Alexeeva, Benoît Wolf, Rene van der Ploeg, Marie Schloesser, Tanneke den Blaauwen, and Martine Nguyen-Distèche. The integral membrane ftsw protein and peptidoglycan synthase pbp3 form a subcomplex in escherichia coli. *Microbiology*, 157(1):251–259, 2011.

Guo Fu, Tao Huang, Jackson Buss, Carla Coltharp, Zach Hensel, and Jie Xiao. In Vivo structure of the E. coli FtsZ-ring revealed by photoactivated localization microscopy (PALM). *PLoS ONE*, 5(9):1–16, January 2010. ISSN 19326203. doi: 10.1371/journal.pone.0012680. URL `http://www.pubmedcentral.nih.gov/articlerender.fcgi?artid=2938336\&tool=pmcentrez\&rendertype=abstract`.

Elisa Galli and Kenn Gerdes. Ftsz-zapa-zapb interactome of escherichia coli. *Journal of bacteriology*, 194(2):292–302, 2012.

Cunjing Ge and Feifei Ma. A fast and practical method to estimate volumes of convex polytopes. In *International Workshop on Frontiers in Algorithmics*, pages 52–65. Springer, 2015.

Brett Geissler and William Margolin. Evidence for functional overlap among multiple bacterial cell division proteins: compensating for the loss of ftsk. *Molecular microbiology*, 58(2):596–612, 2005.

Jean-Marc Ghigo, David S Weiss, Joseph C Chen, Justin C Yarrow, and Jon Beckwith. Localization of ftsl to the escherichia coli septal ring. *Molecular microbiology*, 31(2):725–737, 1999.

Nathan W Goehring, Frederico Gueiros-Filho, and Jon Beckwith. Premature targeting of a cell division protein to midcell allows dissection of divisome assembly in escherichia coli. *Genes & development*, 19(1):127–137, 2005.

J M González and Marisela Vélez. Cooperative behavior of Escherichia coli cell-division protein FtsZ assembly involves the preferential cyclization of long single-stranded fibrils. *Proceedings of the ...*, 102(6):1895–1900, 2005. URL `http://www.pubmedcentral.nih.gov/articlerender.fcgi?artid=548572\&tool=pmcentrez\&rendertype=abstracthttp://www.pnas.org/content/102/6/1895.short`.

José Manuel González, Mercedes Jiménez, Marisela Vélez, Jesús Mingorance, José Manuel Andreu, Miguel Vicente, and Germán Rivas. Essential cell division protein ftsz assembles into one monomer-thick ribbons under conditions resembling the crowded intracellular environment. *Journal of Biological Chemistry*, 278(39):37664–37671, 2003.

Brian Gough. *GNU scientific library reference manual*. Network Theory Ltd., 2009.

Torbjörn Granlund. the gmp development team. gnu mp: The gnu multiple precision arithmetic library, 5.0. 2012.

Frederico J Gueiros-Filho and Richard Losick. A widely conserved bacterial cell division protein that promotes assembly of the tubulin-like protein ftsz. *Genes & development*, 16(19):2544–2556, 2002.

Daniel P Haeusser and William Margolin. Splitsville: structural and functional insights into the dynamic bacterial z ring. *Nature Reviews Microbiology*, 14 (5):305–319, 2016.

Cynthia A Hale and Piet AJ de Boer. Direct binding of ftsz to zipa, an essential component of the septal ring structure that mediates cell division in e. coli. *Cell*, 88(2):175–185, 1997.

Cynthia A Hale and Piet AJ De Boer. Recruitment of zipa to the septal ring ofescherichia coli is dependent on ftsz and independent of ftsa. *Journal of bacteriology*, 181(1):167–176, 1999.

Cynthia A Hale, Hans Meinhardt, and Piet AJ de Boer. Dynamic localization cycle of the cell division regulator mine in escherichia coli. *The EMBO journal*, 20(7):1563–1572, 2001.

W Keith Hastings. Monte carlo sampling methods using markov chains and their applications. *Biometrika*, 57(1):97–109, 1970.

David J Haydon, Neil R Stokes, Rebecca Ure, Greta Galbraith, James M Bennett, David R Brown, Patrick J Baker, Vladimir V Barynin, David W Rice, Sveta E Sedelnikova, et al. An inhibitor of ftsz with potent and selective anti-staphylococcal activity. *Science*, 321(5896):1673–1675, 2008.

Jonne Helenius, Gary Brouhard, Yannis Kalaidzidis, Stefan Diez, and Jonathon Howard. The depolymerizing kinesin mcak uses lattice diffusion to rapidly target microtubule ends. *Nature*, 441(7089):115–119, 2006.

Wolfgang Helfrich. Elastic properties of lipid bilayers: theory and possible experiments. *Zeitschrift für Naturforschung C*, 28(11-12):693–703, 1973.

Y Hirota, A Ryter, and F Jacob. Thermosensitive mutants of e. coli affected in the processes of dna synthesis and cellular division. In *Cold Spring Harbor symposia on quantitative biology*, volume 33, pages 677–693. Cold Spring Harbor Laboratory Press, 1968.

Seamus J Holden, Thomas Pengo, Karin L Meibom, Carmen Fernandez Fernandez, Justine Collier, and Suliana Manley. High throughput 3d superresolution microscopy reveals caulobacter crescentus in vivo z-ring organization. *Proceedings of the National Academy of Sciences*, 111(12):4566–4571, 2014.

Timothy E Holy and Stanislas Leibler. Dynamic instability of microtubules as an efficient way to search in space. *Proceedings of the National Academy of Sciences*, 91(12):5682–5685, 1994.

Jen Hsin, Ajay Gopinathan, and Kerwyn C Huang. Nucleotide-dependent conformations of FtsZ dimers and force generation observed through molecular dynamics simulations. *Proceedings of the National Academy of Sciences of the United States of America*, 109(24):9432–7, June 2012. ISSN 1091-6490. doi: 10.1073/pnas.1120761109. URL `http://www.pubmedcentral.nih.gov/articlerender.fcgi?artid=3386107\&tool=pmcentrez\&rendertype=abstract`.

Zonglin Hu and Joe Lutkenhaus. Topological regulation of cell division in escherichia coli involves rapid pole to pole oscillation of the division inhibitor minc under the control of mind and mine. *Molecular microbiology*, 34(1): 82–90, 1999.

Zonglin Hu, Amit Mukherjee, Sebastien Pichoff, and Joe Lutkenhaus. The minc component of the division site selection system in escherichia coli interacts with ftsz to prevent polymerization. *Proceedings of the National Academy of Sciences*, 96(26):14819–14824, 1999.

Sonia Huecas, Oscar Llorca, Jasminka Boskovic, Jaime Martín-Benito, José María Valpuesta, and José Manuel Andreu. Energetics and geometry of ftsz polymers: nucleated self-assembly of single protofilaments. *Biophysical journal*, 94(5):1796–1806, 2008.

Olivier Huisman, RICHARD D'Ari, and Susan Gottesman. Cell-division control in escherichia coli: specific induction of the sos function sfia protein is sufficient to block septation. *Proceedings of the National Academy of Sciences*, 81(14):4490–4494, 1984.

Elena Ingerman and Jodi Nunnari. A continuous, regenerative coupled gtpase assay for dynamin-related proteins. *Methods in enzymology*, 404:611–619, 2005.

Celina Janion. Inducible sos response system of dna repair and mutagenesis in escherichia coli. *Int J Biol Sci*, 4(6):338–344, 2008.

Marcel E Janson, Rose Loughlin, Isabelle Loïodice, Chuanhai Fu, Damian Brunner, François J Nédélec, and Phong T Tran. Crosslinkers and motors organize dynamic microtubules to form stable bipolar arrays in fission yeast. *Cell*, 128(2):357–368, 2007.

Ravi Kannan, László Lovász, and Miklós Simonovits. Random walks and an o*(n5) volume algorithm for convex bodies. *Random structures and algorithms*, 11(1):1–50, 1997.

Lukas C Kapitein, Erwin JG Peterman, Benjamin H Kwok, Jeffrey H Kim, Tarun M Kapoor, and Christoph F Schmidt. The bipolar mitotic kinesin eg5

moves on both microtubules that it crosslinks. *Nature*, 435(7038):114–118, 2005.

Gouzel Karimova, Nathalie Dautin, and Daniel Ladant. Interaction network among escherichia coli membrane proteins involved in cell division as revealed by bacterial two-hybrid analysis. *Journal of bacteriology*, 187(7): 2233–2243, 2005.

Cynthia Hess Kenny, Weidong Ding, Kerry Kelleher, Susan Benard, Elizabeth Glasfeld Dushin, Alan G Sutherland, Lidia Mosyak, Ronald Kriz, and George Ellestad. Development of a fluorescence polarization assay to screen for inhibitors of the ftsz/zipa interaction. *Analytical biochemistry*, 323(2): 224–233, 2003.

Seksan Kiatsupaibul, Robert L Smith, and Zelda B Zabinsky. An analysis of a variation of hit-and-run for uniform sampling from general regions. *ACM Transactions on Modeling and Computer Simulation (TOMACS)*, 21(3):16, 2011.

Hyun Suk Kim, Narayanan Vijaykrishnan, M Kandemir, Erik Brockmeyer, Francky Catthoor, and Mary Jane Irwin. Estimating influence of data layout optimizations on sdram energy consumption. In *Low Power Electronics and Design, 2003. ISLPED'03. Proceedings of the 2003 International Symposium on*, pages 40–43. IEEE, 2003.

Michael A Kohanski, Daniel J Dwyer, and James J Collins. How antibiotics kill bacteria: from targets to networks. *Nature Reviews Microbiology*, 8(6): 423–435, 2010.

O Kratky and G Porod. Röntgenuntersuchung gelöster fadenmoleküle. *Recueil des Travaux Chimiques des Pays-Bas*, 68(12):1106–1122, 1949.

Ganhui Lan, C W Wolgemuth, and S X Sun. Z-ring force and cell shape during division in rod-like bacteria. *Proceedings of the ...*, 104(41):16110–16115, 2007. URL `http://www.pubmedcentral.nih.gov/articlerender.fcgi?artid=2042170\&tool=pmcentrez\&rendertype=abstracthttp://www.pnas.org/content/104/41/16110.short`.

Ganhui Lan, Brian R Daniels, Terrence M Dobrowsky, Denis Wirtz, and Sean X Sun. Condensation of ftsz filaments can drive bacterial cell division. *Proceedings of the National Academy of Sciences*, 106(1):121–126, 2009.

LD Landau and EM Lifshitz. *Statistical Physics: Course of Theoretical Physics*. Pergamon Press, 1958.

Zdenek Lansky, Marcus Braun, Annemarie Lüdecke, Michael Schlierf, Pieter Rein ten Wolde, Marcel E Janson, and Stefan Diez. Diffusible crosslinkers generate directed forces in microtubule networks. *Cell*, 160(6): 1159–1168, 2015.

Beatriz Lara, Ana Isabel Rico, Sabrina Petruzzelli, Antonella Santona, Jacques Dumas, Jacques Biton, Miguel Vicente, Jesús Mingorance, and Orietta Massidda. Cell division in cocci: localization and properties of the streptococcus pneumoniae ftsa protein. *Molecular microbiology*, 55(3):699–711, 2005.

Team Latte. Latte-a software dedicated to the problems of counting and detecting lattice points inside convex polytopes, and the solution of integer programs.

Ying Li, Jen Hsin, Lingyun Zhao, Yiwen Cheng, Weina Shang, Kerwyn Casey Huang, Hong-Wei Wang, and Sheng Ye. FtsZ protofilaments use a hinge-opening mechanism for constrictive force generation. *Science (New York, N.Y.)*, 341(6144):392–5, July 2013. ISSN 1095-9203. doi: 10.1126/science.1239248. URL `http://www.pubmedcentral.nih.gov/articlerender.fcgi?artid=3816583\&tool=pmcentrez\&rendertype=abstract`.

Zhuo Li, MJ J Trimble, YV V Brun, and GJ J Jensen. The structure of FtsZ filaments in vivo suggests a force-generating role in cell division. *The EMBO journal*, 26(22):4694–708, November 2007. ISSN 1460-2075. doi: 10.1038/sj.emboj.7601895. URL `http://www.pubmedcentral.nih.gov/articlerender.fcgi?artid=2080809\&tool=pmcentrez\&rendertype=abstracthttp://www.nature.com/emboj/journal/vaop/ncurrent/full/7601895a.html`.

Björn Lisper. Fully automatic, parametric worst-case execution time analysis. *WCET*, 3:77–80, 2003.

Zhan Liu, Amit Mukherjee, and Joe Lutkenhaus. Recruitment of zipa to the division site by interaction with ftsz. *Molecular microbiology*, 31(6):1853–1861, 1999.

Vincent Loechner. Polylib: A library for manipulating parameterized polyhedra, 1999.

Martin Loose and Timothy J Mitchison. The bacterial cell division proteins FtsA and FtsZ self-organize into dynamic cytoskeletal patterns. *Nature cell biology*, 16(1):38–46, January 2014. ISSN 1476-4679. doi: 10.1038/ncb2885. URL `http://www.ncbi.nlm.nih.gov/pubmed/24316672`.

László Lovász. *How to compute the volume?* DIMACS, Center for Discrete Mathematics and Theoretical Computer Science, 1991.

László Lovász. Hit-and-run mixes fast. *Mathematical Programming*, 86(3): 443–461, 1999.

László Lovász and Santosh Vempala. Hit-and-run is fast and fun. *preprint, Microsoft Research*, 2003.

László Lovász and Santosh Vempala. Hit-and-run from a corner. *SIAM Journal on Computing*, 35(4):985–1005, 2006.

Harry H Low, Martin C Moncrieffe, and Jan Löwe. The crystal structure of zapa and its modulation of ftsz polymerisation. *Journal of molecular biology*, 341(3):839–852, 2004.

J Löwe and L A Amos. Crystal structure of the bacterial cell-division protein FtsZ. *Nature*, 330(1996):1996–1999, 1998. URL `http://www.nature.com/nature/journal/v391/n6663/abs/391203a0.html`.

Susan Lowey and Kathleen M Trybus. Common structural motifs for the regulation of divergent class ii myosins. *Journal of Biological Chemistry*, 285(22):16403–16407, 2010.

C Lu, J Stricker, and H P Erickson. FtsZ from Escherichia coli, Azotobacter vinelandii, and Thermotoga maritima–quantitation, GTP hydrolysis, and

assembly. *Cell motility and the cytoskeleton*, 40(1):71–86, 1998. ISSN 0886-1544. doi: 10.1002/(SICI)1097-0169(1998)40:1⟨71::AID-CM7⟩3.0.CO;2-I.

C Lu, J Stricker, and H P Erickson. Site-specific mutations of FtsZ–effects on GTPase and in vitro assembly. *BMC microbiology*, 1:7, 2001. ISSN 1471-2180.

Chunlin Lu, Mary Reedy, and Harold P Erickson. Straight and Curved Conformations of FtsZ Are Regulated by GTP Hydrolysis Straight and Curved Conformations of FtsZ Are Regulated by GTP Hydrolysis. *Journal of Bacteriology*, 182(1), 2000. doi: 10.1128/JB.182.1.164-170.2000.Updated.

Joe Lutkenhaus. Assembly dynamics of the bacterial mincde system and spatial regulation of the z ring. *Annu. Rev. Biochem.*, 76:539–562, 2007.

Xiaolan Ma, David W Ehrhardt, and William Margolin. Colocalization of cell division proteins ftsz and ftsa to cytoskeletal structures in living escherichia coli cells by using green fluorescent protein. *Proceedings of the National Academy of Sciences*, 93(23):12998–13003, 1996.

Pablo Mateos-Gil, Alfonso Paez, Ines Hörger, Germán Rivas, Miguel Vicente, Pedro Tarazona, and Marisela Vélez. Depolymerization dynamics of individual filaments of bacterial cytoskeletal protein ftsz. *Proceedings of the National Academy of Sciences*, 109(21):8133–8138, 2012.

Pamela Maupin and Thomas D Pollard. Arrangement of actin filaments and myosin-like filaments in the contractile ring and of actin-like filaments in the mitotic spindle of dividing hela cells. *Journal of ultrastructure and molecular structure research*, 94(1):92–103, 1986.

Keri LN Mercer and David S Weiss. The escherichia coli cell division protein ftsw is required to recruit its cognate transpeptidase, ftsi (pbp3), to the division site. *Journal of Bacteriology*, 184(4):904–912, 2002.

Romain Mercier, Marie-Agnès Petit, Sophie Schbath, Stephane Robin, Meriem El Karoui, Frédéric Boccard, and Olivier Espéli. The matp/mats site-specific system organizes the terminus region of the e. coli chromosome into a macrodomain. *Cell*, 135(3):475–485, 2008.

Sara L Milam, Masaki Osawa, and Harold P Erickson. Negative-stain electron microscopy of inside-out FtsZ rings reconstituted on artificial membrane tubules show ribbons of protofilaments. *Biophysical journal*, 103 (1):59–68, July 2012. ISSN 1542-0086. doi: 10.1016/j.bpj.2012.05.035. URL `http://www.pubmedcentral.nih.gov/articlerender.fcgi?artid=3388225\&tool=pmcentrez\&rendertype=abstract`.

Jesús Mingorance, Michael Tadros, Miguel Vicente, José Manuel González, Germán Rivas, and Marisela Vélez. Visualization of single escherichia coli ftsz filament dynamics with atomic force microscopy. *Journal of Biological Chemistry*, 280(21):20909–20914, 2005.

Emily R Miraldi, Peter J Thomas, and Laura Romberg. Allosteric models for cooperative polymerization of linear polymers. *Biophysical journal*, 95(5): 2470–2486, 2008.

Saeko Mizusawa and Susan Gottesman. Protein degradation in escherichia coli: the lon gene controls the stability of sula protein. *Proceedings of the National Academy of Sciences*, 80(2):358–362, 1983.

Lidia Mosyak, Yan Zhang, Elizabeth Glasfeld, Steve Haney, Mark Stahl, Jasbir Seehra, and William S Somers. The bacterial cell-division protein zipa and its interaction with an ftsz fragment revealed by x-ray crystallography. *The EMBO journal*, 19(13):3179–3191, 2000.

Franklin J Moy, Elizabeth Glasfeld, Lidia Mosyak, and Robert Powers. Solution structure of zipa, a crucial component of escherichia coli cell division. *Biochemistry*, 39(31):9146–9156, 2000.

Amit Mukherjee and Joe Lutkenhaus. Dynamic assembly of ftsz regulated by gtp hydrolysis. *The EMBO journal*, 17(2):462–469, 1998.

Amit Mukherjee, Chune Cao, and Joe Lutkenhaus. Inhibition of ftsz polymerization by sula, an inhibitor of septation in escherichia coli. *Proceedings of the National Academy of Sciences*, 95(6):2885–2890, 1998.

Eva Nogales, Sharon G Wolf, and Kenneth H Downing. Structure of the $\alpha\beta$ tubulin dimer by electron crystallography. *Nature*, 391(6663):199–203, 1998.

Yoshiaki Ohashi, Yoshie Chijiiwa, Koichiro Suzuki, Kouki Takahashi, Hideaki Nanamiya, Tsutomu Sato, Yoshiko Hosoya, Kozo Ochi, and Fujio Kawamura. The lethal effect of a benzamide derivative, 3-methoxybenzamide, can be suppressed by mutations within a cell division gene, ftsz, in bacillus subtilis. *Journal of bacteriology*, 181(4):1348–1351, 1999.

Hirofumi Onishi, Sergey V Mikhailenko, and Manuel F Morales. Toward understanding actin activation of myosin atpase: the role of myosin surface loops. *Proceedings of the National Academy of Sciences*, 103(16):6136–6141, 2006.

Fumio Oosawa and Michiki Kasai. A theory of linear and helical aggregations of macromolecules. *Journal of molecular biology*, 4(1):10–21, 1962.

World Health Organization et al. *Antimicrobial resistance: 2014 global report on surveillance.* World Health Organization, 2014.

Masaki Osawa and Harold P Erickson. Inside-out Z rings–constriction with and without GTP hydrolysis. *Molecular microbiology*, 81(2):571–9, July 2011. ISSN 1365-2958. doi: 10.1111/j.1365-2958.2011.07716.x. URL `http://www.pubmedcentral.nih.gov/articlerender.fcgi?artid=3229917\&tool=pmcentrez\&rendertype=abstract`.

Masaki Osawa, D E Anderson, and H P Erickson. Reconstitution of contractile FtsZ rings in liposomes. *Science*, 320(5877):792–794, May 2008. ISSN 1095-9203. doi: 10.1126/science.1154520. URL `http://www.pubmedcentral.nih.gov/articlerender.fcgi?artid=2645864\&tool=pmcentrez\&rendertype=abstracthttp://www.sciencemag.org/content/320/5877/792.short`.

Masaki Osawa, David E Anderson, and Harold P Erickson. Curved FtsZ protofilaments generate bending forces on liposome membranes. *The EMBO journal*, 28(22):3476–84, November 2009. ISSN 1460-2075. doi: 10.1038/emboj.2009.277. URL `http://www.pubmedcentral.nih.gov/articlerender.fcgi?artid=2782090\&tool=pmcentrez\&rendertype=abstract`.

Raúl Pacheco-Gómez, Xi Cheng, Matthew R Hicks, Corinne J I Smith, David I Roper, Stephen Addinall, Alison Rodger, and Timothy R Dafforn. Tetramerization of ZapA is required for FtsZ bundling. *The Biochemical journal*, 449(3):795–802, February 2013. ISSN 1470-8728. doi: 10.1042/BJ20120140. URL `http://www.biochemj.org/bj/449/bj4490795.htmhttp://www.ncbi.nlm.nih.gov/pubmed/23098212`.

Young Sam Park, Charles I Grove, Marcos González-López, Sameer Urgaonkar, James C Fettinger, and Jared T Shaw. Synthesis of (-)-viriditoxin: A 6, 6-binaphthopyran-2-one that targets the bacterial cell division protein ftsz. *Angewandte Chemie International Edition*, 50(16):3730–3733, 2011.

Erin Parker and Siddhartha Chatterjee. An automata-theoretic algorithm for counting solutions to presburger formulas. In *International Conference on Compiler Construction*, pages 104–119. Springer, 2004.

P. Phoenix and G. R. Drapeau. Cell division control in Escherichia coli K-12: some properties of the ftsZ84 mutation and suppression of this mutation by the product of a newly identified gene. *Journal of Bacteriology*, 170(9): 4338–4342, 1988. ISSN 00219193.

Sebastien Pichoff and Joe Lutkenhaus. Unique and overlapping roles for zipa and ftsa in septal ring assembly in escherichia coli. *The EMBO journal*, 21 (4):685–693, 2002.

Sebastien Pichoff and Joe Lutkenhaus. Tethering the z ring to the membrane through a conserved membrane targeting sequence in ftsa. *Molecular microbiology*, 55(6):1722–1734, 2005.

J Pla, M Sanchez, P Patacios, M Vicente, and M Aldea. Preferential cytoplasmic location of ftsz, a protein essential for escherichia coli septation. *Molecular microbiology*, 5(7):1681–1686, 1991.

William Pugh. *Counting solutions to presburger formulas: How and why*, volume 29. ACM, 1994.

David M Raskin and Piet AJ de Boer. Rapid pole-to-pole oscillation of a

protein required for directing division to the middle of escherichia coli. *Proceedings of the National Academy of Sciences*, 96(9):4971–4976, 1999.

D RayChaudhuri and J T Park. Escherichia coli cell-division gene ftsZ encodes a novel GTP-binding protein. *Nature*, 359(6392):251–254, 1992. ISSN 0028-0836. doi: 10.1038/359251a0.

Debabrata RayChaudhuri. Zipa is a map–tau homolog and is essential for structural integrity of the cytokinetic ftsz ring during bacterial cell division. *The EMBO Journal*, 18(9):2372–2383, 1999.

Debabrata RayChaudhuri and James T Park. A point mutation converts escherichia coli ftsz septation gtpase to an atpase. *Journal of Biological Chemistry*, 269(37):22941–22944, 1994.

L Romberg, M Simon, and H P Erickson. Polymerization of Ftsz, a bacterial homolog of tubulin. is assembly cooperative? *The Journal of biological chemistry*, 276(15):11743–53, April 2001. ISSN 0021-9258. doi: 10.1074/jbc.M009033200. URL `http://www.ncbi.nlm.nih.gov/pubmed/11152458`.

Veronica Wells Rowlett and William Margolin. 3d-sim super-resolution of ftsz and its membrane tethers in escherichia coli cells. *Biophysical journal*, 107 (8):L17–L20, 2014.

Sonsoles Rueda, Miguel Vicente, and Jesús Mingorance. Concentration and assembly of the division ring proteins ftsz, ftsa, and zipa during the escherichia coli cell cycle. *Journal of bacteriology*, 185(11):3344–3351, 2003.

Benedikt Sabass, Margaret L Gardel, Clare M Waterman, and Ulrich S Schwarz. High resolution traction force microscopy based on experimental and computational advances. *Biophysical journal*, 94(1):207–220, 2008.

Dirk-Jan Scheffers, Janny G de Wit, Tanneke den Blaauwen, and Arnold JM Driessen. Substitution of a conserved aspartate allows cation-induced polymerization of ftsz. *FEBS letters*, 494(1):34–37, 2001.

Dirk-Jan Scheffers, Janny G de Wit, Tanneke den Blaauwen, and Arnold JM Driessen. Gtp hydrolysis of cell division protein ftsz: evidence that the

active site is formed by the association of monomers. *Biochemistry*, 41(2): 521–529, 2002.

Kari L Schmidt, Nicholas D Peterson, Ryan J Kustusch, Mark C Wissel, Becky Graham, Gregory J Phillips, and David S Weiss. A predicted abc transporter, ftsex, is needed for cell division in escherichia coli. *Journal of bacteriology*, 186(3):785–793, 2004.

JR Sellers, MD Pato, and RS Adelstein. Reversible phosphorylation of smooth muscle myosin, heavy meromyosin, and platelet myosin. *Journal of Biological Chemistry*, 256(24):13137–13142, 1981.

Victor Shoup et al. Ntl library. *Software Package*, 2009.

Lynn L Silver. Challenges of antibacterial discovery. *Clinical microbiology reviews*, 24(1):71–109, 2011.

Elaine Small, Rachel Marrington, Alison Rodger, David J Scott, Katherine Sloan, David Roper, Timothy R Dafforn, and Stephen G Addinall. Ftsz polymer-bundling by the escherichia coli zapa orthologue, ygfe, involves a conformational change in bound gtp. *Journal of molecular biology*, 369(1): 210–221, 2007.

Robert L Smith. Efficient monte carlo procedures for generating points uniformly distributed over bounded regions. *Operations Research*, 32(6):1296–1308, 1984.

Michael P Strauss, Andrew TF Liew, Lynne Turnbull, Cynthia B Whitchurch, Leigh G Monahan, and Elizabeth J Harry. 3d-sim super resolution microscopy reveals a bead-like arrangement for ftsz and the division machinery: implications for triggering cytokinesis. *PLoS biol*, 10(9):e1001389, 2012.

Jesse Stricker, Paul Maddox, ED Salmon, and Harold P Erickson. Rapid assembly dynamics of the escherichia coli ftsz-ring demonstrated by fluorescence recovery after photobleaching. *Proceedings of the National Academy of Sciences*, 99(5):3171–3175, 2002.

Qin Sun and William Margolin. Ftsz dynamics during the division cycle of liveescherichia coli cells. *Journal of Bacteriology*, 180(8):2050–2056, 1998.

I V Surovtsev, J J Morgan, and P A Lindahl. Kinetic modeling of the assembly, dynamic steady state, and contraction of the FtsZ ring in prokaryotic cytokinesis. *PLoS computational biology*, 4(7):e1000102, January 2008. ISSN 1553-7358. doi: 10.1371/journal.pcbi.1000102. URL `http://www.pubmedcentral.nih.gov/articlerender.fcgi?artid=2432035\&tool=pmcentrez\&rendertype=abstracthttp://dx.plos.org/10.1371/journal.pcbi.1000102`.

Piotr Szwedziak, Qing Wang, TAM Bharat, Matthew Tsim, and Jan Löwe. Architecture of the ring formed by the tubulin homologue FtsZ in bacterial cell division. *eLife*, pages 1–22, 2015. doi: 10.7554/eLife.04601. URL `http://elifesciences.org/content/3/e04601.abstract`.

Christopher M Tan, Alex G Therien, Jun Lu, Sang H Lee, Alexandre Caron, Charles J Gill, Christian Lebeau-Jacob, Liliana Benton-Perdomo, João M Monteiro, Pedro M Pereira, et al. Restoring methicillin-resistant staphylococcus aureus susceptibility to β-lactam antibiotics. *Science translational medicine*, 4(126):126ra35–126ra35, 2012.

Luke Tierney. Markov chains for exploring posterior distributions. *the Annals of Statistics*, pages 1701–1728, 1994.

Nam Ky Tonthat, Stefan T Arold, Brian F Pickering, Michael W Van Dyke, Shoudan Liang, Yue Lu, Tushar K Beuria, William Margolin, and Maria A Schumacher. Molecular mechanism by which the nucleoid occlusion factor, slma, keeps cytokinesis in check. *The EMBO journal*, 30(1):154–164, 2011.

Mary-Jane Tsang and Thomas G Bernhardt. Guiding divisome assembly and controlling its activity. *Current opinion in microbiology*, 24:60–65, 2015.

Désirée HH Tsao, Alan G Sutherland, Lee D Jennings, Yuanhong Li, Thomas S Rush, Juan C Alvarez, Weidong Ding, Elizabeth G Dushin, Russell G Dushin, Steve A Haney, et al. Discovery of novel inhibitors of the zipa/ftsz complex by nmr fragment screening coupled with structure-based design. *Bioorganic & medicinal chemistry*, 14(23):7953–7961, 2006.

Alexandru Turjan, Bart Kienhuis, and Ed Deprettere. A compile time based approach for solving out-of-order communication in kahn process networks.

In *Application-Specific Systems, Architectures and Processors, 2002. Proceedings. The IEEE International Conference on*, pages 17–28. IEEE, 2002.

Athanasios Typas, Manuel Banzhaf, Carol A Gross, and Waldemar Vollmer. From the regulation of peptidoglycan synthesis to bacterial growth and morphology. *Nature Reviews Microbiology*, 10(2):123–136, 2012.

P Van de Putte, Jeannette Van Dillewijn, and A Roersch. The selection of mutants of escherichia coli with impaired cell division at elevated temperature. *Mutation Research/Fundamental and Molecular Mechanisms of Mutagenesis*, 1(2):121–128, 1964.

Fusinita van den Ent, Linda A Amos, and Jan LoÈwe. Prokaryotic origin of the actin cytoskeleton. *Nature*, 413(6851):39–44, 2001.

S Verdoolaege. The barvinok library. *Website a t www. freecode. com/projects/barvinok*.

Sven Verdoolaege. isl: An integer set library for the polyhedral model. In *International Congress on Mathematical Software*, pages 299–302. Springer, 2010.

Sam Walcott, Patricia M Fagnant, Kathleen M Trybus, and David M Warshaw. Smooth muscle heavy meromyosin phosphorylated on one of its two heads supports force and motion. *Journal of Biological Chemistry*, 284(27): 18244–18251, 2009.

Jun Wang, Andrew Galgoci, Srinivas Kodali, Kithsiri B Herath, Hiranthi Jayasuriya, Karen Dorso, Francisca Vicente, Antonio González, Doris Cully, David Bramhill, et al. Discovery of a small molecule that inhibits cell division by blocking ftsz, a novel therapeutic target of antibiotics. *Journal of Biological Chemistry*, 278(45):44424–44428, 2003.

Lilin Wang and Joe Lutkenhaus. Ftsk is an essential cell division protein that is localized to the septum and induced as part of the sos response. *Molecular microbiology*, 29(3):731–740, 1998.

David M Warshaw, Janet M Desrosiers, Steven S Work, and Kathleen M Trybus. Smooth muscle myosin cross-bridge interactions modulate actin

filament sliding velocity in vitro. *The Journal of cell biology*, 111(2):453–463, 1990.

David S Weiss, Joseph C Chen, Jean-Marc Ghigo, Dana Boyd, and Jon Beckwith. Localization of ftsi (pbp3) to the septal ring requires its membrane anchor, the z ring, ftsa, ftsq, and ftsl. *Journal of bacteriology*, 181(2):508–520, 1999.

Gerard D Wright. The antibiotic resistome: the nexus of chemical and genetic diversity. *Nature Reviews Microbiology*, 5(3):175–186, 2007.

Ling Juan Wu and Jeff Errington. Coordination of cell division and chromosome segregation by a nucleoid occlusion protein in bacillus subtilis. *Cell*, 117(7):915–925, 2004.

Ling Juan Wu and Jeff Errington. Nucleoid occlusion and bacterial cell division. *Nature Reviews Microbiology*, 10(1):8–12, 2012.

Ling Juan Wu, Shu Ishikawa, Yoshikazu Kawai, Taku Oshima, Naotake Ogasawara, and Jeff Errington. Noc protein binds to specific dna sequences to coordinate cell division with chromosome segregation. *The EMBO Journal*, 28(13):1940–1952, 2009.

Xuan-Chuan Yu and William Margolin. Ca2+-mediated gtp-dependent dynamic assembly of bacterial cell division protein ftsz into asters and polymer networks in vitro. *The EMBO journal*, 16(17):5455–5463, 1997.

Ying Zhao and Sharad Malik. Exact memory size estimation for array computations. *IEEE Transactions on Very Large Scale Integration (VLSI) Systems*, 8(5):517–521, 2000.